

Dispersive hydrodynamics in viscous fluid conduits

by

Michelle Dorothy Maiden

B.S., Meredith College, 2014

B.A., Meredith College, 2014

M.S., University of Colorado Boulder, 2017

A thesis submitted to the
Faculty of the Graduate School of the
University of Colorado in partial fulfillment
of the requirements for the degree of
Doctor of Philosophy
Department of Applied Mathematics

2019

This thesis entitled:
Dispersive hydrodynamics in viscous fluid conduits
written by Michelle Dorothy Maiden
has been approved for the Department of Applied Mathematics

Dr. Mark Hoefer

Dr. Gennady El

Dr. Keith Julien

Dr. John Crimaldi

Dr. Daniel Appelö

Date _____

The final copy of this thesis has been examined by the signatories, and we find that both the content and the form meet acceptable presentation standards of scholarly work in the above mentioned discipline.

Maiden, Michelle Dorothy (Ph.D., Applied Mathematics)

Dispersive hydrodynamics in viscous fluid conduits

Thesis directed by Dr. Mark Hoefer

Viscous fluid conduits provide an ideal system for the study of dissipationless, dispersive hydrodynamics. A dense, viscous fluid serves as the background medium through which a lighter, less viscous fluid buoyantly rises. If the interior fluid is continuously injected, a deformable pipe forms. The long wave interfacial dynamics are well-described by a dispersive nonlinear partial differential equation called the conduit equation.

Experiments, numerics, and asymptotics of the viscous fluid conduit system will be presented. Structures at multiple length scales are characterized, including solitary waves, periodic waves, and dispersive shock waves. A more generic class of large-scale disturbances is also studied and found to emit solitary waves whose number and amplitudes can be obtained. Of particular interest is the interaction of structures of different scales, such as solitary waves and dispersive shock waves. In the development of these theories for the conduit equation, we have uncovered asymptotic methods that are applicable to a wide range of dispersive hydrodynamic systems.

The conduit equation is nonintegrable, so exact methods such as the inverse scattering transform cannot be implemented. Instead, approximations of the conduit equation are studied, including the Whitham modulation equations, which can be derived for any dispersive hydrodynamic system with a periodic wave solution family and at least two conservation laws. The combination of the conduit equation's tractability and the relative ease of the associated experiments make this a model system for studying a wide range of dispersive hydrodynamic phenomena.

Dedication

To my family and friends.

Acknowledgements

Mark Hoefer. Thank you for your guidance and support from working with you as an undergraduate until now. Your ability to take everything in stride is humbling and inspiring.

Gennady El. I fondly look back on the summer I worked with you. Thank you for helping me understand your methodology and its implications.

My dissertation committee: John Crimaldi, Daniel Appelö, and Keith Julien. I appreciate your participation in this process and your input.

Members of the Dispersive Hydrodynamics Laboratory. It has been my privilege to work with all of you.

Department of Applied Mathematics, University of Colorado Boulder. I appreciate the department's unfailing support and the many people I have met there.

My parents and siblings. You have listened to and supported me through this undertaking and all of my life. Your love has strengthened me when I needed it most. Thank you.

Sama Shrestha, Lara Pantlin, and Andrew Parliment. The support of my friends through these years of graduate school was integral to completing my degree. I cannot imagine being where I am without knowing you.

I gratefully acknowledge financial support by the National Science Foundation through the Graduate Research Fellowship Program and by the University of Colorado Boulder through the Chancellor's Fellowship.

Contents

Chapter	
1	1
1.1	1
1.1.1	2
1.1.2	4
1.1.3	6
1.1.4	7
1.1.5	9
1.1.6	12
1.2	15
1.2.1	15
1.2.2	20
1.2.3	21
1.2.4	22
1.2.5	22
1.2.6	24
1.2.7	27
1.3	28
1.3.1	28
1.4	28

1.4.1	Setup	29
1.4.2	Methods	30
2	Modulations of Periodic Waves	33
2.1	Periodic Traveling Wave Solutions	34
2.1.1	Stokes Expansion	35
2.2	Weakly Nonlinear, Dispersive Modulations	36
2.3	Whitham Equations	43
2.3.1	Weakly Nonlinear Regime	47
2.3.2	Large Amplitude Regime	48
2.4	Discussion and Conclusion	52
3	Generation and Observation of Dispersive Shock Waves	56
3.1	Generation of Wavebreaking Profiles	56
3.1.1	Theory	58
3.1.2	Experimental Methods	64
3.1.3	Results for Wavebreaking Profiles	66
3.1.4	Conclusions about Wavebreaking Profiles	68
3.2	Post-Wavebreaking Interpretation	68
3.2.1	Methods	71
3.2.2	Poiseuille Flow	71
3.2.3	Mass Diffusion	72
3.2.4	Results and Discussion	72
4	Solitary Wave Fission of a Large Disturbance in a Viscous Fluid Conduit	79
4.1	Observation of Solitary Wave Fission	81
4.1.1	Experimental Setup	82
4.1.2	Methods	82

4.1.3	Results	84
4.2	Conduit Equation Solitary Wave Fission	85
4.2.1	Number of Solitary Waves	87
4.2.2	Distribution of Solitary Wave Amplitudes	90
4.2.3	General Method	97
4.2.4	Numerical Methods	98
4.2.5	Comparison to Experiment	98
4.3	Conclusion	101
5	Solitonic Dispersive Hydrodynamics: Theory and Observation	103
5.1	Observation of Soliton Interactions with Dispersive Hydrodynamic Structures	103
5.1.1	Experiment Setup and Methods	106
5.1.2	Results	107
5.2	Solitonic Dispersive Hydrodynamics	107
5.2.1	Riemann Invariants	111
5.2.2	Initial Value Problem for Diagonalized System	113
5.2.3	Rarefaction Wave Results	114
5.2.4	Dispersive Shock Wave Results	116
5.3	Comparison to Experiment	118
5.4	Soliton Phase Shift through a General Disturbance	118
5.5	Conclusion	123
6	Conclusion	125

Bibliography	127
---------------------	------------

Appendix

A Numerical Methods	133
A.1 Periodic Solutions	133
A.2 Time Stepping	134

Tables

Table

3.1	Boundary conditions $a(0, t)$ resulting in approximate profiles of interest. All profiles have a breaking time t_b based on the breaking height z_b of $t_b = z_b/2$	63
4.1	Densities, viscosities, viscosity ratio, and background flow rate from the experiments reported in chapter 4.	82
5.1	Densities, viscosities, viscosity ratio, and background flow rate from the experiments reported in chapter 5.	106

Figures

Figure

- | | | |
|-----|--|----|
| 1.1 | (a) KdV soliton on background $\bar{v} = 1/2$, with amplitude above background $\mathcal{A} = 3/2$ and subsequent speed $c = 1$. (b) Evolution over time of the soliton from (a) in the (x, t) -plane. The color represents amplitude of the solution. | 3 |
| 1.2 | Possible phase planes for equation (1.8). Note in (a) the solution is unbounded. In (b), the solution is bounded between the three roots, but the derivative is only real between the latter two ($x = 1/2$ and $x = 3/2$). | 5 |
| 1.3 | Three cnoidal waves in the form of equation (1.9) with (solid black) $(f_1, f_2, f_3) = (1.5, 2.9, 3)$, (dashed dark blue) $(f_1, f_2, f_3) = (1, 2, 3)$, and (dotted light blue) $(f_1, f_2, f_3) = (1, 1.01, 3)$. Note the limiting cases are cosine-like and soliton-like. | 6 |
| 1.4 | Example KdV soliton train interacting with a rarefying mean flow. | 9 |
| 1.5 | DSW generated from full numerics of the KdV equation (1.2), with an initial step at 0 with $v_- = 1$ and $v_+ = 0$, at time $t = 200$. Note the leading edge is approaching the predicted amplitude of 2. | 10 |
| 1.6 | Normalized soliton amplitude cumulative distribution functions (cdfs) in the spectral parameter η for IST box prediction equation (1.25) [2] (solid black) and soliton fission (1.27) (dashed blue) for box-like initial conditions with $u_m = 1$ and (a) $w = 50$, (b) $w = 400$ | 14 |

1.7	(solid, blue) Solitary wave solution to the conduit equation (1.3) with $\mathcal{A}_s = 3$ on a background $\bar{\phi} = 1$. This wave has speed $c_s \approx 2.94$. For comparison, the KdV soliton solution from equation (1.5) with the same parameters is also shown, and has a nondimensional speed of $5/3$	23
1.8	Still from an experiment where two interior fluids were used. The two fluids were identical except for the difference in the dye used. Note there are two solitons in the image and the closed streamlines inside [40].	25
1.9	(a) Schematic of a possible experimental setup. (b) Schematic of a perturbed conduit [5].	31
1.10	Processed images from a glycerine trial [5]. Measured parameter values are $\mu^{(i)} = 72 \pm 1\text{cP}$, $\rho^{(i)} = 1.222 \pm 0.001\text{g/cm}^3$, $\mu^{(e)} = 1190 \pm 20\text{cP}$, $\rho^{(e)} = 1.262 \pm 0.001\text{g/cm}^3$, and $Q_0 = 0.25 \pm 0.01\text{ml/min}$. The grayscale images are overlayed with the extracted conduit edges.	32
2.1	A computed periodic wave solution to the conduit equation with wavenumber $k = 2$, amplitude $\mathcal{A} = 1.5$, and unit mean $\bar{\phi}$	33
2.2	Comparison of the Stokes wave expansion solution (dashed lines) to the numerically computed solution (solid lines) for three different waves with unit mean. $(\tilde{k}, \tilde{\mathcal{A}})$ are $(1/4, 1)$ (black), $(2, 2)$ (blue), and $(1, 0.5)$ (red). The approximate and numerical solutions for $(\tilde{k}, \tilde{\mathcal{A}}) = (1, 0.5)$ are indistinguishable.	36
2.3	(a) Contour plot of numerically computed dispersion relation. (b) Numerically computed phase velocity. c) Relative error between numerically computed dispersion $\tilde{\omega}(\tilde{k}, \tilde{\mathcal{A}})$ and approximate dispersion $\tilde{\omega}_0(\tilde{k}) + \tilde{\mathcal{A}}^2 \tilde{\omega}_2(\tilde{k})$. Markers (\times) correspond to waves plotted in figure 2.2.	37
2.4	Evolution of weakly nonlinear envelope soliton initial conditions for the conduit equation (1.3). (a) Approximate black soliton initial condition (2.18) with $\tilde{\mathcal{A}} = 0.2$, $\tilde{k} = 1$. (b) Approximate bright soliton initial condition (2.19) with $\tilde{\mathcal{A}} = 0.2$, $\tilde{k} = 3$	40

- 2.5 Evolution of large amplitude dark envelope soliton initial conditions for the conduit equation (1.3). (a) Approximate black soliton initial condition (2.18) with $\tilde{\mathcal{A}} = 1.6$, $\tilde{k} = 1$ breaking up into multiple coherent “dark” wave structures. (b) The large amplitude dark structure from (a) is isolated and evolved, maintaining its coherence. 42
- 2.6 Evolution of large amplitude bright envelope soliton initial conditions for the conduit equation (1.3). (a) Approximate bright soliton initial condition (2.18) with $\tilde{\mathcal{A}} = 0.6$, $\tilde{k} = 3$ breaking up into two coherent “bright” wave structures and small amplitude dispersive radiation. (b) The largest amplitude bright structure from (a) is isolated and evolved, maintaining its coherence. 42
- 2.7 (a) Elliptic (gray) and hyperbolic (white) parameter regimes for the Whitham equations corresponding to complex or real characteristic velocities, respectively. Identified stable (dots) and unstable (squares) periodic waves according to direct numerical simulation of the conduit equation. (b) Contour plot of the imaginary part of the characteristic velocity \tilde{c}_2 , the MI growth rate. The maximum, 0.04795, occurs for $(\tilde{k}, \tilde{\mathcal{A}}) = (2.711, 1.204)$ 49
- 2.8 Numerical evolution of perturbed periodic wave solutions in the conduit equation. (a) Modulationally stable case: $(\tilde{k}, \tilde{\mathcal{A}}) = (2, 2)$. (b) Modulationally unstable case: $(\tilde{k}, \tilde{\mathcal{A}}) = (3, 0.5)$. Top: the respective cases at the final time $t = 750$ 50
- 2.9 (a) Loss of genuine nonlinearity in the Whitham equations. The curves correspond to regions in the \tilde{k} - $\tilde{\mathcal{A}}$ plane where the computed quantities $\mu_{2,3}$ (solid) or μ_1 (dashed) change sign. To the right of the solid (dashed) curve, $\mu_3 > 0$, $\mu_2 < 0$ ($\mu_1 > 0$). The dash-dotted curve corresponds to the prediction $\mu_1 = 0$ from the weakly nonlinear analysis equation (2.37). The elliptic region from figure 2.7 is also depicted (gray). (b) Zoom-in of the small \tilde{k} region of (a) where $\mu_{2,3} \approx 0$ (red) approximately corresponds to the largest \tilde{k} , to the left of which $|\tilde{c}_3 - \tilde{c}_2| < 10^{-5}$ (black), i.e., approaching non-strict hyperbolicity. 53

- 3.1 Interfacial wave breaking of two Stokes fluids causing the spontaneous emergence of coherent oscillations, a DSW. The leading, downstream edge is approximately a large amplitude solitary wave whose phase speed is tied to the upstream conduit area. The trailing, upstream edge is a small amplitude wave packet moving at the group velocity whose wavenumber is tied to the downstream conduit area. (a) 90° clockwise rotated, time-lapse digital images (aspect ratio 10:1). (b) Space-time contour plot of the conduit cross-sectional area from (a). Nominal experimental parameters: $\Delta\rho = 0.0928 \text{ g/cm}^3$, $\mu^{(i)} = 91.7 \text{ cP}$, $\epsilon = 0.030$, downstream flow rate $Q_0 = 0.50 \text{ mL/min}$, and $a_- = 2.5$ 57
- 3.2 Characteristic plots (large plots) and wavebreaking profiles at time of breaking (small plots). The gray regions are areas where wavebreaking has occurred and small-scale dispersion is important so the inviscid Burger's solution is no longer valid. Shown here are step (a), box (b), triangle (c), and N-wave (d) wavebreaking profiles. 60
- 3.3 (a) Temporal profile of the boundary condition equation (3.13). (b) Evolution of the rescaled rarefaction wave equation (3.13). As time moves forward, the wave approaches the desired step. The dots in (a) correspond to the times depicted in (b), from left to right. 62
- 3.4 (a) Processed images from a glycerine trial. Measured parameter values are $\mu^{(i)} = 72 \pm 1 \text{ cP}$, $\rho^{(i)} = 1.222 \pm 0.001 \text{ g/cm}^3$, $\mu^{(e)} = 1190 \pm 20 \text{ cP}$, $\rho^{(e)} = 1.262 \pm 0.001 \text{ g/cm}^3$, and $Q_0 = 0.25 \pm 0.01 \text{ ml/min}$. The grayscale images are overlaid with the extracted conduit edges. (b) Nondimensional area plot corresponding to the images in (a). The vertical line indicates the measured breaking height obtained by the inflection criterion. The dashed line indicates the expected step in a dispersionless system. Predictions were fit to the found Poiseuille flow relation (1.61). 65
- 3.5 Numerical simulation of the conduit equation with initial condition $a(z, 0) = 1$ and the boundary condition equation (3.13) with $z_b = 100$ and $a_b = 2$. The predicted z_b and $t_b = 50$ are marked. 65

- 3.6 Numerics: slope of the front of the evolving structure over time. Inset: three profiles in space corresponding to the marked points in time. Observe dispersion is in full effect by the time the slope of the leading edge has ‘leveled out.’ The expected breaking time of the input boundary condition was $t_b = 50$ 66
- 3.7 Comparison of dispersionless (long-wave) theory (dashed lines), full conduit equation numerics (triangles) and glycerine experiments (squares) for the step wavebreaking configuration. (a) Breaking height results and (b) relative error for experiments as a function of jump ratio a_b , with the same fluid parameters as those in figure 3.4. (c) Breaking time results and (d) relative error for those same experiments. Note the breaking time error bars are smaller than the symbols used. The black squares correspond to an expected $z_b = 15.3$ cm, the gray to $z_b = 20.5$ cm, and the white to $z_b = 25.6$ cm. 67
- 3.8 Experimental data for (a) triangle wave and (b) N-wave boundary conditions. Overlay lines: fitted characteristic data for the respective experiments. 69
- 3.9 Demonstration of Poiseuille flow in a steady viscous fluid conduit. Log-log plot of measured conduit diameter D near injection site versus volumetric flow rate Q (dots) and the relation $D = \alpha Q^{1/4}$ with the measured value $\alpha = 0.2557$ (cm·min)^{1/4} (solid) corresponding to $\mu^{(i)} = 80.4$ cP, $\Delta\rho = 0.1305$ g/cm³. A least squares fit gives $\alpha = 0.2548$ (cm·min)^{1/4}, which translates to the fitted viscosity $\mu^{(i)} = 79.0$ cP, within the 2% error tolerance of our rotational viscometer. 73
- 3.10 Poiseuille flow fit approximately 120 cm up the fluid column. Downstream conduit diameters D extracted from digital images (dots) and a least squares fit to the Poiseuille flow relation $D = \alpha Q^{1/4}$ with $\alpha = 0.2688$ (cm·min)^{1/4} (solid). The fit corresponds to the interior viscosity $\mu^{(i)} = 104$ cP, an increase from its measured value $\mu^{(i)} = 80.4$ cP. This can be explained by the shear thinning properties of corn syrup. 73

3.11	Comparison of conduit diameter at different locations along the fluid column. Measurements (dots) and the linear fit $D_{\text{top}} = mD_{\text{bottom}}$ (solid) with $m = 1.07$ corresponding to a 7% increase in the conduit diameter. The lower (upper) diameter was measured approximately 6 cm (120 cm) above the injection site.	74
3.12	Comparison of observed and predicted leading edge DSW amplitude and speed. Observations (circles), Whitham modulation theory (solid), and numerical simulation of the conduit equation (dashed) for (a) DSW leading edge speeds s_+ and (b) DSW leading amplitude \mathcal{A}_+ versus downstream area ratio a_- . Nominal experimental parameters: $\Delta\rho = 0.1305 \text{ g/cm}^3$, $\mu^{(i)} = 80.4 \text{ cP}$ (measured), $\mu^{(i)} = 104 \text{ cP}$ (fitted as described in section 3.2.2), $\epsilon = 0.0024$	76
3.13	Time-lapse images (aspect ratio 1:1) of large amplitude wave breaking leading to upstream propagation of the DSW trailing edge envelope: DSW backflow. Nominal experimental parameters: $\Delta\rho = 0.0983 \text{ g/cm}^3$, $\mu^{(i)} = 93.5 \text{ cP}$, $\epsilon = 0.029$, $a_- = 4$, and $Q_0 = 0.50 \text{ mL/min}$	77
4.1	A box initial condition (inset) and its long-time numerical evolution according to the conduit equation (1.3). The number denotes the predicted number of solitary waves from that initial condition, and the black circles with vertical bars denote the ranges from a quantiled distribution of the predicted solitary wave amplitudes, both derived later in this chapter.	81
4.2	Experimental development and dispersion of a box over the full experiment.	83
4.3	(a) Example of an experimental box. Note wavebreaking (DSW formation) has already initiated at the leading edge. (b) Conduit area over time at a fixed distance in the upper part of the apparatus.	84
4.4	Observed number of solitary waves \mathcal{N} from experimental boxes of differing dimensional widths and nondimensional heights a_m . Least-square linear fits for each dataset are included.	85

4.5	Experimental cdfs for solitary wave amplitudes $\mathcal{F}_{a_m}(\mathcal{A}; w)$, for different boxes. Each plot corresponds to a different input a_m and darker lines correspond to narrower boxes.	86
4.6	Wavenumber k_- versus the wave mean $\bar{\phi}$, with fixed integration constant $\lambda = 1/2$. The solid line shows k_- from the conduit equation, and the dashed line is the result from the KdV equation (1.26), rescaled for the conduit equation via (4.3). This monotonic relationship determines the mean-to-wavenumber mapping of the initial box disturbance.	89
4.7	Plot of the solitary wave level curve corresponding to $k_- = 0$ in $(\lambda, \bar{\phi})$ -space.	91
4.8	(a) Truncation of the initial profile from figure 4.1 for different values of λ . (b) Expected contribution of each λ -truncation in terms of the produced solitary waves.	92
4.9	Integral endpoints $z_{1,2}$ as a function of the integration constant, λ , for the initial condition of figure 4.1.	93
4.10	(a) Numerical simulations of boxes of different widths $w = 100, 200, 300, 400$ with fixed $a_m = 2$ and the ensuing solitary waves. Note the evolutions here are at different times and shifted to align, to better illustrate the similarities and differences in the amplitude distributions. (b) (solid) Amplitude distributions from the same simulations, (dashed) Predicted amplitude distribution from equation (4.34) for the smoothed box, and (dash-dotted) predicted amplitude distribution from equation (4.38) for a pure box.	99
4.11	(a) Numerical simulations of boxes of different heights $a_m \in 1, 2, 3, 4$ with fixed $w = 150$ and the ensuing solitary waves. The evolutions here are at different times, to better illustrate the similarities and differences in the amplitude distributions. The expected solitary wave counts do not change much past a certain initial condition amplitude, as expected from equation (4.14). (b) (solid) Amplitude distributions from the same simulations, and (dashed) Predicted amplitude distribution from equation (4.34) for the smoothed box.	99

- 4.12 (a) Number of solitary waves from experiment (circles) versus the number expected from equation (4.4). The dashed and dot-dashed lines represent one and two solitary waves away from the expected 1:1 relationship. (b) Relative error versus the expected number of solitary waves. Note the relative error goes down dramatically as \mathcal{N} increases. 100
- 4.13 Cdfs of amplitude distributions from selected experiments (solid line), with the asymptotic expectation from using the conduit equation (4.34) for the smoothed box (dashed line) and KdV (dotted line). Each step in the experimental cdf corresponds to a solitary wave. Box parameters: (a) width=20 cm, $a_m = 2$ (b) width=40 cm, $a_m = 4$ 100
- 4.14 Experimental amplitude cdfs (stairs) versus (dashed) Predicted amplitude distribution from equation (4.34) for the smoothed box, and (dash-dotted) predicted amplitude distribution from equation (4.38) for a pure box. Color scale corresponds to initial conditions where $a_m = 2$ and (light to dark) widths 25, 30, 35, 40 cm. 101
- 5.1 Interactions of solitons and DSWs. Time-lapse images with aspect ratio 10:1 (a) and space-time contour (b) of DSW-solitary wave interaction revealing solitary wave refraction by a DSW with $a_- = 3$. (c) Space-time contour of the absorption of a solitary wave by a DSW with $a_- = 3.5$. (d) DSW-DSW interaction and merger causing multiphase mixing (inset) and the refraction of the trailing DSW by the leading DSW with $a_1 = 2.5$, $a_2 = 5$. Nominal experimental parameters: $\Delta\rho = 0.0971$ g/cm³, $\mu^{(i)} = 99.1$ cP, $\epsilon = 0.029$, $Q_0 = 0.2$ mL/min. 105

- 5.2 Experiments demonstrating soliton transmission and trapping with hydrodynamic states. Representative image sequences (a,c,e,g) and space-time contours (b,d,f,h) extracted from image processing are shown. The contour intensity scale is the dimensionless conduit cross-sectional area relative to the smallest area. a,b) Soliton-RW transmission. c,d) Soliton-RW trapping. e,f) Soliton-DSW transmission. g,h) Soliton-DSW trapping. 108
- 5.3 Representative initial configuration and evolution (top to bottom) for solitonic dispersive hydrodynamics. The narrow soliton on the uniform mean field \bar{u}_- is transmitted through the broad hydrodynamic flow if it reaches and propagates freely on the uniform mean field \bar{u}_+ . The hydrodynamic flow exhibits expansion (rarefaction) and compression that leads to a dispersive shock wave. 109
- 5.4 Graphical depictions of hydrodynamic reciprocity. (a) Space-time contour plot of soliton-DSW ($t > 0$) and soliton-RW ($t < 0$) interaction with two solitons satisfying the transmission condition (5.13). For $|t|$ sufficiently large, the soliton speeds are the same. (b) If the soliton post DSW interaction (top, left to right) is used to initialize soliton-RW interaction (bottom, right to left), the post RW interaction soliton has the same properties as the pre DSW interaction soliton. 117
- 5.5 Transmitted soliton properties due to conduit soliton-RW and DSW interaction for a hydrodynamic transition from $\bar{u} = 1$ to $\bar{u} = 1.75$. a) Soliton amplitude from eq. (5.13) (curve), experiment (filled squares, triangles), and numerical simulations (open squares, triangles). b) Soliton phase shift from eq. (5.13) (curves) and numerical simulations (symbols). 119
- 5.6 Comparison of predicted soliton phase shifts from the soliton fission prediction equation (1.27) (x's), IST box approximation (neglecting radiation) equation (1.25) (squares), equation (5.17) (o's), and (5.22) (triangles) with numerics. 122

5.7	Percent relative error associated with predicted soliton phase shifts from the soliton fission prediction equation (1.27) (x's), IST box approximation (neglecting radiation) equation (1.25) (squares), equation (5.17) (o's), and (5.22) (triangles) compared to numerics as a function of (a) box width w , with soliton amplitude $a_s = 5$ and (b) test soliton amplitude a_s , with width $w = 200$	122
5.8	Example of a generic localized profile evolving according to KdV and its interaction with a soliton. (a) At different times (b) Space-time contour plot. Note the subtle phase shift identified by the difference between the t -intercepts of the dashed curve and solid line.	124
A.1	Maximum absolute error in the direct numerical simulation of the conduit equation, achieving fourth order spatial accuracy as expected. The solution used in validation was a periodic wave with $k = 3$ and $a = 0.5$ generated with accuracy 10^{-8} , and was simulated over 50 spatial periods and 5 temporal periods. The reference line is $C(\Delta z)^{-4}$	134

Chapter 1

Introduction

This dissertation is an amalgamation of several papers from the author [56, 55, 54, 5]. These will be heavily drawn on in this and other chapters.

1.1 Dispersive Hydrodynamics

Long wavelength, hydrodynamic theories abound in physics, from fluids [48] to optics [9], condensed matter [28] to quantum mechanics [88], and beyond. Such theories describe expansion and compression waves until wavebreaking occurs, which is when characteristics cross, and the solution may become multivalued. In classical fluids where dissipation is the driving force, this results in a shock wave, a disturbance that moves faster than the local speed of sound [21]. When the physics at shorter wavelengths are predominantly dispersive, wavebreaking is regulated by the dispersion, and dispersive hydrodynamic theories [87, 21] are used to describe shock waves of a spectacularly different character than their dissipative counterparts.

Solitary waves and dispersive shock waves (DSWs) are key coherent structures in dispersive hydrodynamic systems. Model equations include the integrable Korteweg-de Vries (KdV) and Nonlinear Schrödinger (NLS) equations as well as non-integrable counterparts that are important for applications to superfluids, geophysical fluids, and laser light. A generic initial value problem (IVP) for a scalar dispersive hydrodynamic equation is of the form [54]

$$u_t + V(u)u_x = D[u]_x, \quad x \in \mathbb{R}, \quad t > 0, \quad u(x, 0) = u_0(x). \quad (1.1)$$

$V(u)$ is the long-wave speed, $D[u]$ is an integro-differential operator, and equation (1.1) admits a real-valued, linear dispersion relation with frequency $\omega(k, \bar{u})$ where k is the wavenumber and \bar{u} is the background mean field. We assume $V'(u) > 0$ so that the dispersive hydrodynamic system has convex flux [22].

Throughout this section, we will illustrate dispersive hydrodynamic concepts using the well-studied KdV equation

$$v_t + vv_x + v_{xxx} = 0. \quad (1.2)$$

We chose the KdV equation because it is the simplest equation with both nonlinear and dispersive terms, so it is a commonly used example in the field [21]. Although the KdV equation is integrable, integrability will not be used in this introduction, except for comparison with the results found. Instead, the focus will be on results from Whitham modulation theory, which can also be applied to nonintegrable systems. In this chapter, we will use $u(x, t)$ to represent a generic hydrodynamic system (1.1) and $v(x, t)$ when showing results for the KdV equation (1.2) in particular.

While we present some results for KdV in chapter 5 for KdV, the majority of this thesis is focused on results for the conduit equation,

$$a_t + (a^2)_z - (a^2 (a^{-1} a_t)_z)_z = 0, \quad (1.3)$$

which is the focus of section 1.2.

1.1.1 Solitary Waves

Solitary waves or solitons are localized travelling waves that may travel with an amplitude-dependent speed. These waves are hallmarks of dispersive hydrodynamic systems, and their study dates back to the beginning of the field, when a solitary wave was observed in a shallow water canal and followed on horseback [67]. This observation led to a series of experiments and eventually the derivation of the (1+1)-dimensional KdV equation (1.2), first as a footnote by Boussinesq [8] and later more elaborately by Korteweg and de Vries [47].

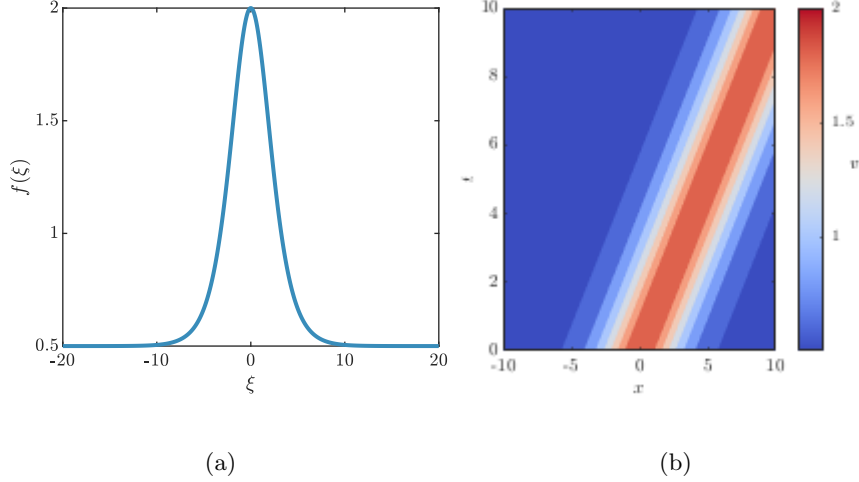


Figure 1.1: (a) KdV soliton on background $\bar{v} = 1/2$, with amplitude above background $\mathcal{A} = 3/2$ and subsequent speed $c = 1$. (b) Evolution over time of the soliton from (a) in the (x, t) -plane. The color represents amplitude of the solution.

The terminology “soliton” versus “solitary wave” relates to the integrability of the governing equation (1.1) [1]. In addition to the above conditions, a true soliton interacts with other solitons elastically, with the only result of the interaction a spatial/temporal phase shift. Many waves exhibit the localization and speed-amplitude property, but there exists other residue from interactions, such as a small dispersive tail [51]. The term solitary wave is used to describe these ‘near-solitons’ that do not interact elastically.

Solitary wave solutions for a generic equation (1.1) can be found by assuming the ansatz

$$u(x, t) = f(\xi), \quad \xi = x - ct, \quad \lim_{|\xi| \rightarrow \infty} f(\xi) = \bar{u}, \quad \lim_{|\xi| \rightarrow \infty} f^{(n)}(\xi) = 0, \quad n = 1, 2, 3, \dots \quad (1.4)$$

where $\bar{u}, c \in \mathbb{R}$. Inserting this ansatz into (1.2) and integrating results in an explicit expression for f , with background \bar{v}

$$f(\xi) = \bar{v} + 3(c - \bar{v}) \operatorname{sech}^2 \left(\frac{\sqrt{c - \bar{v}}}{2} \xi \right). \quad (1.5)$$

The speed-amplitude relation is readily realized as $c(\mathcal{A}, \bar{v}) = \mathcal{A}/3 + \bar{v}$. An example profile and its behavior over time is given in figure 1.1.

The phase shift for interactions of KdV solitons is known explicitly via the inverse scattering

transform to be [1]

$$\phi(\eta_1, \eta_2) = \frac{1}{\eta_1} \log \left| \frac{\eta_1 + \eta_2}{\eta_1 - \eta_2} \right|, \quad \eta_1 > \eta_2, \quad (1.6)$$

where η_j is termed the spectral parameter and relates to the amplitude \mathcal{A}_j of the j^{th} soliton, $j = 1, 2$, via $\mathcal{A}(\eta) = 12\eta^2$.

Solitary waves play a central role in this thesis, and will be represented in some capacity in every chapter. New results pertaining to solitary waves mainly concern their interactions with hydrodynamic structures, which will be covered in detail in chapter 5.

1.1.2 Periodic Waves

Periodic traveling waves are another class of important traveling wave solutions to dispersive hydrodynamic equations. The ansatz

$$u(x, t) = f(\theta), \quad \theta = kx - \omega t, \quad f(\theta + 2\pi) = f(\theta) \quad (1.7)$$

inserted into the KdV equation (1.2) leads to the first-order ordinary differential equation

$$(f')^2 = -\frac{1}{3k^2}(f - f_1)(f - f_2)(f - f_3) \quad (1.8)$$

with roots of the right-hand side f_1, f_2, f_3 . When there are two complex conjugate roots, the solution is unbounded, as can be seen in figure 1.2(a). A real periodic wave can therefore exist only when all three roots are real and that solution oscillates between the two larger roots, as can be seen when plotting the phase plane, as in figure 1.2(b). When two roots are equal, either the amplitude of the wave is zero or the wave has an infinite period; these limiting cases are discussed in more detail below. Since we have three real roots, we can order them such that $f_1 \leq f_2 \leq f_3$, so the wave solution exists for f between f_2 and f_3 . When the solution exists, the solution to (1.8) can be written in terms of a Jacobi elliptic function [21]

$$f(\theta) = f_1 + (f_3 - f_1) \operatorname{dn}^2 \left[\frac{K(m)}{\pi} \theta; m \right], \quad m = \frac{f_3 - f_2}{f_3 - f_1}, \quad 0 \leq m \leq 1, \quad (1.9)$$

where $K(m)$ is the complete elliptic integral of the first kind. There are two limiting cases of equation (1.9). First, when $f_2 \rightarrow f_3$, we have $m \rightarrow 0$, and the amplitude of the cnoidal wave

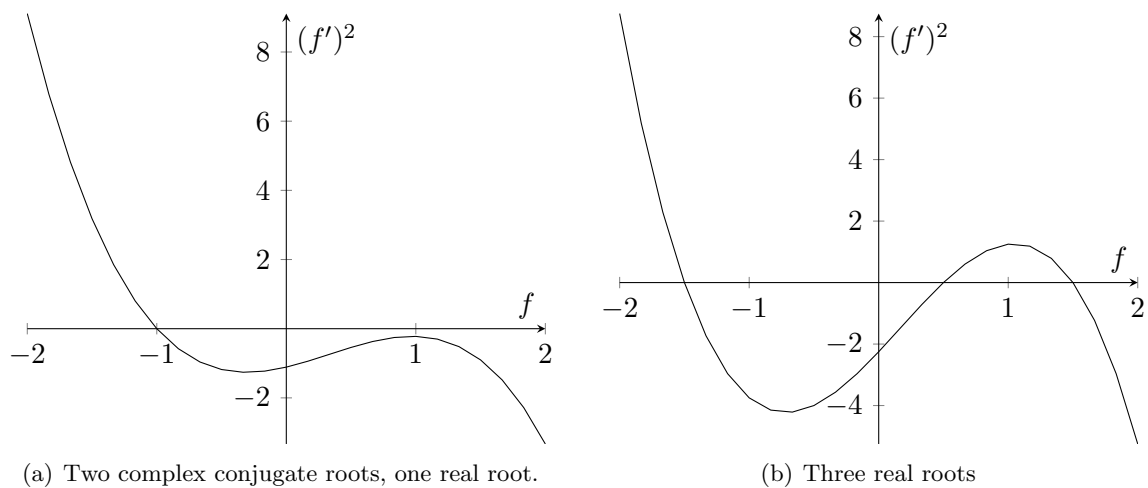


Figure 1.2: Possible phase planes for equation (1.8). Note in (a) the solution is unbounded. In (b), the solution is bounded between the three roots, but the derivative is only real between the latter two ($x = 1/2$ and $x = 3/2$).

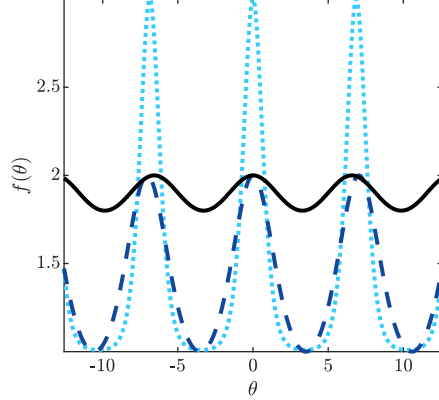


Figure 1.3: Three cnoidal waves in the form of equation (1.9) with (solid black) $(f_1, f_2, f_3) = (1.5, 2.9, 3)$, (dashed dark blue) $(f_1, f_2, f_3) = (1, 2, 3)$, and (dotted light blue) $(f_1, f_2, f_3) = (1, 1.01, 3)$. Note the limiting cases are cosine-like and soliton-like.

$f_3 - f_2$ also approaches zero. The cnoidal wave becomes a vanishingly small linear cosine wave with frequency $\omega = \sqrt{f_3 - f_1}$. Second, when $f_2 \rightarrow f_1$, note $m \rightarrow 1$, and by properties of the elliptic function, we arrive back at the soliton solution (1.5) with amplitude $\mathcal{A} = (f_3 - f_2)$. A sample cnoidal wave and its limiting cases are shown in figure 1.3.

The main purpose of introducing periodic waves in this thesis is to explore modulations of these waves, which will be introduced next.

1.1.3 Modulations of Periodic Waves

Nonlinear wave modulation is a major mathematical component of the description of dispersive hydrodynamics. Modulation theory assumes the existence of a multi-parameter family of nonlinear, periodic traveling wave solutions whose parameters change on different length and time scales relative to the wavelength and period of the periodic solution under perturbation.

There are many methods used in modulation theory, a few of which will be explored in this work. Weakly nonlinear, long waves are generically modeled by KdV, and weakly nonlinear, quasimonochromatic, short-wave oscillations are generically modeled by the NLS envelope equation. These reductions are explored for our system in [83] and in section 2.2. The bulk of this work,

however, concerns the Whitham equations. The Whitham equations describe slow modulations of, for example, the wave's mean, amplitude, and wavenumber [87]. At leading order, they are a dispersionless system of quasi-linear equations. We invoke two methods of derivation: averaging conservation laws over a periodic wave period and a formal derivation via multiple scales. The KdV-Whitham equations are found by averaging two of the KdV conservation laws over the periodic wave solution family (1.7) and then closing with the equation for conservation of waves. Using the notation $\bar{f} = \int_0^{2\pi} f \, d\theta$, the KdV-Whitham equations are (note that $\overline{f''} = 0$).

$$\begin{cases} \bar{f}_t + \left(\frac{1}{2}\overline{f^2}\right)_x = 0, \\ \left(\overline{f^2}\right)_t + \left(\frac{2}{3}\overline{f^3} - 3k^2\overline{(f')^2}\right)_x = 0, \\ k_t + \omega_x = 0. \end{cases} \quad (1.10)$$

We have parameterized the wave family with physical parameters: the mean \bar{v} , wavenumber k , and amplitude \mathcal{A} , and invoked the dispersion relation $\omega = \omega(k, \mathcal{A}, \bar{v})$. The derivation of the Whitham equations for the conduit equation 1.3 will be detailed in section 2.3.

While reductions of the Whitham equations appear in most chapters, the full conduit-Whitham equations will be studied extensively in chapter 2.

1.1.4 Modulations of Linear and Solitary Waves in a Mean Flow

There are two important reductions of the Whitham equations which apply to the linear wave and solitary wave regimes. We assume a general equation (1.1) satisfies the prerequisites for Whitham theory which are, for a system of N^{th} order, the existence of an N -parameter family of periodic solutions and the availability of $N - 1$ conservation laws [21, 54, 87]. The modulation variables used here are the physical parameterization $(\bar{u}, k, \mathcal{A})$. Then the linear and solitary wave regimes correspond to when $\mathcal{A} \rightarrow 0$ and $k \rightarrow 0$, respectively. For KdV, which will continue to be our example system, $V(u) = u$, $D[u] = -u_{xx}$, and the linear dispersion relation can be found by assuming the ansatz $u(x, t) \approx \bar{u} + \varepsilon \cos(kx - \omega_0 t)$, $\varepsilon \ll 1$

$$\omega_0(k, \bar{u}) = \bar{u}k - k^3. \quad (1.11)$$

For the linear wave regime, the $\mathcal{A} \rightarrow 0$ limit means the vanishing amplitude oscillations do not contribute to the averaging, so $\overline{F(u)} = F(\bar{u})$ for any differential operator F . Thus all θ derivatives of u are zero under the averaging operator, which reduces the first two equations into one equation for the mean flow

$$\bar{u}_t + V(\bar{u})\bar{u}_x = 0. \quad (1.12)$$

The oscillations are fully characterized by the conservation of waves equation for linear waves

$$k_t + \omega_{0,k}k_x + \omega_{0,\bar{u}}\bar{u}_x = 0, \quad (1.13)$$

where $\omega_0(k, \bar{u})$ is the system's linear dispersion relation. For the KdV equation, the system for modulated linear waves in a mean flow \bar{v} is

$$\begin{aligned} \bar{v}_t + \bar{v}\bar{v}_x &= 0, \\ k_t + (\bar{v} - 3k^2)k_x + k\bar{v}_x &= 0. \end{aligned} \quad (1.14)$$

We next consider the Whitham equations in the solitary wave limit $k \rightarrow 0$. Here, the wavelength $2\pi/k$ tends to infinity, so again the contribution of oscillations to averaging vanishes and $\overline{F(u)} = F(\bar{u})$. Then the equation again reduces to the dispersionless equation (1.12) and the second equation becomes an equation for the solitary wave amplitude \mathcal{A}

$$\mathcal{A}_t + c(\mathcal{A}, \bar{u})\mathcal{A}_x + g(\mathcal{A}, \bar{u})\bar{u}_x = 0, \quad (1.15)$$

where $c(\mathcal{A}, \bar{u})$ is the solitary wave speed-amplitude relation for the system, and $g(\mathcal{A}, \bar{u})$ is a coupling function. Equations (1.12) and (1.15) combined describe modulated solitary waves ($k \equiv 0$) in a mean flow, but we can describe a ‘soliton train,’ or a periodic wave with $0 < k \ll 1$, approximately with these two equations and the approximate equation for conservation of waves in this regime,

$$k_t + [c(a, \bar{u})k]_x = 0. \quad (1.16)$$

This approximation gives additional information about the waves, including position information unavailable with just the first two equations. For the KdV equation the system for modulated

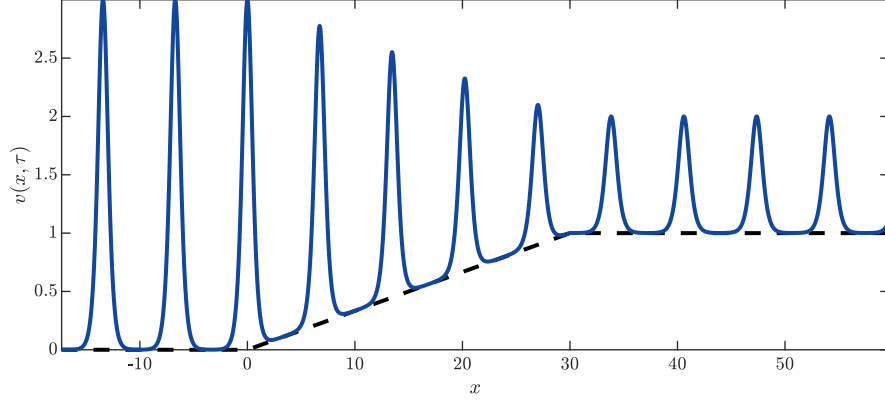


Figure 1.4: Example KdV soliton train interacting with a rarefying mean flow.

solitary waves in a mean flow \bar{v} is

$$\begin{aligned}\bar{v}_t + \bar{v}\bar{v}_x &= 0, \\ \mathcal{A}_t + (\mathcal{A}/3 + \bar{v})\mathcal{A}_x + (2\mathcal{A}/3)\bar{v}_x &= 0.\end{aligned}\tag{1.17}$$

A soliton train for the KdV equation interacting with a mean flow is shown in figure 1.4.

The interaction of small- and large-scale structures are explored in chapter 5 [54]. A general solitary wave-mean field theory is introduced, and invariants are identified that predict trapping or transmission of solitons by hydrodynamic states. The result of solitons incident upon rarefaction or dispersive shock waves is the same, an effect termed hydrodynamic reciprocity. We further extend this theory to a general mean field. Experiments on viscous fluid conduits quantitatively confirm the soliton-mean field theory. Work on linear wave-mean field theory is ongoing; early results are mentioned in the conclusion (chapter 6).

1.1.5 Dispersive Shock Waves

A DSW is an expanding, oscillatory train of amplitude-ordered nonlinear wave with two distinguishing edges. Such a DSW is usually composed of a large amplitude solitary wave adjacent to a monotonically decreasing wave envelope that terminates with a packet of small amplitude dispersive waves [21, 34]. Thus, DSWs coherently encapsulate a range of fundamental features

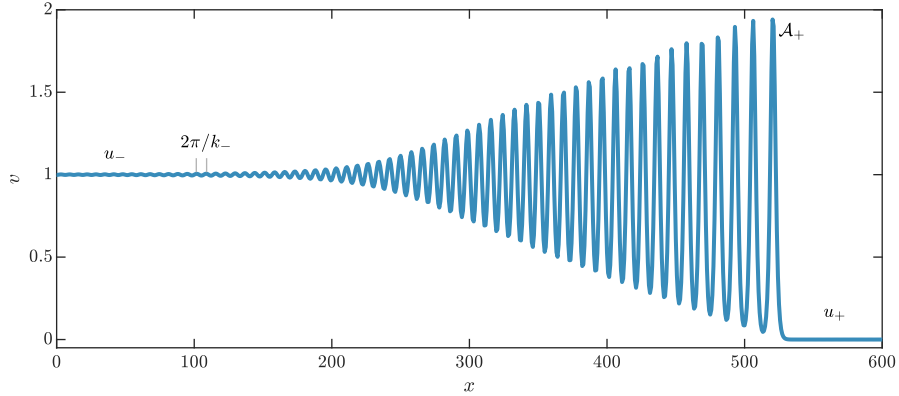


Figure 1.5: DSW generated from full numerics of the KdV equation (1.2), with an initial step at 0 with $v_- = 1$ and $v_+ = 0$, at time $t = 200$. Note the leading edge is approaching the predicted amplitude of 2.

of nonlinear wave systems. A sample DSW generated from full numerics of the KdV equation is shown in figure 1.5.

More broadly, DSWs occur in dispersive hydrodynamic media that exhibit three unifying features: i) nonlinear self-steepening, ii) wave dispersion, and iii) negligible dissipation [21]. Observations in a wide range of physical media that include quantum systems (ultra-cold atoms [17, 42], semiconductor cavities [4], electron beams [60]), optics [66, 79, 89], classical fluids [56, 77], undular bores in geophysical fluids [27, 36], collisionless shocks in rarefied plasma [75] and magnetic materials [43] demonstrate the prevalence of DSWs.

Because DSWs are well-modeled as modulated nonlinear periodic waves, Whitham theory gives invaluable insights into key features of dispersive shock waves. First consider the GP problem, named for Gurevich and Pitaevskii [34], which is the following initial value problem for the KdV-Whitham equations (1.10)

$$\bar{v}(x, t) = v_{\pm}, \quad \pm x > 0. \quad (1.18)$$

If $v_- < v_+$, wavebreaking does not occur, and an approximate solution can be found based on the dispersionless KdV equation, or the Hopf equation $v_t + vv_x = 0$. The solution is called a rarefaction

wave and takes the form

$$v(x, t) = \begin{cases} v_-, & x < v_- t \\ x/t, & v_- t < x < v_+ t \\ v_+, & x > v_+ t \end{cases} \quad (1.19)$$

If $v_- > v_+$, the Hopf solution is multivalued, and the regularizing force of dispersion must be included. Numerics of this problem suggest the solution is a slowly modulated wavetrain, given enough time to develop. The leading edge separates sufficiently from the wavetrain to be considered a solitary wave ($k \rightarrow 0$), and the trailing edge consists of oscillations of small amplitude so that they can be considered in the linear wave limit $\mathcal{A} \rightarrow 0$. Thus the long-time resolution of a DSW can be readily studied using the reduced Whitham modulation equations for the governing equation of interest, with these above assumptions guiding the study.

Recalling the linear wave system (1.12, 1.13), we look for a special solution to the hyperbolic system of equations [87] in the form of $k = k(\bar{u})$. If we restrict to only evolving along a characteristic $d/d\tau = \partial_t + \omega_{0,k}\partial_x$, k and \bar{u} can only change with respect to the differential relation

$$\omega_{0,\bar{u}} d\bar{u} + (\omega_{0,k} - V(\bar{u})) dk = 0.$$

For KdV, this has the solution

$$k_-(\bar{v}) = \sqrt{\frac{2}{3}(\bar{v} + c)}, \quad (1.20)$$

where c is a constant of integration. Similarly, if we use the solitary wave system (1.12, 1.15) and assume a solution in the form $\mathcal{A} = \mathcal{A}(\bar{u})$, along $d/d\tau = \partial_t + c(\mathcal{A}, \bar{u})\partial_x$ the differential relation satisfied is

$$g(\mathcal{A}, \bar{u}) d\bar{u} + (c(\mathcal{A}, \bar{u}) - V(\bar{u})) d\mathcal{A} = 0.$$

For KdV, this is also easily solved

$$\mathcal{A}(\bar{v}) = d - 2\bar{v}, \quad (1.21)$$

where d is another constant of integration.

For the additional degree of freedom in c, d , it was shown in [18] that this is resolved by requiring the two simple wave solutions (from the reduced equations) have to match. We use the boundary condition $k_-(v_+) = 0$ to find $c = -v_+$, and the condition $\mathcal{A}(v_-) = 0$ to find $d = 2v_-$. Then we evaluate $k_-(\bar{v})$ at the trailing edge $\bar{v} = v_-$ to find an expression for the trailing edge wavenumber

$$k_- = \frac{1}{3}\sqrt{6(v_- - v_+)}, \quad (1.22)$$

and $\mathcal{A}(v_+)$ gives an expression for the leading edge amplitude

$$\mathcal{A}_+ = 2(v_- - v_+). \quad (1.23)$$

1.1.6 Soliton Fission

Another fundamental problem in fluid dynamics is the long time resolution of a large, localized disturbance. In inviscid fluids, a prominent feature of this resolution is the emergence of a solitary wavetrain. This process is generally referred to as soliton fission and has been observed in a variety of fluid contexts [29, 6, 63, 78].

Despite the prevalence of soliton fission in fluid dynamics, its theoretical description has primarily been limited to completely integrable partial differential equations (PDEs) such as the KdV equation, a classical weakly nonlinear, long wave model [90, 44, 14]. From [2], for initial data for the KdV equation (1.2) consisting of a box of width w and height 1, assuming no radiation, the resulting number of solitons are

$$\mathcal{N}_{IST} = \frac{w}{\pi\sqrt{6}}. \quad (1.24)$$

The spectral parameters $\eta_i > 0$, $i = 1, 2, \dots, \mathcal{N}$ (Recall $\mathcal{A}(\eta) = 12\eta^2$) of the resulting solitons are the zeros of

$$\tan\left(\sqrt{1/6 - \eta^2}w\right) = \frac{2\eta\sqrt{1/6 - \eta^2}}{1/6 - 2\eta^2}. \quad (1.25)$$

A new method based on Whitham averaging theory that does not require integrability was first applied to the Serre/Su-Gardner/Green-Naghdi equations for fully nonlinear shallow water waves in [24]. The method draws upon principles first developed to describe DSWs that result

from step initial data [18]. The formulae for the expected number of solitons \mathcal{N} and the amplitude density function $f(\mathcal{A})$ for a broad initial profile $v(x, 0) = v_0(x)$ for the KdV equation (1.2) are [24]

$$\begin{aligned}\mathcal{N} &= \frac{1}{\pi\sqrt{6}} \int_{-\infty}^{\infty} \sqrt{v_0(x)} \, dx, \\ f(\mathcal{A}) &= \frac{1}{4\pi\sqrt{6}} \int_{x_1}^{x_2} \frac{dx}{\sqrt{v_0(x) - \mathcal{A}/2}}, \quad 0 \leq \mathcal{A} \leq 2v_m.\end{aligned}\tag{1.26}$$

Here, x_1 and x_2 are the intersections of $\mathcal{A}/2$ with the initial condition $v_0(x)$, which is assumed to be on a zero background with a single maximum $v_m = \max v_0(x)$. For initial data consisting of a box of width w and height u_m , eq. (1.26) becomes

$$\begin{aligned}\text{for } v_0(x) &= \begin{cases} v_m & -w < x < 0 \\ 0 & \text{else} \end{cases}, \\ \mathcal{N} &= \frac{w\sqrt{v_m}}{\pi\sqrt{6}}, \quad f(\mathcal{A}) = \frac{w}{4\pi\sqrt{6}\sqrt{v_m - \mathcal{A}/2}}, \quad 0 \leq \mathcal{A} \leq 2v_m.\end{aligned}\tag{1.27}$$

The number of solitons agrees with that obtained by the IST equations (1.24) and (1.25) in its asymptotic regime of validity $\mathcal{N} \sim w\sqrt{v_m} \gg 1$. We also observe agreement in the amplitude distributions, as shown in their normalized cumulative density functions (cdfs) in figure 1.6. The cdfs are defined in terms of $f(\mathcal{A})$ and \mathcal{N} as

$$\mathcal{F}(\mathcal{A}) = \frac{1}{\mathcal{N}} \int_{\min \mathcal{A}}^{\mathcal{A}} f(\mathcal{A}) \, d\mathcal{A}.\tag{1.28}$$

Application of this method to the nonintegrable Serre equations also showed excellent agreement with numerical simulations [24]. This method can be applied to any dispersive nonlinear wave equation that admits a Whitham modulation description [21].

We explore solitary wave fission for viscous fluid conduits in chapter 4. The method detailed in [24] is used to resolve the fission of an initial disturbance into solitary waves and predicts the relationship between the disturbance profile, the number of emergent solitary waves, and their amplitude distribution. When compared to both numerics and experiments, these predictions accurately captured the long-time resolution of the system. This is the first known experimental confirmation of this theory.

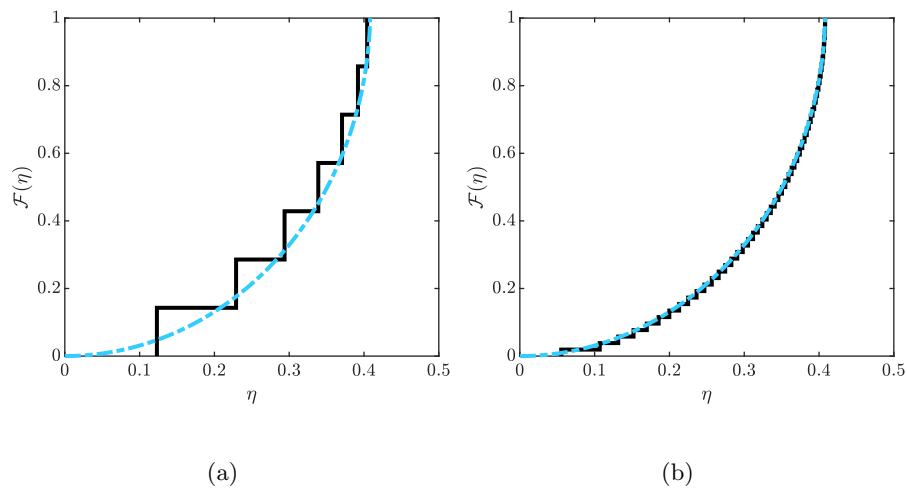


Figure 1.6: Normalized soliton amplitude cumulative distribution functions (cdf) in the spectral parameter η for IST box prediction equation (1.25) [2] (solid black) and soliton fission (1.27) (dashed blue) for box-like initial conditions with $u_m = 1$ and (a) $w = 50$, (b) $w = 400$.

1.2 The Conduit Equation

The model system for our experimental setup is the conduit equation 1.3

$$a_t + (a^2)_z - (a^2 (a^{-1} a_t)_z)_z = 0.$$

This equation approximately models the evolution of the circular interface, with cross-sectional area a at time t and vertical spatial coordinate z , separating a light, viscous fluid rising buoyantly through a heavier, more viscous, miscible fluid at small Reynolds numbers [69, 50]. Our motivation for studying eq. (1.3) is two-fold. First, the conduit equation is not integrable [38] so there are mathematical challenges in analyzing its rich variety of nonlinear wave features. Second, equation (1.3) is an accurate model of viscous fluid conduit interfacial waves where hallmark experiments have been performed on solitary waves [62, 81, 40], their interactions [69, 84, 51], and DSWs [56]. We therefore believe the conduit system is an ideal model for the study of a broad range of dispersive hydrodynamic phenomena. In what follows, we will highlight various work done by others on the conduit equation itself and the implications of this work.

1.2.1 Derivation of the Conduit Equation

The conduit equation is a specific case of the generalized magma equations, which describe the dynamics of melted rock within a solid rock matrix was derived by treating molten rock and its solid, porous surroundings as two fluids with a large density and viscosity difference [59]

$$\phi_t + (\phi^n + m\phi^{n-m-1}\phi_t\phi_z - \phi^{n-m}\phi_{tz})_z = 0, \quad (1.29)$$

where ϕ represents the volume fraction of melted rock [65, 71]. There are two constitutive model parameters (n, m) that relate the porosity of the rock matrix to its permeability and viscosity, respectively. Generally, physically permissible parameter values for (1.29) are $0 \leq m \leq 1$, $2 \leq n \leq 5$. The conduit equation (1.3) coincides with the magma equation (1.29) when $(n, m) = (2, 1)$ [69].

The conduit equation was derived for our experimental system in [50], and the derivation will be summarized here. The derivation begins with the Navier-Stokes equation and the continuity

equation for the interaction between two incompressible fluids [50]

$$\begin{aligned} \nabla \cdot \mathbf{u}^{(i,e)} &= 0 \\ \rho^{(i,e)} \frac{D\mathbf{u}^{(i,e)}}{Dt} &= -\nabla p^{(i,e)} + \nabla \cdot \boldsymbol{\sigma}^{(i,e)} \end{aligned}, \quad 0 < r < L_w, \quad z > 0, \quad t > 0 \quad (1.30)$$

where \mathbf{u} is the flow velocity, $^{(i,e)}$ represents the interior or exterior fluid, respectively, ρ is the density, p is the pressure, t is time, $\frac{D}{Dt}$ is the material derivative

$$\frac{D}{Dt} = \frac{\partial}{\partial t} + \mathbf{u} \cdot \nabla, \quad (1.31)$$

L_w is a far-field boundary assumed far from the fluid interface, and $\boldsymbol{\sigma}$ is the stress tensor (for an incompressible fluid, it depends only on the deformation rate of a fluid element). Everything is described in axisymmetric, cylindrical coordinates, which eliminates any angular dependence for the equations. Therefore, the velocity vectors for the intrusive and exterior fluids can be defined, respectively, as

$$\mathbf{u}^{(i,e)} = \begin{bmatrix} u_r^{(i,e)} \\ u_z^{(i,e)} \end{bmatrix}. \quad (1.32)$$

As shorthand, let any quantity evaluated at the fluid-fluid interface be denoted

$$[f]_j = f^{(e)} - f^{(i)}.$$

Finally denote the viscosity ratio $\varepsilon = \mu^{(i)}/\mu^{(e)}$. This ratio will be assumed small $0 < \varepsilon \ll 1$ for the asymptotic calculation. Initially looking at steady-state pipe (Poiseuille) flow with no-slip boundary conditions at the interior/exterior interface and no surface tension, we find expressions for the intrusive pressure and fluid based on a conduit radius of R_0 :

$$\begin{aligned} p^{(i)} &= (\rho^{(i)} - \rho^{(e)})gz + p_0 \\ u_z^{(i)} &= \frac{g}{4\mu^{(i)}}(\rho^{(e)} - \rho^{(i)})(R_0^2 - r^2) \end{aligned} \quad (1.33)$$

In this case, the vertical velocity of the exterior fluid turns out to be $\mathcal{O}(\varepsilon)$. In actuality, the no-slip boundary condition should be applied to the outer boundary at $r = L_w$ and stress velocity continuity applied at the two-fluid interface.

Next, we assume perturbations around this steady state that depend on appropriate slow-time and slow-space variables, assuming that the length of the perturbation is large relative to its radius R_0 . These assumptions provide the following scalings for nondimensionalization

$$\begin{aligned}
\tilde{r} &= r/L & \tilde{z} &= \varepsilon^{1/2}z/L & L &= R_0/\sqrt{8}, \\
\tilde{\mathbf{u}}^{(i,e)} &= \mathbf{u}^{(i,e)}/U & U &= \frac{gR_0^2(\rho^{(e)}-\rho^{(i)})}{8\mu^{(i)}} & \tilde{t} &= \varepsilon^{1/2}t/(L/U) \\
\tilde{p}^{(i,e)} &= \tilde{P}^{(i,e)} + \tilde{p}_h^{(i,e)} = \varepsilon^{1/2}\frac{p^{(i,e)}-p_0}{\Pi} & \Pi &= \mu^{(i)}U/L & \tilde{p}_h^{(i,e)} &= -\varepsilon^{1/2}\frac{\rho^{(i,e)}gz}{\Pi} = \frac{-\rho^{(i,e)}\tilde{z}}{\rho^{(e)}-\rho^{(i)}}
\end{aligned} \tag{1.34}$$

Tildes will be dropped after this point. Note in the transverse direction, the scaling is L , but in the longitudinal direction, the scaling is $L/\sqrt{\varepsilon}$, $0 < \varepsilon \ll 1$. Thus the amplitude deviation from R_0 can be arbitrarily large, provided the waves are sufficiently long. Velocities are normalized to the radially averaged vertical velocity of the uniform conduit, U . The Reynolds numbers for this system are

$$\text{Re}^{(i,e)} = \frac{\rho^{(i,e)}(\varepsilon^{-1/2}L)U}{\mu^{(i,e)}}.$$

Then the interior fluid equations (1.30) are rescaled to, dropping tildes,

$$\begin{aligned}
\frac{1}{r}\frac{\partial}{\partial r}(ru_r^{(i)}) + \varepsilon^{1/2}\frac{\partial u_z^{(i)}}{\partial z} &= 0 \\
\text{Re}^{(i)}\frac{\text{D}^{(i)}u_r^{(i)}}{\text{Dt}} &= -\varepsilon^{-3/2}\frac{\partial p^{(i)}}{\partial r} + \nabla^2 u_r^{(i)} - \varepsilon^{-1}\frac{u_r^{(i)}}{r^2}, \quad 0 < r < L_w/L, \quad L_w/L \gg 1, \quad z > 0, \quad t > 0 \\
\text{Re}^{(i)}\frac{\text{D}^{(i)}u_z^{(i)}}{\text{Dt}} &= -\varepsilon^{-1}\frac{\partial p^{(i)}}{\partial z} + \nabla^2 u_z^{(i)}
\end{aligned} \tag{1.35}$$

where the superscripted material derivative means the material derivative for that particular fluid, and

$$\nabla = \tilde{\nabla} = \varepsilon^{-1/2}\frac{\partial}{\partial r} + \frac{\partial}{\partial z}, \quad \nabla^2 = \varepsilon^{-1}\frac{1}{r}\frac{\partial}{\partial r}\left(r\frac{\partial}{\partial r}\right) + \frac{\partial^2}{\partial z^2}.$$

For the exterior fluid, the continuity equation is the same other than superscripts, and Navier-Stokes is similar, except for the pressure coefficients:

$$\varepsilon^{-3/2}\frac{\partial \rho^{(i)}}{\partial r} \mapsto \varepsilon^{-1/2}\frac{\partial \rho^{(e)}}{\partial r}, \quad \varepsilon^{-1}\frac{\partial \rho^{(i)}}{\partial z} \mapsto \frac{\partial \rho^{(e)}}{\partial z}$$

For $r = 0$, we continue to assume an even solution with no radial velocity and a pressure extrema, and as $r \rightarrow L_w/L$, we require the fluid velocities and modified pressure decay. For the kinematic

boundary condition, which here will be defined at $r = R_0 + R(z, t)$, we have

$$u_r^{(i)} = \varepsilon^{1/2} \left(\frac{\partial R}{\partial t} + u_z^{(i)} \frac{\partial R}{\partial z} \right).$$

Then the continuity equation is:

$$(u_r^{(e)} - u_r^{(i)}) = \varepsilon^{1/2} \frac{\partial R}{\partial z} \left(u_z^{(e)} - u_z^{(i)} \right).$$

And the no-slip boundary condition is:

$$(u_z^{(e)} - u_z^{(i)}) = \varepsilon^{1/2} \frac{\partial R}{\partial z} \left(u_r^{(i)} - u_r^{(e)} \right).$$

Neglecting surface tension, continuity of the stress tensor in the normal and tangential directions at the interface imply, respectively,

$$\begin{aligned} & \left[-\|\mathbf{n}_c\| P + \kappa \left(\sigma_{rr} - 2\varepsilon^{1/2} \frac{\partial R}{\partial z} \sigma_{rz} + \varepsilon \left(\frac{\partial R}{\partial z} \right)^2 \sigma_{zz} \right) \right]_j = 0 \\ & \left[\kappa \left\{ - \left(1 - \varepsilon \left(\frac{\partial R}{\partial z} \right)^2 \right) \sigma_{rz} + \varepsilon^{1/2} \frac{\partial R}{\partial z} (\sigma_{zz} - \sigma_{rr}) \right\} \right]_j = 0, \end{aligned} \quad (1.36)$$

where \mathbf{n}_c is the unit normal vector to the fluid interface, and κ is a fluid-specific coefficient such that $\kappa^{(e)} = \varepsilon^{-1}$ and $\kappa^{(i)} = 1$.

All pressures and velocities will be expanded in powers of ε , but the scaling for each of these expansions depend on the Poiseuille flow initial state and/or the length scaling ratio. The interior pressure and vertical velocity start at $\mathcal{O}(1)$ (cf. equation (1.33))

$$\begin{aligned} p^{(i)} &= p_0^{(i)} + \varepsilon p_1^{(i)} + \dots, \\ u_z^{(i)} &= u_{z,0}^{(i)} + \varepsilon u_{z,1}^{(i)} + \dots. \end{aligned} \quad (1.37)$$

The exterior pressure and vertical velocity are at $\mathcal{O}(\varepsilon)$.

$$\begin{aligned} p^{(e)} &= \varepsilon p_1^{(e)} + \varepsilon^2 p_2^{(e)} + \dots, \\ u_z^{(e)} &= \varepsilon u_{z,1}^{(e)} + \varepsilon^2 u_{z,2}^{(e)} + \dots. \end{aligned} \quad (1.38)$$

The radial velocities are $\mathcal{O}(\varepsilon^{1/2})$.

$$u_r^{(i)} = \varepsilon^{1/2} u_{r,1}^{(i)} + \varepsilon^{3/2} u_{r,2}^{(i)} + \dots, \quad u_r^{(e)} = \varepsilon^{1/2} u_{r,1}^{(e)} + \varepsilon^{3/2} u_{r,2}^{(e)} + \dots. \quad (1.39)$$

Note that this means for the equation to hold, perturbations of the conduit must be longer than they are wide by a factor of $\varepsilon^{-1/2}$, as assumed in the scalings (1.34). These specific scalings are taken so that a dominant balance involving nonlinearity and dispersion unfolds, as we now show.

To leading order, these equations can be solved; see equations 44-55 in [50]. Of note is the expression for the vertical velocity (the subscript 0 denotes leading order)

$$u_{z,0}^{(i)} \approx \frac{1}{4} \left[1 - \frac{\partial}{\partial z} \left(\frac{2}{R} \frac{\partial R}{\partial t} \right) \right] (R^2 - r^2),$$

which can be used to solve for the volumetric flow rate in terms of the conduit area $A(z, t) = \pi R^2(z, t)$, and the vertical fluid flux in the conduit with normal vector \mathbf{n}_d

$$Q(z, t) = 2\pi \int_0^{R(z,t)} \mathbf{u}^{(i)} \cdot \mathbf{n}_d r \, dr \quad (1.40)$$

$$= \frac{A^2}{8\pi} \left\{ 1 - \frac{\partial}{\partial z} \left(A^{-1} \frac{\partial A}{\partial t} \right) \right\} \quad (1.41)$$

Then using the relation $A_t + Q_z = 0$ (from conservation of mass), and rescaling $a = A/8\pi$, we arrive at the conduit equation (1.3).

We can also deduce the length and temporal scales from equation (1.34) to a few key parameters based on $\mu^{(i,e)}$, $\rho^{(i,e)}$, and R_0

$$a = \frac{1}{\pi R_0^2} A, \quad z = \frac{\sqrt{8\varepsilon}}{R_0} Z, \quad t = \frac{g R_0 \Delta \sqrt{\varepsilon}}{\sqrt{8\mu^{(i)}}} T. \quad (1.42)$$

Then for $0 < \varepsilon \ll 1$ and $\rho^{(i)} < \rho^{(e)}$, the dimensional circular cross-sectional area A of this pipe can be described as a function of dimensional time T and vertical space Z by the dimensional conduit equation

$$A_T + \frac{g\Delta}{8\pi\mu^{(i)}} (A^2)_Z - \frac{\mu^{(e)}}{8\pi\mu^{(i)}} (A^2 (A^{-1} A_T)_Z)_Z = 0. \quad (1.43)$$

1.2.2 Reduction to KdV

The conduit equation (1.3) can be reduced to KdV in the proper regime [83]. To show this, rewrite the conduit equation in the variables $B(\zeta, t) = a(z, t)$ and $Q(\zeta, t) = -a_t(z, t)$, so (1.3)

$$\begin{cases} B_t + Q_\zeta &= 0 \\ Q &= B^2 \left[1 + \left(\frac{Q_\zeta}{B} \right)_\zeta \right], \end{cases} \quad (1.44)$$

Note substituting the first equation into the second yields the nondimensional conduit equation in terms of $B(t, \zeta)$. Then we expand the dependent variables in integer powers of $\varepsilon \ll 1$,

$$\begin{aligned} B &= B_0 + \varepsilon B_1 + \varepsilon^2 B_2 + \dots, \\ Q &= Q_0 + \varepsilon Q_1 + \varepsilon^2 Q_2 + \dots. \end{aligned} \quad (1.45)$$

and change to a slow-time, slow-space, and a moving reference frame, i.e. $\sigma = \varepsilon^{3/2}t$, $Z = \varepsilon^{1/2}(\zeta - c_0 t)$. To leading order,

$$\begin{cases} -c_0 B_{1Z} &= Q_{1Z} \\ Q_1 &= 2B_1 \end{cases}$$

Thus $c_0 = 2$, which is the speed of linear waves in the conduit equation. Then at the next order, substituting in $c_0 = 2$ and $Q_1 = 2B_1$, we have

$$\begin{cases} 2B_{2Z} + B_{1\sigma} &= -Q_2 Z \\ Q_2 &= 2B_{1ZZ} + B_1^2 + 2B_2 \end{cases}$$

Therefore,

$$B_{1\sigma} + 2B_1 B_{1Z} + 2B_{1ZZZ} = 0, \quad (1.46)$$

which is a scaled version of the KdV equation (1.2) [83].

This rescaling is useful for comparing results for the KdV and the conduit equations, which will be done in chapter 4. To that end, the rescaling from the conduit equation (1.3) to the KdV equation (1.2) is given by

$$t = \delta^{3/2}t, \quad x = \delta^{1/2}2^{-1/3}(z - 2t), \quad v = 2^{2/3}\delta(a - 1). \quad (1.47)$$

1.2.3 Conservation Laws and Integrability

The magma equation family (1.29) was of great interest as a magma model in the 1980s-1990s, and the questions of conservation laws and integrability were studied [37, 38]. The conservation laws were assumed to have the form $T_t + X_z = 0$, where T only depends on z -derivatives of ϕ and X holds no such restrictions. Note they exclude the trivial cases

$$T = \Omega_z, X = -\Omega_t,$$

and linear combinations of such a form. The first conservation law for any of the magma equations is the equation itself. In general, there are only two conservation laws for general m and n , unless either i) $m = 1, n \neq 0$, where, there are at least two conservation laws, and ii) $m = n + 1, n \neq 0$, where, there is a third law [37]. The conduit equation is a part of case (i), so it is unknown if there are more than two conservation laws.

Further work on the conduit equation's integrability has also been undertaken [38]. By taking the travelling wave ansatz $\phi(x, t) = \psi(x - ct) := \psi(\xi)$ to reduce the problem to an ODE, then changing the ansatz to $\psi = \alpha(\xi - xi_0)^p$, the equation is

$$c\alpha^3 p[p(1-m) - 1][p(1-m+n) - 2](z - z_0)^{3p-3} \quad (1.48)$$

$$+ np\alpha^{m+2}(z - z_0)^{p(m+2)-1} - cp\alpha^{m-n+3}(z - z_0)^{p(m+n+3)-1} = 0. \quad (1.49)$$

Assuming this is valid in the neighborhood of a movable singularity, the authors examined possible dominant balances, and for each case, added an additional term to ψ ($\psi = \psi + \beta(\xi - z_0)^{p+r}$). If branch point-like behavior is observed (see §3.1 of [38]), then the equation is not of Painlevé type. If an equation is of Painlevé type, then it can generally be rescaled to a known integrable equation, so if an equation is not of Painlevé type, this is another indication of nonintegrability. The conduit equation had a repeated resonance ($r = 0$), which indicates a logarithmic branch point [38]. Further analysis determined there were exactly two cases of m and n that do not fail the Painlevé test: $(m, n) = (0, -1)$, $(m, n) = (\frac{1}{2}, -\frac{1}{2})$. Note these fall under exception (ii) in the conservation laws paper [37]. These equations can be related to other completely integrable

equations: the Hirota-Satsuma and the Maxwell-Bloch equations, respectively.

To summarize, the conduit equation is known to have at least two conservation laws [7, 37]

$$\begin{cases} a_t + (a^2 - a^2(a^{-1}a_t)_z)_z & = 0, \\ \left(\frac{1}{a} + \frac{a_z^2}{a^2}\right)_t + \left(\frac{a_{tz}}{a} - \frac{a_z a_t}{a^2} - 2 \ln a\right)_z & = 0, \end{cases} \quad (1.50)$$

and its failure of the Painlevé test is evidence for its nonintegrability [38].

1.2.4 Other Properties of the Conduit Equation

The conduit equation obeys the scaling invariance

$$\tilde{a} = a/a_0, \quad \tilde{z} = a_0^{-1/2}z, \quad \tilde{t} = a_0^{1/2}t \quad \Rightarrow \quad \tilde{a}_{\tilde{t}} + (\tilde{a}^2)_{\tilde{z}} - (\tilde{a}^2 (\tilde{a}^{-1}\tilde{a}_{\tilde{t}})_{\tilde{z}})_{\tilde{z}} = 0. \quad (1.51)$$

The linearization of the conduit equation upon the background $\bar{\phi}$ admits trigonometric traveling wave solutions subject to the linear dispersion relation

$$\omega_0(k, \bar{\phi}) = \frac{2k\bar{\phi}}{1 + k^2\bar{\phi}}, \quad (1.52)$$

with wavenumber k , similar to the bounded dispersion law of the Benjamin-Bona-Mahony equation.

This leads to the linear phase c_p and group c_g velocities

$$c_p(k, \bar{\phi}) = \frac{\omega_0(k, \bar{\phi})}{k} = \frac{2\bar{\phi}}{1 + k^2\bar{\phi}}, \quad c_g(k, \bar{\phi}) = \omega'_0(k, \bar{\phi}) = \frac{2\bar{\phi}(1 - k^2)}{(1 + k^2\bar{\phi})^2}. \quad (1.53)$$

Note that $c_g < c_p$ for $k > 0$. While the phase velocity is always positive, the group velocity is negative for $k > 1$. We note that the conduit equation is globally well-posed for initial data $a(\cdot, 0) - 1 \in H^1(\mathbb{R})$ with $a(z, 0)$ physically-relevant initial data bounded away from zero in order to avoid a singularity [70].

1.2.5 Solitary Waves

Solitary waves have been studied numerically for the more general magma equation (1.29) where it has been found that they exhibit near-elastic interactions resulting in a phase-shift and a

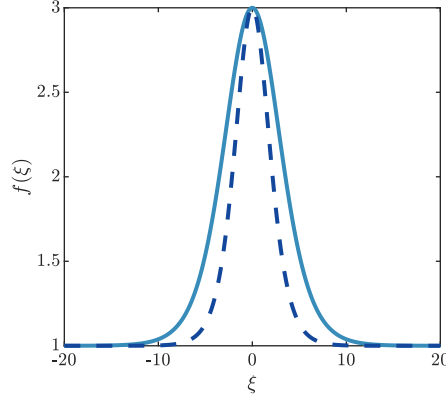


Figure 1.7: (solid, blue) Solitary wave solution to the conduit equation (1.3) with $\mathcal{A}_s = 3$ on a background $\bar{\phi} = 1$. This wave has speed $c_s \approx 2.94$. For comparison, the KdV soliton solution from equation (1.5) with the same parameters is also shown, and has a nondimensional speed of $5/3$.

physically negligible dispersive tail [68, 61, 51]. Since the conduit equation is nonintegrable, true solitons are not possible. However, solitary waves that act as approximate solitons do exist, and the wave profiles can be found numerically as solutions of the ordinary differential equation resulting from the ansatz (1.4) with $\bar{\phi} = \bar{u}$ ($\lim_{|z| \rightarrow \infty} f(\xi) = \bar{\phi}$) to yield

$$(f')^2 = -\frac{2}{c}f^2 \log f + \left(\frac{\bar{\phi} - c + 2 \log \bar{\phi}}{c} + \frac{2}{\bar{\phi}} \right) f^2 - 2f - \frac{\bar{\phi}^2 - c\bar{\phi}}{c} \quad (1.54)$$

If we further assume the solution is of amplitude \mathcal{A}_s measured from $f = 0$ at a maximum ($f(\xi_0) = \mathcal{A}_s$ where $f'(\xi_0) = 0$), we find the solitary wave speed-amplitude relation [62]

$$c_s(\mathcal{A}_s, \bar{\phi}) = \frac{\bar{\phi} \left(2\mathcal{A}_s^2 (\log \mathcal{A}_s - \log \bar{\phi}) - \mathcal{A}_s^2 + \bar{\phi}^2 \right)}{(\mathcal{A}_s - \bar{\phi})^2}. \quad (1.55)$$

An example solitary wave is shown in figure 1.7.

Much of the previous work done on this equation has focused on solitary waves, or solitons, and their interactions with each other and with changes in the background flow [62, 51, 54]. For example, solitary waves were shown to convey mass up the conduit [40]. This can be observed by comparing the difference in speeds between the solitary wave and the background conduit, and concluding that there exist stagnation points on either side of the solitary wave (in a reference frame moving with the wave). Furthermore, there are closed streamlines inside the solitary waves,

which can be shown by defining a streamfunction in the (r, ξ) coordinate system (ξ is the moving reference frame coordinate, r the radial coordinate), then finding the streamline that encloses the trapped fluid [40]. Our own experiments confirm this; a still from an experiment with bicolored interior fluid is shown in figure 1.8. Of interest is the volume of fluid this streamline encircles is less than, but the same order of magnitude as, the volume of the solitary wave itself. At larger amplitudes, the two converge. The asymptotic stability of solitary waves has also been proven [72]. It's also notable that conduit solitary waves exhibit KdV-like interaction behavior including almost elastic interactions and the three Lax interaction categories, even for strongly nonlinear, large amplitude solitary waves [51].

New results for conduit solitary waves will be presented in chapter 5.

1.2.6 Whitham Modulation Equations

Much of the work in this thesis relies on the Whitham modulation framework, which has previously been leveraged to describe dispersive shock waves (DSWs) in the conduit system [52]. General (unmodulated) periodic wave solutions have been found, and an implicit dispersion relation has been computed for these waves [62]. Such a solution for the conduit equation can be found using the ansatz (1.7). Inserting this ansatz into equation (1.3) and integrating twice results in

$$(\phi')^2 = g(\phi) = -\frac{2}{k^2}\phi - \frac{2}{\omega k}\phi^2 \log \phi + C_0 + C_1\phi^2, \quad (1.56)$$

where C_0 and C_1 are real constants of integration. The right side of the equation can have up to three roots, $\phi_1 \leq \phi_2 \leq \phi_3$. As for the KdV equation, if three real roots exist, then so does the periodic wave solution.

We will use the physically relevant parameterization of ϕ is given by the wavenumber k , the wave amplitude \mathcal{A} , and the wave mean $\bar{\phi}$ rather than the parameterization C_0 , C_1 , and k . The wave frequency ω is dependent on $(k, \mathcal{A}, \bar{\phi})$.

Allowing for slow modulations of $\bar{\phi}$, k , and \mathcal{A} in space and time results in the conduit-Whitham equations. Whitham's original formulation invoked averaged conservation laws [86], later

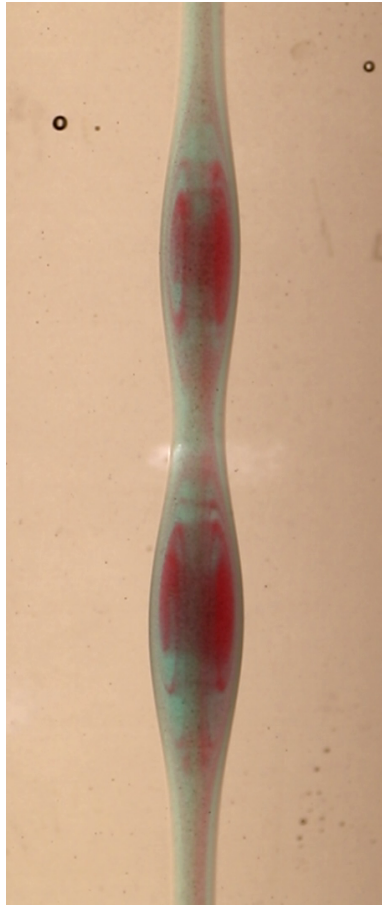


Figure 1.8: Still from an experiment where two interior fluids were used. The two fluids were identical except for the difference in the dye used. Note there are two solitons in the image and the closed streamlines inside [40].

shown to be equivalent to a perturbative, multiple-scales reduction [53]. We use the averaging method to obtain the conduit-Whitham equations from the conduit equation's two conservation laws in (1.50) [7, 37] by averaging over the periodic wave family and appending the equation for conservation of waves [55]. Using the notation for averaging over a wave period

$$\bar{f} = \frac{1}{2\pi} \int_0^{2\pi} f(\theta) d\theta, \quad (1.57)$$

the Whitham equations are

$$\begin{cases} \bar{\phi}_t + \left(\bar{\phi}^2 - 2k\omega\bar{\phi}_\theta^2 \right)_z = 0 \\ \left(\frac{1}{\bar{\phi}} + k^2 \frac{\bar{\phi}_\theta^2}{\bar{\phi}^2} \right)_t - 2(\ln \bar{\phi})_z = 0 \\ k_t + \omega_z = 0 \end{cases} \quad (1.58)$$

We are interested in large $t = T/\varepsilon$, $x = X/\varepsilon$ where $1/\varepsilon \gg 1$ is a time-space scale of interest.

There have been several works applying Whitham modulation theory to the magma equations (1.29). Reference [57] considered equation (1.29) with $(n, m) = (3, 0)$, describing DSWs and some structural properties of the Whitham equations. Modulations of periodic traveling waves in the magma equation (1.29) and a generalization of it were investigated in the weakly nonlinear, KdV regime [26]. Modulated periodic waves in the form of DSWs were investigated for the entire family of magma equations (1.29) in [52]. What is different here is we will focus on the conduit equation (1.3).

This thesis takes a comprehensive look at modulated periodic waves in the context of dispersive hydrodynamics broadly and viscous fluid conduits particularly. We begin with analysis of the conduit equation through our study of the structural properties of the conduit-Whitham equations in chapter 2 [55]. Periodic waves are characterized by wavenumber and amplitude to have modulational stability or instability. Dark and bright envelope solitons are found to persist in long-time numerical solutions of the conduit equation with numerical evidence for the existence of large-amplitude envelope solitons. In the large amplitude regime, structural properties of the Whitham equations are computed, including strict hyperbolicity, genuine nonlinearity, and linear degeneracy.

1.2.7 Dispersive Shock Waves

Dispersive shock waves are the result of a step increase in background conduit area, taken without loss of generality to be from 1 to $\bar{\phi}_-$, and can be characterized by a modulated periodic wave described by the conduit-Whitham equations. Then a DSW can be viewed as connecting two distinguished limits of these wave parameters: as $\mathcal{A} \rightarrow 0$ and $k \rightarrow 0$. When $\mathcal{A} \rightarrow 0$, the solution limits to small amplitude harmonic waves with the linear dispersion relation (1.52). When $k \rightarrow 0$, the solution limits to a leading edge that bears the same characteristics as a solitary wave, with the speed-amplitude relation (1.55).

A simple wave solution to the conduit-Whitham equations results in expressions for the leading (solitary wave) and trailing (harmonic) edge speeds in terms of the jump parameter $\bar{\phi}_-$, labeled s_+ and s_- , respectively [52]

$$s_+ = \sqrt{1 + 8\bar{\phi}_-} - 1, \quad s_- = 3 + 3\bar{\phi}_- - 3\sqrt{\bar{\phi}_-(8 + \bar{\phi}_-)}. \quad (1.59)$$

The solitary wave amplitude \mathcal{A}_+ is implicitly determined from the solitary wave speed-amplitude relation (1.55), and the trailing wavenumber k_- can be explicitly determined by equating the group velocity $\partial_k \omega_0$ to s_-

$$k_-^2 = \frac{1}{4} \left(1 - \frac{4}{\bar{\phi}_-} + \sqrt{\frac{1}{\bar{\phi}_-}(8 + \bar{\phi}_-)} \right). \quad (1.60)$$

The group velocity of the harmonic edge is always less than the speed of the solitary wave edge. Thus, a DSW in the conduit system is always led by a solitary wave, with a trailing, continually expanding, oscillating wavetrain, similar to figure 1.5. Other quantifiable features of conduit DSWs include the onset of backflow, where the group velocity of the trailing edge goes negative, and the onset of implosion, where the trailing edge of the DSW is nonmonotonic in the modulation variables due to gradient catastrophe in the conduit-Whitham equations [52].

We look at the generation and observation of dispersive shock waves in a viscous fluid conduit experiment in chapter 3 [5, 56]. For DSW generation, we can consistently achieve desired jump ratios and breaking heights. We also find excellent agreement with DSW-theory post-breaking, namely theoretical predictions of the leading edge speeds and amplitudes as a function of jump

height as well as the observation of backflow at the trailing edge for sufficiently large jumps. This remarkable agreement motivates further study of dispersive hydrodynamics through this experimental setup.

1.3 Experiments in Viscous Fluid Conduits

Conduits generated by the low Reynolds number, buoyant dynamics of two miscible fluids with differing densities and viscosities were first studied in the context of geological and geophysical processes [82]. Viscous fluid conduits, contrary to magma, are easily accessible in a laboratory setting, typically with a sugar solution or glycerine for the exterior fluid, and a dyed, diluted version of the same for the interior fluid [5, 40, 50, 54, 56, 62, 69, 84]. Early experiments primarily explored the development of the conduit itself, which results in a diapir followed by a periodic wavetrain [62, 82].

1.3.1 Solitary Wave Observation

Previous experiments used a raised reservoir of interior fluid to generate a pressure head that maintained a constant conduit [40]. Moving the reservoir up and down resulted in modulations of that conduit. Similar to our experiments [56], it was reported in [40, 62] that the solitary waves have a constant speed ($R = 0.999$), but the speeds diverge from the expected speed-amplitude relation (1.55) for large-amplitude waves. It was posited in [62] that the slowly-varying assumption of the conduit equation has likely been violated. Interactions of solitary waves have also been studied [51].

1.4 Experimental Setup and Methods

In our experiment, the steady injection of an intrusive viscous fluid (dyed, diluted corn syrup or glycerine) into an exterior, miscible, much more viscous fluid (pure corn syrup or glycerine) leads to the formation of a stable fluid filled pipe or conduit [82]. Due to high viscosity contrast, there is minimal drag at the conduit interface so the flow is well approximated by the Poiseuille or pipe

flow relation. From section 1.2.1, we insert the Poiseuille flow relation for u_z from equation (1.33) into equation (1.40) for volumetric flow rate and evaluate at the steady-state radius R_0

$$\begin{aligned} Q_0 &= 2\pi \int_0^{R_0} \frac{g\Delta}{4\mu^{(i)}} (R_0^2 - r^2) r \, dr \\ &= \frac{\pi g\Delta}{2\mu^{(i)}} \left(\frac{R_0^2}{2} r^2 - \frac{1}{4} R_0^4 \right) \Big|_{r=0}^{R_0} \\ &= \frac{\pi g\Delta}{2^3 \mu^{(i)}} R_0^4. \end{aligned}$$

We more commonly write this in terms of the diameter D_0

$$D_0 = \alpha Q_0^{1/4}, \quad \alpha = \left(\frac{2^7 \mu^{(i)}}{\pi g \Delta} \right)^{1/4} \quad (1.61)$$

By modulating the injection rate, interfacial wave dynamics ensue. Negligible mass diffusion implies a sharp conduit interface and conservation of injected fluid. Typical experiment setup and processing will be laid out in detail here and referenced throughout this work.

1.4.1 Setup

The experimental apparatus shown in figure 1.9(a) consists of a square acrylic column with dimensions $4 \text{ cm} \times 4 \text{ cm} \times 183 \text{ cm}$; the column is filled with the exterior fluid, either glycerine or corn syrup, both highly viscous, transparent fluids. A nozzle is installed at the base of the column to allow for the injection of the interior fluid. To eliminate surface tension effects, the interior fluid is a matching solution of corn syrup or glycerine, diluted with deionized water, and dyed black with food coloring. As a result, the interior fluid has both lower viscosity and density than the exterior fluid ($\mu^{(i)} \ll \mu^{(e)}$, $\rho^{(i)} < \rho^{(e)}$) and we assume mass diffusion is negligible. This will later be verified for corn syrup in section 3.2.3.

Interior fluid is drawn from a separate reservoir and injected through the nozzle via a high precision computer controlled piston pump. The interior fluid rises buoyantly. By injecting at a constant rate, a vertically uniform fluid conduit is established. This uniform steady state is referred to as the background conduit, and is well-approximated as pipe (Poiseuille) flow, verified in section 3.2.2. A perturbed conduit schematic is shown in figure 1.9(b). Data acquisition is performed using

high resolution cameras equipped with macro lenses aimed at the regions of interest. For images of the full conduit, a high resolution camera with a zoom lens is mounted on a tripod an appropriate distance from the apparatus. A ruler is positioned beside the column within camera view for calibration purposes. Correction for the refractive index of glycerin is calibrated via images of a cylinder of known height and width dropped into the center of the apparatus before the experiment.

1.4.2 Methods

Inputs for this system are in the form of a boundary condition $a(0, t)$. Then to utilize a given boundary condition, we transform from the nondimensional conduit equation (lower case variables) to physical parameters (upper case variables). Following the scaling in (1.42) and the Poiseuille flow relation equation (1.61), volumetric flow rate profile $Q(t)$ is generated for the desired configuration and programmed into a computer-controlled piston pump.

The macro lens cameras take images before, during, and after the times of interest, so conduit diameters can be measured. The fluid column is backlit with strip LED lights behind white diffusion filter paper. The conduit edges are extracted from filtered camera images in MATLAB by identifying extreme intensity differences. The approximately white background and the opaque, black conduit yield sufficient contrast for edge detection via horizontal intensity slices, as illustrated in figure 1.10. The edge data is then processed with a low-pass filter to reduce noise due to pixelation of the photograph and any impurities (such as bubbles) in the exterior fluid. The number of pixels between the two edges is identified as the conduit diameter, which is squared and normalized by the squared background conduit diameter to obtain the dimensionless cross-sectional area a [56, 5]. From here, processing techniques diverge due to experimental differences and thus will be explained in the relevant chapters.

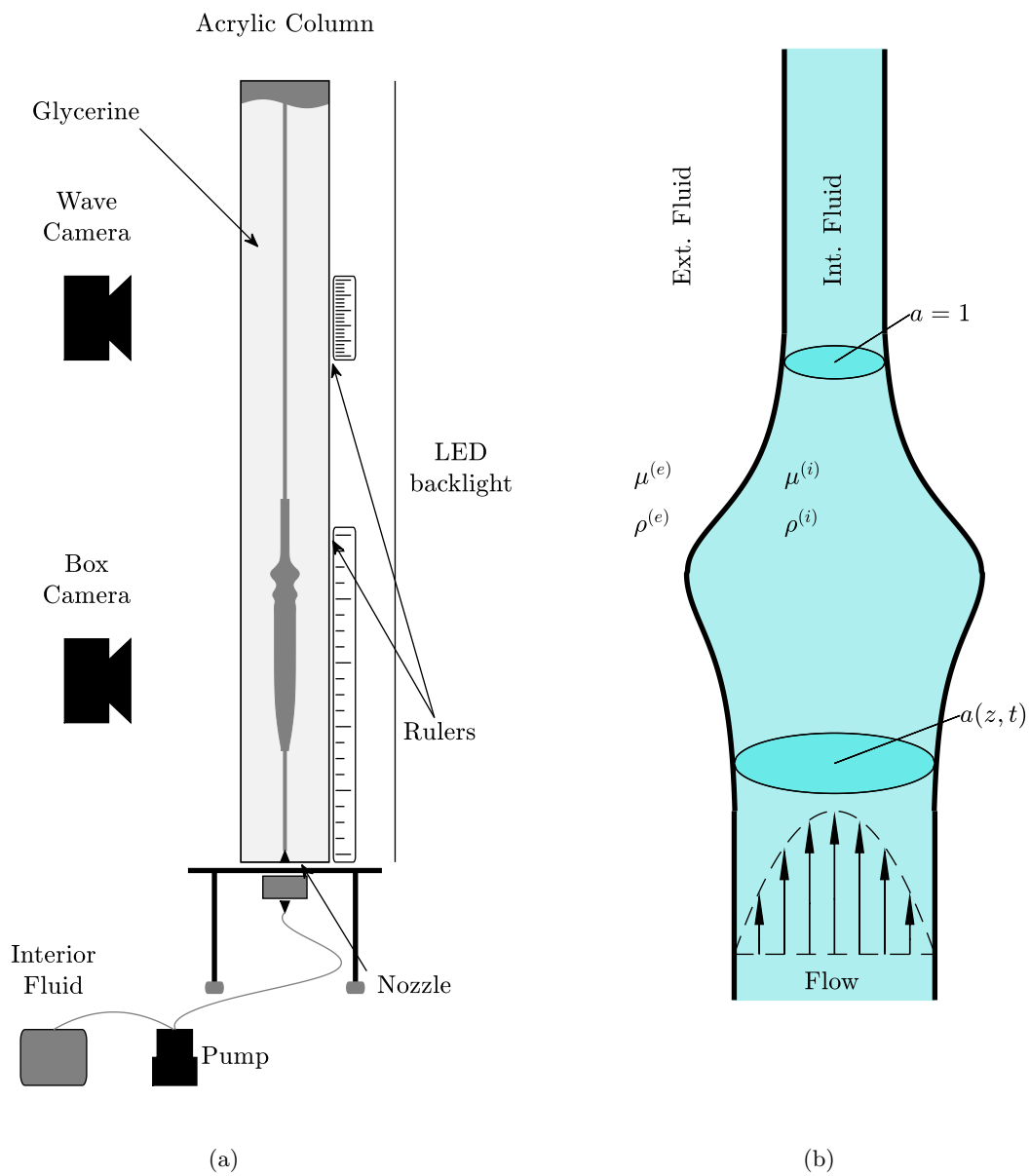


Figure 1.9: (a) Schematic of a possible experimental setup. (b) Schematic of a perturbed conduit [5].

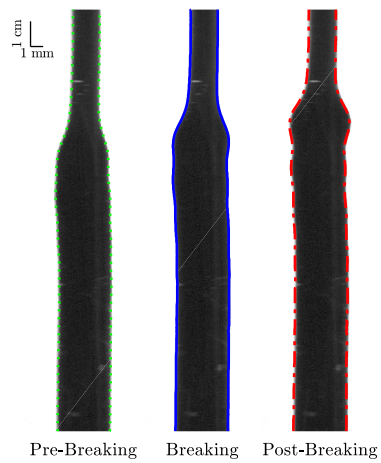


Figure 1.10: Processed images from a glycerine trial [5]. Measured parameter values are $\mu^{(i)} = 72 \pm 1\text{cP}$, $\rho^{(i)} = 1.222 \pm 0.001\text{g/cm}^3$, $\mu^{(e)} = 1190 \pm 20\text{cP}$, $\rho^{(e)} = 1.262 \pm 0.001\text{g/cm}^3$, and $Q_0 = 0.25 \pm 0.01\text{ml/min}$. The grayscale images are overlaid with the extracted conduit edges.

Chapter 2

Modulations of Periodic Waves

In this chapter, we study nonlinear wave phenomena predicted by equation (1.3) by analyzing its weakly nonlinear Stokes wave and NLS reductions as well as the structural properties of the large amplitude modulation (Whitham) equations, and then compare these predictions with numerical simulations. An example non-modulated periodic wave is shown in figure 2.1. We identify long-lived bright and dark envelope soliton solutions in both the weakly nonlinear, NLS regime and the large amplitude, strongly nonlinear regime. The weakly and strongly nonlinear quasi-linear Whitham equations are analyzed asymptotically and with numerical computation. Regions in parameter space of strict hyperbolicity, ellipticity, and linear degeneracy are identified. The elliptic regime corresponds to modulationally unstable periodic waves and a maximally unstable wave is identified. This chapter is a lightly edited version of [55], formatted to fit the style of this thesis.

As mentioned in the introduction, there have been several previous studies on the Whitham modulation equations for the family of magma equations. This work differs from previous studies by concentrating on the case $(n, m) = (2, 1)$ for the conduit equation, identifying new coherent

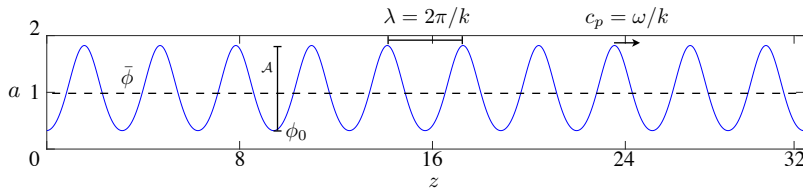


Figure 2.1: A computed periodic wave solution to the conduit equation with wavenumber $k = 2$, amplitude $\mathcal{A} = 1.5$, and unit mean $\bar{\phi}$.

structures (envelope solitons), and determining structural properties of the associated Whitham equations (hyperbolicity, ellipticity, linear degeneracy). By focusing on the $(n, m) = (2, 1)$ case, we lay the groundwork for future analytical, numerical, and experimental studies in this thesis.

2.1 Periodic Traveling Wave Solutions

We seek periodic traveling wave solutions to equation (1.3) in the form $a(z, t) = \phi(\theta)$, $\theta = kz - \omega t$, $\phi(\theta + 2\pi) = \phi(\theta)$ for $\theta \in \mathbb{R}$. Inserting this ansatz into equation (1.3) yields

$$-\omega\phi' + k(\phi^2)' + \omega k^2(\phi^2(\phi^{-1}\phi')')' = 0. \quad (2.1)$$

Integrating twice results in

$$(\phi')^2 = g(\phi) \equiv -\frac{2}{k^2}\phi - \frac{2}{\omega k}\phi^2 \ln \phi + C_0 + C_1\phi^2, \quad (2.2)$$

where C_0 and C_1 are real integration constants.

Equation (2.2) exhibits at most three real roots [52]. When there are three distinct roots, a periodic solution oscillates between the largest two. The solution can be parameterized by three independent variables. Defining the wave minimum ϕ_0 according to $\phi_0 = \min_{\theta} \phi(\theta)$, we utilize the following physical parametrization

$$\begin{aligned} \text{wavenumber:} & & k, \\ \\ \text{wave amplitude:} & & \mathcal{A} = \max_{\theta \in [0, \pi]} \phi(\theta) - \phi_0, \\ \text{wave mean:} & & \bar{\phi} \equiv \frac{1}{\pi} \int_0^{\pi} \phi(\theta) d\theta = \frac{1}{\pi} \int_{\phi_0}^{\phi_0 + \mathcal{A}} \frac{\phi d\phi}{\sqrt{g(\phi)}}. \end{aligned} \quad (2.3)$$

The requirement that ϕ is 2π -periodic is enforced through

$$\pi = \int_0^{\pi} d\theta = \int_{\phi_0}^{\phi_0 + \mathcal{A}} \frac{d\phi}{\sqrt{g(\phi)}}, \quad (2.4)$$

where in (2.3) and (2.4) we have used the even symmetry of solutions to equation (2.2). Given $(k, \mathcal{A}, \bar{\phi})$, the relations (2.3) and (2.4) determine the wave frequency $\omega = \omega(k, \mathcal{A}, \bar{\phi})$ and the wave minimum $\phi_0 = \phi_0(k, \mathcal{A}, \bar{\phi})$. The extrema requirements $g(\phi_0) = g(\phi_0 + \mathcal{A}) = 0$ determine C_0 and C_1 from equation (2.2).

Due to the scaling invariance equation (1.51), the wave mean can be scaled to unity. This implies that only $\omega(k, \mathcal{A}, 1)$ and $\phi_0(k, \mathcal{A}, 1)$ need be determined. Then the general cases follow according to

$$\omega(k, \mathcal{A}, \bar{\phi}) = \bar{\phi}^{1/2} \omega\left(\bar{\phi}^{1/2}k, \bar{\phi}^{-1}\mathcal{A}, 1\right), \quad \phi_0(k, \mathcal{A}, \bar{\phi}) = \bar{\phi}\phi_0\left(\bar{\phi}^{1/2}k, \bar{\phi}^{-1}\mathcal{A}, 1\right). \quad (2.5)$$

We therefore define the unit-mean nonlinear dispersion relation and traveling wave solution according to

$$\tilde{\omega}(\tilde{k}, \tilde{\mathcal{A}}) = \omega(\tilde{k}, \tilde{\mathcal{A}}, 1), \quad \tilde{\phi}(\theta; \tilde{k}, \tilde{\mathcal{A}}) = \phi(\theta; \tilde{k}, \tilde{\mathcal{A}}, 1). \quad (2.6)$$

We will use the variables $(\tilde{\phi}, \tilde{\omega}, \tilde{k}, \tilde{\mathcal{A}})$ whenever we are assuming a unit mean solution.

2.1.1 Stokes Expansion

We can obtain approximate periodic traveling wave solutions in the weakly nonlinear regime via the Stokes wave expansion [85]:

$$\tilde{\phi} = 1 + \varepsilon\tilde{\phi}_1 + \varepsilon^2\tilde{\phi}_2 + \dots, \quad (2.7)$$

$$\tilde{\omega} = \tilde{\omega}_0 + \varepsilon^2\tilde{\omega}_2 + \dots, \quad (2.8)$$

where $0 < \varepsilon \ll 1$ is an amplitude scale. Inserting this ansatz into equation (2.1), equating like coefficients in ε , and enforcing solvability conditions yields the approximate solution

$$\tilde{\phi}_1(\theta) = \cos \theta, \quad \tilde{\omega}_0(k) = \frac{2\tilde{k}}{1+\tilde{k}^2}, \quad \tilde{\phi}_2(\theta) = \frac{1}{6\tilde{k}\tilde{\omega}_0} \cos 2\theta, \quad \tilde{\omega}_2(\tilde{k}) = \frac{1-8\tilde{k}^2}{48\tilde{k}(1+\tilde{k}^2)}, \quad (2.9)$$

where $\tilde{\omega}_0$ is the unit mean linear dispersion relation (equation (1.52) with $\bar{\phi} = 1$). Setting the amplitude $\tilde{\mathcal{A}} = 2\varepsilon$, the approximate periodic wave solution is

$$\tilde{\phi}(\theta, \tilde{k}, \tilde{\mathcal{A}}) = 1 + \frac{\tilde{\mathcal{A}}}{2} \cos \theta + \frac{\tilde{\mathcal{A}}^2(1+\tilde{k}^2)}{48\tilde{k}^2} \cos 2\theta + \mathcal{O}(\tilde{\mathcal{A}}^3), \quad (2.10)$$

$$\tilde{\omega}(\tilde{k}, \tilde{\mathcal{A}}) = \frac{2\tilde{k}}{1+\tilde{k}^2} + \tilde{\mathcal{A}}^2 \frac{1-8\tilde{k}^2}{48\tilde{k}(1+\tilde{k}^2)} + \mathcal{O}(\tilde{\mathcal{A}}^3). \quad (2.11)$$

In figure 2.2, this solution is compared to numerically computed periodic waves (numerical methods are described in Appendix A.1). The frequency and wave profile of the Stokes expansion accurately

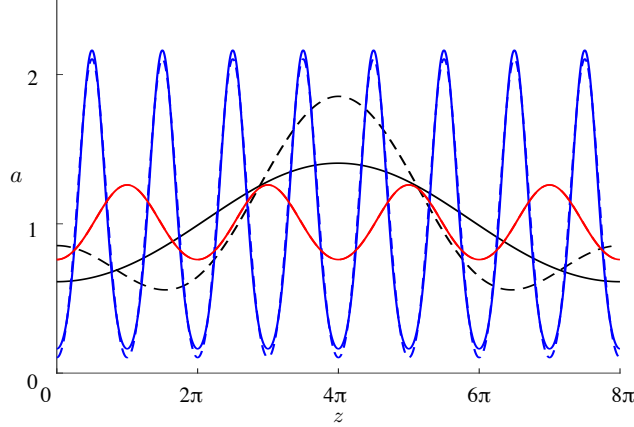


Figure 2.2: Comparison of the Stokes wave expansion solution (dashed lines) to the numerically computed solution (solid lines) for three different waves with unit mean. $(\tilde{k}, \tilde{\mathcal{A}})$ are $(1/4, 1)$ (black), $(2, 2)$ (blue), and $(1, 0.5)$ (red). The approximate and numerical solutions for $(\tilde{k}, \tilde{\mathcal{A}}) = (1, 0.5)$ are indistinguishable.

describe some periodic conduit waves, even for $\mathcal{O}(1)$ amplitudes provided the wavenumber is appropriately chosen. However, even at moderately small wavenumbers, the expansion rapidly breaks down. This is quantified in figure 2.3. Figures 2.3(a,b) show the dispersion and phase velocities for numerically computed periodic waves, and figure 2.3(c) compares the full, nonlinear dispersion $\tilde{\omega}(\tilde{k}, \tilde{\mathcal{A}})$ to $\tilde{\omega}_0(\tilde{k}) + \tilde{\mathcal{A}}^2 \tilde{\omega}_2(\tilde{k})$. The dispersion relation agrees exceedingly well for $\tilde{k} > 1$ and $\tilde{\mathcal{A}} \lesssim 1$, but deviates for larger amplitudes and wavenumbers less than 0.5. To retain asymptotic ordering, we need $\tilde{\mathcal{A}} \ll \tilde{k}^2/(1 + \tilde{k}^2)$.

Note that the approximate solution (2.10) can result in an unphysical, negative conduit cross-sectional area. The minimum of the approximate solution $\tilde{\phi}(\theta)$ occurs when $\theta = \pi$. Equating the minimum to zero, we find that physical, positive values for approximate $\tilde{\phi}$ are restricted to $\tilde{\mathcal{A}} < \mathcal{A}_0$, where $\mathcal{A}_0 > 4(3 - \sqrt{6}) \approx 2.20$, which is well beyond our assumption of small amplitude $0 < \tilde{\mathcal{A}} \ll 1$.

2.2 Weakly Nonlinear, Dispersive Modulations

The aim of this section is to describe wave modulation in the weakly nonlinear, dispersive regime. First, we derive an approximation of wave modulations in the small-amplitude, weakly nonlinear regime with the NLS approximation using the method of multiple scales. Consider the

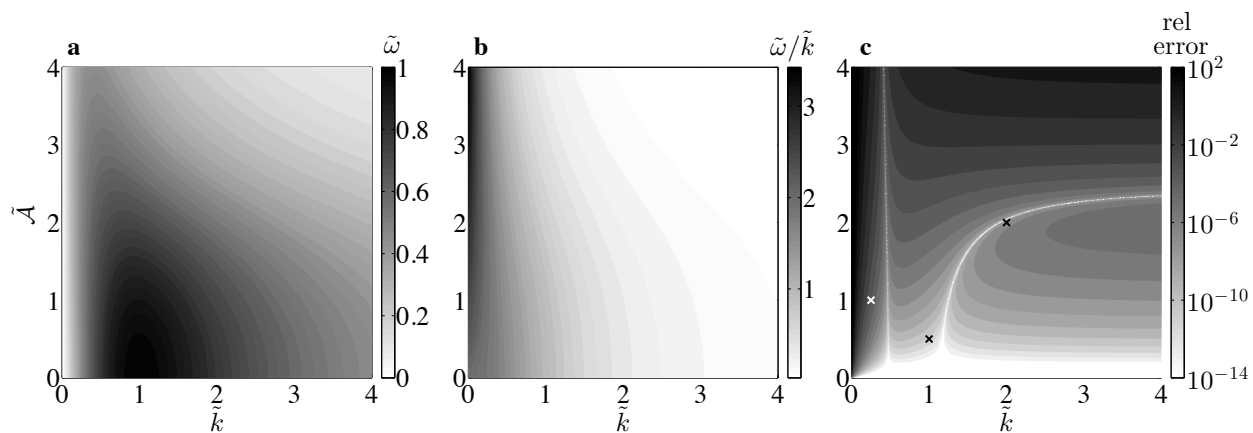


Figure 2.3: (a) Contour plot of numerically computed dispersion relation. (b) Numerically computed phase velocity. (c) Relative error between numerically computed dispersion $\tilde{\omega}(\tilde{k}, \tilde{\mathcal{A}})$ and approximate dispersion $\tilde{\omega}_0(\tilde{k}) + \tilde{\mathcal{A}}^2 \tilde{\omega}_2(\tilde{k})$. Markers (x) correspond to waves plotted in figure 2.2.

ansatz

$$a(z, t) = 1 + \varepsilon A_0 + \varepsilon^2 A_1 + \varepsilon^3 A_2 + \dots, \quad \varepsilon \rightarrow 0, \quad (2.12)$$

where $A_i = A_i(\theta, Z, T)$ for $i = 0, 1, \dots$, $\theta = \tilde{k}z - \tilde{\omega}_0(\tilde{k})t$, $Z = \varepsilon z$, and $T = \varepsilon t$, where $\tilde{\omega}_0(\tilde{k})$ is the linear dispersion relation (1.52) for unit mean. Note that the amplitude in the NLS approximation is small, $\mathcal{O}(\varepsilon)$. Then, at $\mathcal{O}(\varepsilon)$, we obtain a linear, homogeneous equation for A_0 : $\mathcal{L}A_0 := -\omega A_{0,\theta} + 2kA_{0,\theta} + k^2\omega A_{0,3\theta} = 0$, with solution $A_0 = \psi(Z, T)e^{i\theta} + c.c.$ if $\omega = \tilde{\omega}_0$, $k = \tilde{k}$, (*c.c.* denotes the complex conjugate of the previous terms). At $\mathcal{O}(\varepsilon^2)$, $\mathcal{L}A_1 = F_1$ where

$$F_1 = e^{2i\theta} \left[-2i\tilde{k}\psi^2 \right] - e^{i\theta} (1 + \tilde{k}^2) [\psi_T + \tilde{\omega}'_0(\tilde{k})\psi_Z] + c.c.$$

Solvability therefore implies $-(1 + \tilde{k}^2) [\psi_T + \tilde{\omega}'_0(\tilde{k})\psi_Z] \sim \varepsilon g_1 + \dots$, where we have introduced the higher order correction g_1 . Solving for A_1 , we include second harmonic and mean terms $A_1 = \psi^2(Z, T)e^{2i\theta}/(3\tilde{k}\tilde{\omega}) + c.c + M(Z, T)$ with M to be determined at the next order. Solvability with respect to constants at $\mathcal{O}(\varepsilon^3)$ yields $M = (3\tilde{k} - 1)(1 + \tilde{k}^2)\tilde{k}^{-2}(\tilde{k}^2 + 3)^{-1} |\psi|^2$. Solvability with respect to the first harmonic yields for g_1 ,

$$-(1 + k^2) [A_T + \omega'(k)A_Z] = \varepsilon \begin{cases} 2ikm |A|^2 A - ik^2\omega m |A|^2 A - 2ikA_{ZT} \\ +i\omega A_{ZZ} + 2ikBA^* - 9ik^2B\omega A^* \end{cases}$$

Upon entering the moving reference frame and scaling to long time $\xi = Z - \tilde{\omega}'_0 T$, $\tau = \varepsilon T$, yields the Nonlinear Schrödinger equation in the form

$$i\psi_\tau + \frac{\tilde{\omega}''(\tilde{k})}{2} \psi_{\xi\xi} + n(\tilde{k}) |\psi|^2 \psi = 0, \quad (2.13)$$

where

$$n(\tilde{k}) = \frac{3 + 5\tilde{k}^2 + 8\tilde{k}^4}{3\tilde{k}(\tilde{k}^2 + 1)(\tilde{k}^2 + 3)}. \quad (2.14)$$

Rescaling according to

$$\tau = \varepsilon^2 t, \quad \zeta = \frac{\varepsilon}{\sqrt{|\tilde{\omega}''_0|}} (z - \tilde{\omega}'_0 t), \quad B = \frac{\psi}{\sqrt{n}}, \quad (2.15)$$

yields the NLS Equation for the complex envelope $B(\zeta, \tau)$

$$iB_\tau + \frac{\sigma}{2} B_{\zeta\zeta} + |B|^2 B = 0, \quad (2.16)$$

where $\sigma = \text{sgn } \tilde{\omega}_0''(\tilde{k})$ denotes the dispersion curvature. Then given a solution B of the NLS equation, an approximate solution to the conduit equation is

$$a(z, t) \approx 1 + \varepsilon \left[\sqrt{n} B e^{i\theta} + c.c. \right] + \varepsilon^2 \left[\frac{nB^2}{3\tilde{k}\tilde{\omega}_0} e^{2i\theta} + c.c. + M \right], \quad (2.17)$$

$$M = \frac{(3\tilde{k} - 1)(1 + \tilde{k}^2)}{\tilde{k}^2(\tilde{k}^2 + 3)} n |B|^2, \quad n(\tilde{k}) = \frac{3 + 5\tilde{k}^2 + 8\tilde{k}^4}{3\tilde{k}(\tilde{k}^2 + 1)(\tilde{k}^2 + 3)}$$

where ε is an amplitude scale.

Since

$$\tilde{\omega}_0''(\tilde{k}) = \frac{4\tilde{k}(\tilde{k}^2 - 3)}{(1 + \tilde{k}^2)^3},$$

and $n(\tilde{k}) > 0$ in equation (2.14), the NLS equation (2.16) is defocusing when $0 < \tilde{k} < \sqrt{3}$, and focusing for $\tilde{k} > \sqrt{3}$. This result effectively splits periodic wave solutions of the conduit equation into two regimes. For the defocusing case, weakly nonlinear periodic waves are modulationally stable, and dark envelope soliton solutions are predicted, which, when combined with the ansatz (2.17), take the form (see, e.g., [1])

$$B(\zeta, \tau) = e^{i\tau + i\psi_0} [i \cos \alpha + \sin \alpha \tanh[\sin \alpha (\zeta - \cos \alpha \tau - \zeta_0)]], \quad (2.18)$$

with arbitrary, real constants ζ_0 , ψ_0 , and α , where $0 < \alpha \leq \pi/2$ is half the phase jump across the soliton. This ‘‘gray soliton’’ reduces to the ‘‘black soliton’’ when $\alpha = \pi/2$ because $B = 0$ at the soliton center.

For the focusing case, periodic waves are modulationally unstable [87, 91]. Bright envelope soliton solutions for the NLS equation exist, which have the form

$$B(\zeta, \tau) = e^{i\tau/2 + i\Theta_0} \text{sech}(\zeta - \zeta_0), \quad (2.19)$$

where ζ_0 and Θ_0 are arbitrary, real constants.

In order to validate these approximate solutions, we numerically simulate the conduit equation (1.3) with envelope soliton initial conditions (2.17) and (2.18) or (2.17) and (2.19), depicted in figure 2.4(a,b). In figure 2.4(a), a black soliton is observed to coherently propagate, maintaining essentially the same shape. The NLS approximation is asymptotically valid up to times $t = \mathcal{O}(1/\varepsilon^2)$. For the

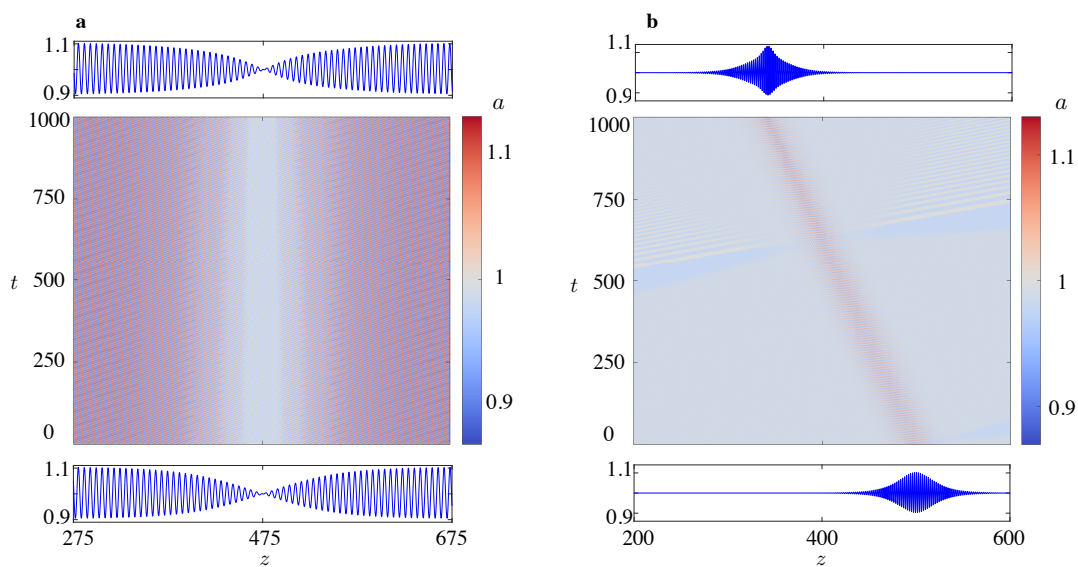


Figure 2.4: Evolution of weakly nonlinear envelope soliton initial conditions for the conduit equation (1.3). (a) Approximate black soliton initial condition (2.18) with $\tilde{\mathcal{A}} = 0.2$, $\tilde{k} = 1$. (b) Approximate bright soliton initial condition (2.19) with $\tilde{\mathcal{A}} = 0.2$, $\tilde{k} = 3$.

simulation in figure 2.4(a), $\varepsilon = \tilde{\mathcal{A}}/4 = 0.05$ so that $1/\varepsilon^2 = 400$. The black envelope soliton shows no sign of instability over times up to $t = 1000$. Figure 2.4(b) shows the long-time evolution of an envelope bright soliton with the same $\varepsilon = 0.05$. The envelope appears to steepen and become peaked by $t = 1000$ but otherwise maintains its envelope structure. The observed speeds of propagation of the black and bright solitons are 0.0002 and -0.1589, respectively, very close to the predicted group velocities 0 and -0.16, respectively.

We also numerically studied the large amplitude regime with dark and bright envelope soliton initial conditions. Figure 2.5(a) shows the numerical evolution of dark envelope soliton initial data for $\tilde{\mathcal{A}} = 1.6$, $\tilde{k} = 1$. The initial data apparently breaks up into three coherent structures. Two shallow amplitude modulations propagate in opposite directions and a large amplitude dip propagates very slowly. In order to verify the coherence of this large amplitude structure, we isolate it from the fast nonlinear waves by extracting the solution at $t = 750$ over the truncated domain $z \in [100, 275]$ and use this as an initial condition for the conduit equation. Additional periods of the unmodulated wave were prepended to the profile in order to increase the spatial domain. The evolution is shown in figure 2.5(b), displaying a remarkable persistence out to $t = 1000$.

Figure 2.6(a) depicts the evolution of bright envelope soliton initial conditions with $\tilde{\mathcal{A}} = 0.6$, $\tilde{k} = 3$. The initial envelope appears to split into two coherent bright envelope structures and small amplitude dispersive radiation. The large amplitude wave is extracted from the solution at $t = 1000$ over the truncated domain $z \in [350, 360]$ and superimposed on a unit background then used as a new initial condition for the conduit equation. The result is shown in figure 2.6(b) that shows the persistence of a large amplitude envelope structure accompanied by the emission of small amplitude dispersive radiation.

These results reflect the fact that the NLS approximation models the envelope of a weakly nonlinear, dispersive carrier wave. Yet numerical evolution of large amplitude initial data present intriguing coherent structures deserving of further study. We now turn to the Whitham equations for an asymptotic description of nonlinear wave modulations in the moderate to large amplitude regime. However, the tradeoff for using these quasi-linear equations is their lack of dispersion at

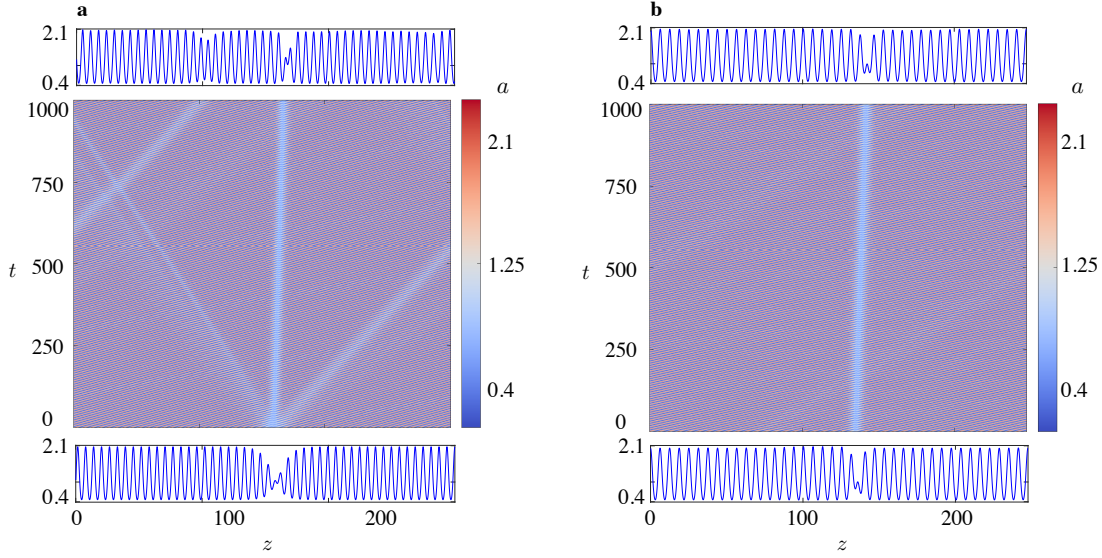


Figure 2.5: Evolution of large amplitude dark envelope soliton initial conditions for the conduit equation (1.3). (a) Approximate black soliton initial condition (2.18) with $\tilde{\mathcal{A}} = 1.6$, $\tilde{k} = 1$ breaking up into multiple coherent “dark” wave structures. (b) The large amplitude dark structure from (a) is isolated and evolved, maintaining its coherence.

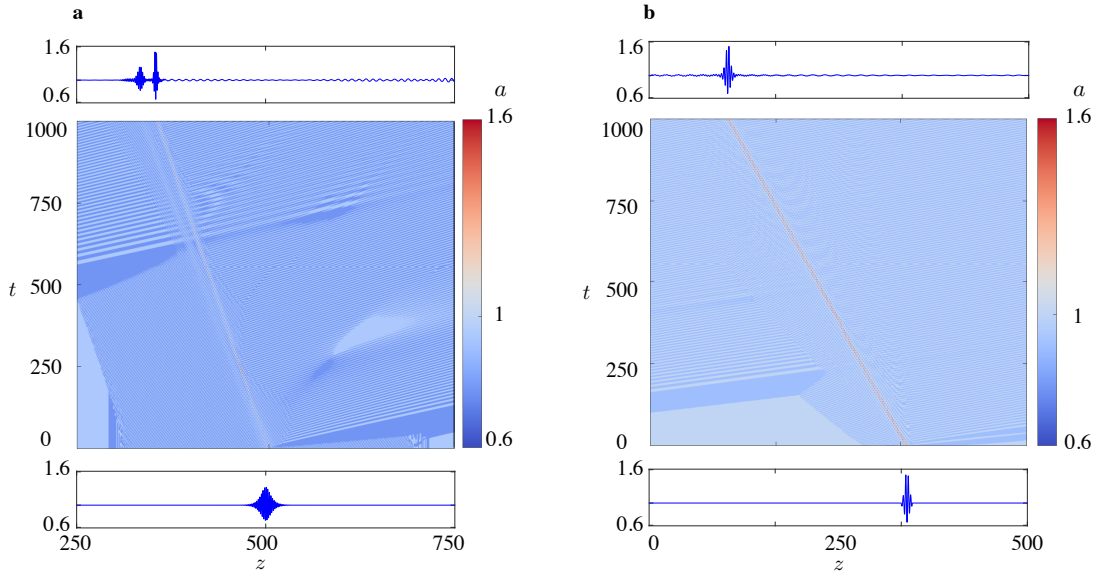


Figure 2.6: Evolution of large amplitude bright envelope soliton initial conditions for the conduit equation (1.3). (a) Approximate bright soliton initial condition (2.18) with $\tilde{\mathcal{A}} = 0.6$, $\tilde{k} = 3$ breaking up into two coherent “bright” wave structures and small amplitude dispersive radiation. (b) The largest amplitude bright structure from (a) is isolated and evolved, maintaining its coherence.

the first order of approximation, consequently they cannot describe envelope solitons.

2.3 Whitham Equations

In order to describe modulated, large amplitude periodic waves, we appeal to the Whitham modulation equations. We have already introduced the conduit-Whitham equations in section 1.2.6 as equation (1.58). Note that the time scale of validity for the leading order Whitham equations is $\mathcal{O}(1/\varepsilon)$, shorter than the $\mathcal{O}(1/\varepsilon^2)$ time scale of the NLS equation (2.16). The benefit of the Whitham equations is that there is no amplitude restriction whereas the NLS equation considers $\mathcal{O}(\varepsilon)$ amplitudes.

For completeness, we supply a synopsis of the multiple scales asymptotic derivation of the Whitham modulation equations. For the formal derivation here, we introduce slow space and time scales $Z = \varepsilon z$, $T = \varepsilon t$ and consider the ansatz $a(z, t) = A_0(\theta, Z, T) + \varepsilon A_1(\theta, Z, T) + \dots$, $0 < \varepsilon \ll 1$, where $\theta_z = k$ and $\theta_t = -\omega$. Note that there is no amplitude restriction on A_0 . Equality of mixed partials $\theta_{zt} = \theta_{tz}$ implies the conservation of waves $k_T + \omega_Z = 0$, one of the Whitham equations. We insert the asymptotic ansatz into the conduit equation (1.3) and equate like orders in ε . The $\mathcal{O}(1)$ equation is

$$-\omega A_{0,\theta} + 2k A_0 A_{0,\theta} - k^2 \omega A_{0,\theta} A_{0,\theta\theta} + k^2 \omega A_0 A_{0,\theta\theta\theta} = 0. \quad (2.20)$$

Equation (2.20) is solved with a family of periodic traveling waves parameterized by $(k, \mathcal{A}, \bar{\phi})$ (see section 2.1) where the parameters are assumed to depend on the slow variables (Z, T) . Note that in order to remove secularity at this order, the period of the solution in θ must be scaled to a constant [53, 87], which we choose to be 2π without loss of generality: $A_0(\theta + 2\pi, Z, T) = A_0(\theta, Z, T)$.

At the next order, $\mathcal{O}(\varepsilon)$, we obtain the linear problem $\mathcal{L}A_1 = f$ where

$$\begin{aligned} \mathcal{L}A_1 &= -\omega A_{1,\theta} + (-k^2 \omega A_{0,\theta} A_{1,\theta} + 2k A_0 A_1)_\theta + k^2 \omega (A_{1,\theta\theta\theta} A_0 + A_{0,\theta\theta\theta} A_1), \\ f &= -A_{0,T} - k^2 A_{0,\theta\theta} A_{0,T} + k^2 A_0 A_{0,\theta\theta T} - 2A_0 A_{0,Z} + 2k\omega A_{0,\theta} A_{0,\theta Z} - 2k\omega A_0 A_{0,\theta\theta Z}. \end{aligned}$$

There are two solvability conditions in the form $\langle w, f \rangle \equiv \int_0^{2\pi} w(\theta) f(\theta) d\theta = 0$, where $w \in \text{Ker } \mathcal{L}^* =$

$\text{span}\{1, A_0^{-2}\}$ for the the adjoint operator

$$\mathcal{L}^* w = \omega w_\theta + k^2 \omega [-(A_{0,\theta} w)_{\theta\theta} + (A_{0,\theta\theta} w)_\theta + A_{0,3\theta} w - (A_0 w)_{3\theta}] + 2k[A_{0,\theta} w - (A_0 w)_\theta],$$

with 2π -periodic boundary conditions. Note that there is a third, linearly independent function that is annihilated by \mathcal{L}^* , but it is not 2π -periodic. Applying the two solvability conditions $\langle 1, f \rangle = \langle A_0^{-2}, f \rangle = 0$, performing some simplifications (primarily integration by parts), and adding the conservation of waves, we arrive at the Whitham equations

$$(\overline{A_0})_T + \left(\overline{A_0^2} - 2k\omega \overline{A_{0,\theta}^2} \right)_Z = 0, \quad (2.21)$$

$$\left(\frac{1}{A_0} + k^2 \frac{A_{0,\theta}^2}{A_0^2} \right)_T - 2(\overline{\ln A_0})_Z = 0, \quad (2.22)$$

$$k_T + \omega_Z = 0, \quad (2.23)$$

where $\bar{g} = \langle 1, g \rangle$. We can set $\varepsilon = 1$, and equivalently consider the Whitham equations in the long time $t \gg 1$ regime. Replacing A_0 with the periodic solution ϕ of equation (1.56), we obtain the Whitham equations in conservative form

$$\mathcal{P}_t + \mathcal{Q}_z = 0, \quad \mathcal{P} = \begin{bmatrix} \overline{\phi} \\ I_1 \\ k \end{bmatrix}, \quad \mathcal{Q} = \begin{bmatrix} I_2 \\ I_3 \\ \omega \end{bmatrix}, \quad (2.24)$$

where we have introduced the averaging integrals

$$I_1 = \overline{\phi^{-1}} + k^2 \overline{g(\phi)/\phi^2}, \quad I_2 = \overline{\phi^2} - 2k\omega \overline{g(\phi)}, \quad I_3 = -2\overline{\ln \phi}. \quad (2.25)$$

Alternatively, averaging of the conservation laws (1.50) is achieved by inserting the ansatz $a(z, t) = \phi(\theta; k(z, t)\mathcal{A}(z, t), \overline{\phi}(z, t))$ and averaging the densities and fluxes over a period:

$$\begin{aligned} \overline{\phi}_t + \left(\overline{\phi^2 + \omega k \phi^2 (\phi^{-1} \phi_\theta)_\theta} \right)_z &= 0, \\ \left(\overline{\frac{1}{\phi} + k^2 \frac{\phi_\theta^2}{\phi^2}} \right)_t + \left(\overline{-\omega k \frac{\phi_{\theta\theta}}{\phi} + \omega k \frac{\phi_\theta \phi_\theta}{\phi^2} - 2 \ln \phi} \right)_z &= 0. \end{aligned}$$

Integration by parts and the addition of conservation of waves yields the Whitham equations in the conservative form (2.24). Consequently we have shown that multiple scales and conservation law averaging yield the same modulation equations.

The density \mathcal{P} and flux \mathcal{Q} can be expanded in terms of the modulation variables $\mathbf{q} = (k, \mathcal{A}, \bar{\phi})^T$ to obtain the quasi-linear form of the Whitham equations

$$\mathbf{q}_t + \mathcal{M}\mathbf{q}_z = 0, \quad (2.26)$$

where

$$\begin{aligned} \mathcal{M} &= \left(\frac{\partial \mathcal{P}}{\partial \mathbf{q}} \right)^{-1} \frac{\partial \mathcal{Q}}{\partial \mathbf{q}} \\ &= \begin{bmatrix} \omega_k & \omega_{\mathcal{A}} & \omega_{\bar{\phi}} \\ \frac{I_{3,k} - I_{1,k}\omega_k - I_{2,k}I_{1,\bar{\phi}}}{I_{1,\mathcal{A}}} & \frac{I_{3,\mathcal{A}} - I_{1,k}\omega_{\mathcal{A}} - I_{2,\mathcal{A}}I_{1,\bar{\phi}}}{I_{1,\mathcal{A}}} & \frac{I_{3,\bar{\phi}} - I_{1,k}\omega_{\bar{\phi}} - I_{2,\bar{\phi}}I_{1,\bar{\phi}}}{I_{1,\mathcal{A}}} \\ I_{2,k} & I_{2,\mathcal{A}} & I_{2,\bar{\phi}} \end{bmatrix}. \end{aligned} \quad (2.27)$$

This non-conservative form of the Whitham equations is only valid where the matrix $\partial \mathcal{P} / \partial \mathbf{q}$ is invertible, which is the case for the parameter regimes considered in this thesis.

The scaling invariance (1.51) can be used so that the dependence on $\bar{\phi}$ in the Whitham equations is explicit and the averaging integrals need be computed only over the scaled variables \tilde{k} and $\tilde{\mathcal{A}}$. Then the integrals (2.25) can be written

$$I_1 = \tilde{I}_1 / \bar{\phi}, \quad I_2 = \bar{\phi}^2 \tilde{I}_2, \quad I_3 = \tilde{I}_3 - 2 \ln \bar{\phi}, \quad (2.28)$$

where $\tilde{I}_i = \tilde{I}_i(\tilde{k}, \tilde{\mathcal{A}})$, $i = 1, 2, 3$. Therefore, computation of the averaging integrals is only required for $(\tilde{k}, \tilde{\mathcal{A}})$. The Whitham equations in the scaled variables $\tilde{\mathbf{q}} = (\tilde{k}, \tilde{\mathcal{A}}, \bar{\phi})$ are

$$\tilde{\mathbf{q}}_t + \tilde{\mathcal{M}}\tilde{\mathbf{q}}_z = 0, \quad \tilde{\mathcal{M}} = \left(\frac{\partial \tilde{\mathbf{q}}}{\partial \tilde{\mathbf{q}}} \right)^{-1} \mathcal{M} \frac{\partial \tilde{\mathbf{q}}}{\partial \tilde{\mathbf{q}}}, \quad \frac{\partial \tilde{\mathbf{q}}}{\partial \tilde{\mathbf{q}}} = \begin{bmatrix} \bar{\phi}^{-1/2} & 0 & -\frac{1}{2}\bar{\phi}^{-3/2}\tilde{k} \\ 0 & \bar{\phi} & \tilde{\mathcal{A}} \\ 0 & 0 & 1 \end{bmatrix}. \quad (2.29)$$

We will be interested in structural properties of the Whitham equations such as hyperbolicity (strict or non-strict), ellipticity, and genuine nonlinearity. All of these criteria rely on the eigenvalues c and eigenvectors \mathbf{r} of the Whitham matrix \mathcal{M} satisfying

$$(\mathcal{M} - c\mathbf{I})\mathbf{r} = 0. \quad (2.30)$$

In general, we expect three eigenpairs $\{(c_j, \mathbf{r}_j)\}_{j=1}^3$ with either all real eigenvalues $c_1 \leq c_2 \leq c_3$ when the Whitham equations are hyperbolic or, in the case of one real and two complex conjugate eigenvalues, the Whitham equations are elliptic. If the eigenvalues are all real and they are strictly ordered $c_1 < c_2 < c_3$, then the Whitham equations are strictly hyperbolic.

The coefficient matrix $\widetilde{\mathcal{M}}$ is a similarity transformation of \mathcal{M} so its eigenvalues are the same as those of \mathcal{M} . $\widetilde{\mathcal{M}}$ exhibits the following property

$$\widetilde{\mathcal{M}}(\tilde{k}, \tilde{\mathcal{A}}, \bar{\phi}) = \begin{bmatrix} 1 & 0 & 0 \\ 0 & 1 & 0 \\ 0 & 0 & \bar{\phi} \end{bmatrix} \widetilde{\mathcal{M}}(\tilde{k}, \tilde{\mathcal{A}}, 1) \begin{bmatrix} \bar{\phi} & 0 & 0 \\ 0 & \bar{\phi} & 0 \\ 0 & 0 & 1 \end{bmatrix}, \quad (2.31)$$

which can be used to show

$$c(\tilde{k}, \tilde{\mathcal{A}}, \bar{\phi}) = \bar{\phi} c(\tilde{k}, \tilde{\mathcal{A}}, 1), \quad \mathbf{r}(\tilde{k}, \tilde{\mathcal{A}}, \bar{\phi}) = \begin{bmatrix} \bar{\phi}^{-1} & 0 & 0 \\ 0 & \bar{\phi}^{-1} & 0 \\ 0 & 0 & 1 \end{bmatrix} \mathbf{r}(\tilde{k}, \tilde{\mathcal{A}}, 1). \quad (2.32)$$

Therefore, the hyperbolicity/ellipticity of the Whitham equations is independent of the mean $\bar{\phi}$.

The unit mean eigenvalues \tilde{c} and eigenvectors $\tilde{\mathbf{r}}$ are defined according to

$$\tilde{c}(\tilde{k}, \tilde{\mathcal{A}}) = c(\tilde{k}, \tilde{\mathcal{A}}, 1), \quad \tilde{\mathbf{r}}(\tilde{k}, \tilde{\mathcal{A}}) = \mathbf{r}(\tilde{k}, \tilde{\mathcal{A}}, 1). \quad (2.33)$$

Utilizing the identities in (2.32), we find that the quantity

$$\mu \equiv \nabla_{\tilde{\mathbf{q}}} c(\tilde{k}, \tilde{\mathcal{A}}, \bar{\phi}) \cdot \mathbf{r}(\tilde{k}, \tilde{\mathcal{A}}, \bar{\phi}) = \begin{bmatrix} \tilde{c}_{\tilde{k}} \\ \tilde{c}_{\tilde{\mathcal{A}}} \\ \tilde{c} \end{bmatrix} \cdot \tilde{\mathbf{r}} \quad (2.34)$$

is independent of $\bar{\phi}$, i.e., $\mu = \mu(\tilde{k}, \tilde{\mathcal{A}})$. If $\mu \neq 0$, then the Whitham equations are genuinely nonlinear [87]. For those values of \tilde{k} and $\tilde{\mathcal{A}}$ where $\mu = 0$, the Whitham equations are linearly degenerate. The sign definiteness of μ corresponds to a monotonicity condition that is required for the existence of simple wave solutions to the Whitham equations, of particular importance for the study of DSWs [21].

2.3.1 Weakly Nonlinear Regime

Now consider equation (2.27) in the small \mathcal{A} regime by inserting the Stokes expansion (2.10), (2.11), yielding

$$\mathcal{M} = \begin{bmatrix} \omega_{0,k} & 2\mathcal{A}\omega_2 & \omega_{0,\bar{\phi}} \\ \frac{\mathcal{A}}{2}\omega_{0,kk} & \omega_{0,k} & \frac{\mathcal{A}}{2} \frac{4(1+\bar{\phi}k^2+3\bar{\phi}^2k^4+\bar{\phi}^3k^6)}{(1+\bar{\phi}k^2)^3} \\ 0 & 2\mathcal{A} \frac{1-3\bar{\phi}k^2}{8(1+\bar{\phi}k^2)} & 2\bar{\phi} \end{bmatrix} + \mathcal{O}(\mathcal{A}^2). \quad (2.35)$$

The eigenvalues of \mathcal{M} (characteristic velocities) via (2.32) evaluated at unit mean $\bar{\phi} = 1$ are

$$\begin{aligned} \tilde{c}_1 &= \tilde{\omega}_{0,\tilde{k}} - \frac{\tilde{\mathcal{A}}}{4} \sqrt{-n\tilde{\omega}_{0,\tilde{k}\tilde{k}}} + \mathcal{O}(\tilde{\mathcal{A}}^2), \\ \tilde{c}_2 &= \tilde{\omega}_{0,\tilde{k}} + \frac{\tilde{\mathcal{A}}}{4} \sqrt{-n\tilde{\omega}_{0,\tilde{k}\tilde{k}}} + \mathcal{O}(\tilde{\mathcal{A}}^2), \\ \tilde{c}_3 &= 2 + \mathcal{O}(\tilde{\mathcal{A}}^2), \end{aligned} \quad (2.36)$$

where $n = n(\tilde{k})$ is from equation (2.14). The complex characteristic velocities occur precisely when the NLS equation (2.16) is in the focusing regime, i.e., when $\tilde{k} > \sqrt{3}$. This is to be expected [87]. The requirement $-n\tilde{\omega}_{0,\tilde{k}\tilde{k}} > 0$ for modulational stability is sometimes referred to as the Benjamin-Feir-Lighthill criterion [91]. Note that we must use $-n(\tilde{k})$, as opposed to $\tilde{\omega}_2(\tilde{k})$ from the Stokes expansion (2.9), in the criterion because of the generation of a mean term (cf. [87]).

Next, we determine the approximate eigenvectors $\tilde{\mathbf{r}}_j$ associated with the approximate eigenvalues (2.36) using standard asymptotics of eigenvalues and eigenvectors (see, e.g., [41]). These approximate results are used to compute μ_j , $j = 1, 2, 3$ for $0 < \tilde{\mathcal{A}} \ll 1$ (2.34) (each μ_j is associated with its c_j)

$$\begin{aligned} \mu_1 &= \frac{6k(k^2-3)}{(1+k^2)^3} + \frac{(2k^{10}+43k^8+35k^6+99k^4+243k^2-54)}{6k(k^2+1)^3(k^2+3)^{3/2} \sqrt{-\frac{8k^6}{3} + \frac{19k^4}{3} + 4k^2+3}} \tilde{\mathcal{A}} + \mathcal{O}(\tilde{\mathcal{A}}^2), \\ \mu_2 &= \frac{6k(k^2-3)}{(1+k^2)^3} - \frac{(2k^{10}+43k^8+35k^6+99k^4+243k^2-54)}{6k(k^2+1)^3(k^2+3)^{3/2} \sqrt{-\frac{8k^6}{3} + \frac{19k^4}{3} + 4k^2+3}} \tilde{\mathcal{A}} + \mathcal{O}(\tilde{\mathcal{A}}^2), \\ \mu_3 &= 2. \end{aligned}$$

We find that $\mu_1 = 0$ when

$$\tilde{\mathcal{A}} = 6\sqrt{\frac{2}{5}}3^{3/4}(\sqrt{3} - \tilde{k})^{3/2} + \mathcal{O}\left(\left(\sqrt{3} - \tilde{k}\right)^{5/2}\right), \quad 0 < \sqrt{3} - \tilde{k} \ll 1. \quad (2.37)$$

Along the curve (2.37), the weakly nonlinear Whitham equations are linearly degenerate in the first characteristic field.

We also find linear degeneracy in the second characteristic field: $\mu_2 = 0$ when $\tilde{\mathcal{A}} = 18\tilde{k}^2 + \mathcal{O}(\tilde{k}^4)$, $0 < \tilde{k} \ll 1$. But the weakly nonlinear Whitham equations are nonstrictly hyperbolic when $\tilde{\mathcal{A}} = 12\tilde{k}^2 + \mathcal{O}(\tilde{k}^4)$, $0 < \tilde{k} \ll 1$, as shown by equating $\tilde{c}_2 = \tilde{c}_3$ from equation (2.36). Because nonstrict hyperbolicity implies linear degeneracy [13], there is apparently a contradiction. The reason for this is due to the Stokes approximation that requires $\tilde{\mathcal{A}} \ll \tilde{k}^2$ to maintain an asymptotically well-ordered approximation of equation (2.10) so that both $\mu_2 = 0$ and $\tilde{c}_2 = \tilde{c}_3$ are outside the asymptotic regime of validity.

2.3.2 Large Amplitude Regime

We now investigate modulations of large amplitude, periodic waves by direct computation of the Whitham equations. For this, we examine the Whitham equations in the form (2.29), so that the dependence on $\bar{\phi}$ is explicit. We numerically compute periodic solutions $\tilde{\phi}$ and the corresponding nonlinear dispersion relation $\tilde{\omega}(\tilde{k}, \tilde{\mathcal{A}})$ and unit-mean averaging integrals $\{\tilde{I}_j(\tilde{k}, \tilde{\mathcal{A}})\}_{j=1}^3$ for the equispaced, discrete values $(\tilde{k}_j, \tilde{\mathcal{A}}_l)$, $\tilde{k}_j = j\Delta$, $\tilde{\mathcal{A}}_l = l\Delta$, $j, l = 1, 2, \dots, N$. We chose $N = 4000$, $\Delta = 0.001$ so that $\tilde{k}_N = \tilde{\mathcal{A}}_N = 4$. Derivatives of $\tilde{\omega}$ and \tilde{I}_j with respect to \tilde{k} and $\tilde{\mathcal{A}}$, required in (2.26), are estimated with sixth order finite differences, yielding a numerical approximation of the coefficient matrix $\tilde{\mathcal{M}}$ on the discrete grid.

Using our direct computation of the coefficient matrix $\tilde{\mathcal{M}}$, we determine its eigenvalues $\{\tilde{c}_j(\tilde{k}, \tilde{\mathcal{A}})\}_{j=1}^3$ and plot in figure 2.7(a) the region in the \tilde{k} - $\tilde{\mathcal{A}}$ plane where the Whitham equations are hyperbolic or elliptic. As shown by our weakly nonlinear analysis (2.36), the elliptic region appears for $\tilde{k} > \sqrt{3}$, independent of $\tilde{\mathcal{A}}$ for small $\tilde{\mathcal{A}}$. But our computations show that the region depends strongly on the wave amplitude for larger $\tilde{\mathcal{A}}$.

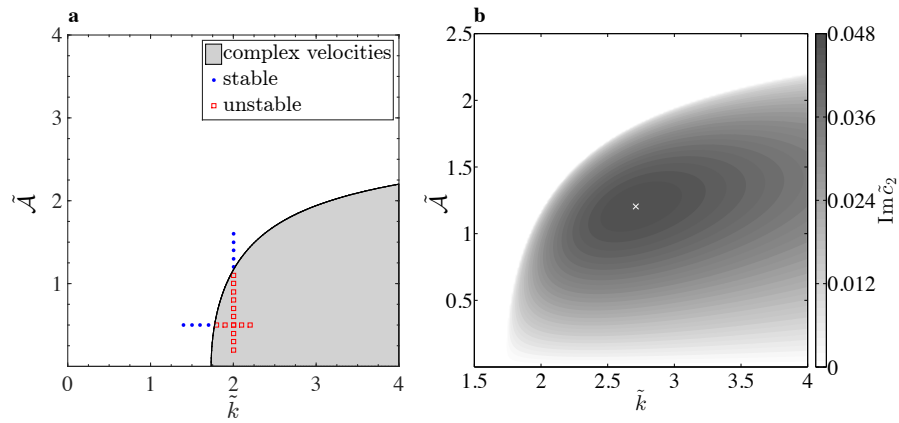


Figure 2.7: (a) Elliptic (gray) and hyperbolic (white) parameter regimes for the Whitham equations corresponding to complex or real characteristic velocities, respectively. Identified stable (dots) and unstable (squares) periodic waves according to direct numerical simulation of the conduit equation. (b) Contour plot of the imaginary part of the characteristic velocity \tilde{c}_2 , the MI growth rate. The maximum, 0.04795, occurs for $(\tilde{k}, \tilde{A}) = (2.711, 1.204)$.

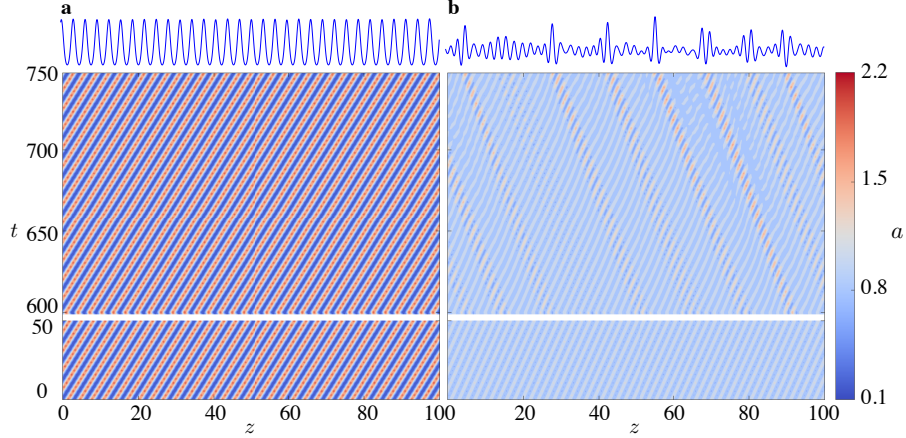


Figure 2.8: Numerical evolution of perturbed periodic wave solutions in the conduit equation. (a) Modulationally stable case: $(\tilde{k}, \tilde{A}) = (2, 2)$. (b) Modulationally unstable case: $(\tilde{k}, \tilde{A}) = (3, 0.5)$. Top: the respective cases at the final time $t = 750$.

As noted earlier, ellipticity of the Whitham equations implies modulational instability of the periodic traveling wave [87]. In agreement with our weakly nonlinear analysis (2.36), we find that in the elliptic region, $\tilde{c}_1 = \tilde{c}_2^*$ (* denotes complex conjugation) and $\tilde{c}_3 \in \mathbb{R}$. We confirm the hyperbolic/elliptic boundary by direct numerical simulation of the conduit equation (1.3) with slightly perturbed, periodic initial data. Random, smooth noise (band-limited to wavenumber 512 on a grid with at minimum 4000 points) of magnitude $\mathcal{O}(10^{-3})$ was added to a periodic traveling wave initial condition on a domain of over 100 spatial periods. This initial data was evolved either 100 temporal periods or to $t = 500$, whichever was longer. Some waves, especially those in the small-amplitude regime, were evolved for even longer time periods. The modulational (in)stability of several of these runs are shown in figure 2.7(a). We find excellent agreement with the MI predictions from Whitham theory. The long-time evolution of two particular waves are shown in figure 2.8, showing both a stable and an unstable case. The unstable case in figure 2.8(b) appears to show the formation of large amplitude, bright envelope coherent structures. This is additional numerical evidence for the existence of bright envelope soliton solutions of the conduit equation.

A periodic traveling wave solution of the conduit equation (1.3) corresponds to a constant solution $\tilde{\mathbf{q}}(z, t) = \tilde{\mathbf{q}}_0$ of the Whitham equations (2.29). If we consider the stability of this solution

by linearizing the Whitham equations according to $\tilde{\mathbf{q}}(z, t) = \tilde{\mathbf{q}}_0 + \mathbf{b}e^{i\kappa z + \sigma t}$, $|\mathbf{b}| \ll 1$, we obtain the growth rates

$$\operatorname{Re} \sigma_i = \kappa \operatorname{Im} c_i, \quad (2.38)$$

for each component of the perturbation in the eigenvector basis of $\tilde{\mathcal{M}}$. The physical growth rate requires knowledge of the perturbation wavenumber κ . Because the Whitham equations are quasi-linear, first order equations, any wavenumber is permissible (determined by the initial data), suggesting that the physical growth rate (2.38) is unbounded. In practice, there is a dominant wavenumber associated with the instability that is determined by higher order effects, which in this case is dispersion. The NLS equation (2.16) resolves this feature in the weakly nonlinear regime but we are interested in large amplitude modulations. We therefore identify the imaginary part of the characteristic velocity \tilde{c}_2 as a proxy for the growth rate of the instability and observe in figure 2.7(b) that there is a maximum of $\operatorname{Im}(\tilde{c}_2)$ for unit-mean periodic waves that occurs for the wave parameters $(\tilde{k}, \tilde{\mathcal{A}}) = (2.711, 1.204)$. We confirm that these parameters do indeed approximately correspond to a maximally unstable periodic wave by performing numerical simulations of the conduit equation (1.3) with initially perturbed periodic traveling waves, utilizing the same process as that used in the determination of modulational (in)stability. The envelopes of these waves were extracted for each time step and then compared to the envelope of the initial condition, giving a deviation from the expected periodic wave evolution. The growth rate was calculated by fitting an exponential to the maximum of this deviation. From these numerics, the maximally unstable parameters are closer to $(\tilde{k}, \tilde{\mathcal{A}}) = (2.7, 1.35)$ than the expected $(\tilde{k}, \tilde{\mathcal{A}}) = (2.7, 1.2)$. The maximal growth rate for these parameters was found to be 0.0457, which is within 5% of the maximal growth rate found via the Whitham equations. Thus the perturbation wavenumber κ does not drastically affect the maximal growth rates.

Next, we compute the quantities $\{\mu_j(\tilde{k}, \tilde{\mathcal{A}})\}_{j=1}^3$ from equation (2.34) on the discrete grid $\{(\tilde{k}_j, \tilde{\mathcal{A}}_l)\}_{j,l=1}^N$ using sixth order finite differencing. The results are depicted in figure 2.9(a) where the curves correspond to the largest value of \tilde{k} , given $\tilde{\mathcal{A}}$, such that μ changes sign. The curve

where μ_1 changes sign bifurcates from the edge of the elliptic region at the point $(\tilde{k}, \tilde{\mathcal{A}}) = (\sqrt{3}, 0)$, agreeing with the weakly nonlinear result (2.37) for sufficiently small $\tilde{\mathcal{A}}$. The curve where both $\mu_{2,3}$ change sign apparently bifurcates from $(0, 0)$ and occurs for small \tilde{k} . These results demonstrate that the Whitham equations lack genuine nonlinearity when considered in the whole of the hyperbolic region.

In order to understand the small \tilde{k} results better, we show in figure 2.9(b) a zoom-in of this region. The accurate determination of the loss of genuine nonlinearity in this region is numerically challenging because the characteristic velocities $\tilde{c}_{2,3}$ get very close to one another. A more numerically stable calculation is shown by the black dashed curve in figure 2.9(b) where, for each $\tilde{\mathcal{A}}$, it corresponds to the largest \tilde{k} at which $|\tilde{c}_3 - \tilde{c}_2| < 10^{-5}$. For parameters to the left of this curve, the characteristic velocities remain very close to one another. It is well-known that, for example, in the KdV-Whitham equations, the characteristic velocities get exponentially close to one another yet remain distinct in the small wavenumber regime [49, 33]. Because non-strict hyperbolicity implies loss of genuine nonlinearity [13], the proximity of \tilde{c}_2 and \tilde{c}_3 may be affecting the numerical results. It remains to definitively determine if the Whitham equations lose strict hyperbolicity and/or genuine nonlinearity in the small \tilde{k} regime. Note that the curve for which $\mu_1 = 0$ in figure 2.9(a) occurs in a strictly hyperbolic region.

2.4 Discussion and Conclusion

Our study of the structural properties of the conduit Whitham equations sheds some light on recent theoretical and experimental studies of dispersive shock waves. The DSW fitting method allows one to determine a dispersive shock's harmonic and soliton edge speeds, even for non-integrable systems [18]. However, the method is known to break down when the Whitham equations lose genuine nonlinearity in the second characteristic field [52, 21]. It was observed in [52] that the fitting method failed to accurately predict conduit DSW soliton edge speeds for sufficiently large jump heights. Our results here suggest that this could be due to the loss of strict hyperbolicity and/or genuine nonlinearity in the small wavenumber (soliton train) regime.

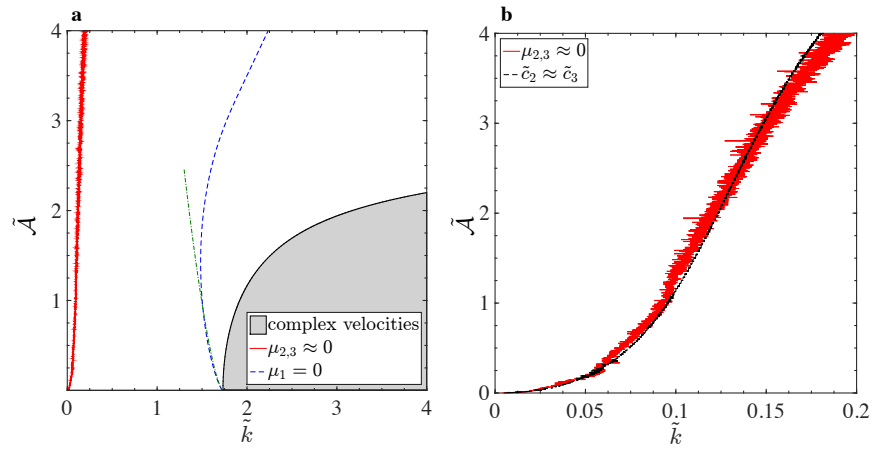


Figure 2.9: (a) Loss of genuine nonlinearity in the Whitham equations. The curves correspond to regions in the \tilde{k} - \tilde{A} plane where the computed quantities $\mu_{2,3}$ (solid) or μ_1 (dashed) change sign. To the right of the solid (dashed) curve, $\mu_3 > 0$, $\mu_2 < 0$ ($\mu_1 > 0$). The dash-dotted curve corresponds to the prediction $\mu_1 = 0$ from the weakly nonlinear analysis equation (2.37). The elliptic region from figure 2.7 is also depicted (gray). (b) Zoom-in of the small \tilde{k} region of (a) where $\mu_{2,3} \approx 0$ (red) approximately corresponds to the largest \tilde{k} , to the left of which $|\tilde{c}_3 - \tilde{c}_2| < 10^{-5}$ (black), i.e., approaching non-strict hyperbolicity.

In addition to the hyperbolic modulation regime where DSWs, and dark envelope solitons are prominent coherent structures, we have found an elliptic regime where the periodic wave breaks up into coherent wavepackets or bright envelope solitons. The accessibility of both hyperbolic and elliptic modulation regimes in one system motivates further study of each and the transition between the two. One potential future, novel direction is to explore the possibility of creating a soliton gas [23].

It remains to generate a periodic wave from an initially uniform conduit and explore its properties experimentally. Accurate control of wavebreaking via a dispersionless simple wave (a rarefaction wave) has been achieved by slow modulation of the conduit area from a boundary [56, 5]. One possibility is to utilize simple wave solutions of the Whitham equations to efficiently and smoothly transition between a constant conduit $\tilde{\mathcal{A}} = 0$ to a periodic conduit $\tilde{\mathcal{A}} > 0$. This also suggests the theoretical and experimental exploration of Riemann problems, step initial data, for the Whitham equations themselves. Our determination of linearly degenerate curves will inform the ability to construct simple waves connecting two generic wave states.

We have presented strong numerical evidence for the existence of large amplitude dark and bright envelope solitary waves in viscous fluid conduits, bifurcating from weakly nonlinear NLS solutions. Dark envelope solitons can have either positive or negative velocities. All bright envelope solitons for NLS associated with the conduit equation have negative velocities. It remains to be determined if this is true in the large amplitude case. Existing laboratory studies of viscous fluid conduits implement control of the conduit interface by varying the injected flow rate through a nozzle at the bottom of a fluid column, as detailed in section 1.4. This allows for the creation of waves with positive (upward) propagation velocities such as dark envelope solitons. If bright envelope solitons only have negative velocities, then an alternative experimental approach will be required to create them.

We have shown that the non-convexity of the conduit linear dispersion relation leads to the existence of elliptic Whitham equations and modulational instability. This is just one possible implication of non-convex dispersion in dispersive hydrodynamics. We note that non-convex dis-

persion in other, higher order equations, has also been found to give rise to a resonance between the DSW soliton edge and linear waves, leading to the generation of radiating DSWs [11, 25, 73].

Chapter 3

Generation and Observation of Dispersive Shock Waves

The Whitham theory developed in chapter 2 and [52] is spectacularly realized during the process of wave breaking into dispersive shock waves for the viscous fluid conduit system. This system enables high fidelity studies of large amplitude DSWs, which are found to agree quantitatively with Whitham theory [87, 34, 50]. The following chapter is a reformatting of [56] and [5] to fit the scope and style of this thesis.

Figure 3.1(a) displays a typical time-lapse of our experiment. At time 0 s, the conduit exhibits a relatively sharp transition between narrower and wider regions. Due to buoyancy, the interface of the wider region moves faster than the narrower region. Rather than experience folding over on itself, the interface begins to oscillate due to dispersive effects as shown in figure 3.1(a) at 30 s. As later times in figure 3.1(a) attest, the oscillatory region expands while the oscillation amplitudes maintain a regular, rank ordering from large to small. By extracting the spatial variation of the normalized conduit cross-sectional area a from a one frame per second image sequence, we display in figure 3.1(b) the full spatio-temporal interfacial dynamics as a space-time contour plot. This plot reveals two characteristic fronts associated with the oscillatory dynamics: a large amplitude leading edge and a small amplitude, oscillatory envelope trailing edge.

3.1 Generation of Wavebreaking Profiles

A major challenge for the experimental study of DSWs is the controlled realization of wavebreaking, e.g. generating the profile seen at $T = 0$ s in figure 3.1(a). One obstacle to the laboratory

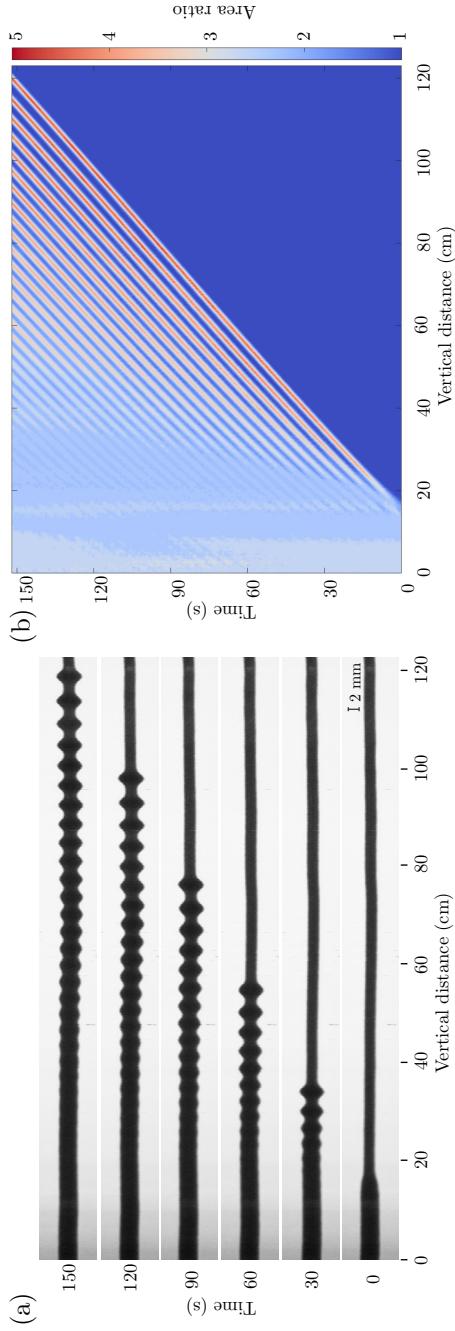


Figure 3.1: Interfacial wave breaking of two Stokes fluids causing the spontaneous emergence of coherent oscillations, a DSW. The leading, downstream edge is approximately a large amplitude solitary wave whose phase speed is tied to the upstream conduit area. The trailing, upstream edge is a small amplitude wave packet moving at the group velocity whose wavenumber is tied to the downstream conduit area. (a) 90° clockwise rotated, time-lapse digital images (aspect ratio 10:1). (b) Space-time contour plot of the conduit cross-sectional area from (a). Nominal experimental parameters: $\Delta\rho = 0.0928 \text{ g/cm}^3$, $\mu^{(i)} = 91.7 \text{ cP}$, $\epsilon = 0.030$, downstream flow rate $Q_0 = 0.50 \text{ mL/min}$, and $a_- = 2.5$.

generation of a desired wavebreaking profile is its reliable initiation from only boundary control. Laboratory nonlinear dispersive wave environments constrained by boundary control include fluid environments such as shallow water wave tanks (see, e.g. [77]) and viscous fluid conduits [69]. Also included are non-fluid systems such as intense laser light propagation in optical fibers [89], magnetic spin waves [43], and granular crystals [10]. It can be difficult to achieve step-like conditions without boundary interactions. Here, we report on a simple mathematical observation that yields a feasible way to achieve a variety of wavebreaking profiles away from boundaries [5]. We track the dispersionless (long-wave) characteristics of the conduit equation backwards in time from the desired wavebreaking profile. The resulting solution is then used as a boundary condition for conduit experiments to realize a variety of wavebreaking profiles at desired spatial locations.

Changing between boundary and initial conditions is a useful tool in the study of nonlinear waves. The piston shock problem is a canonical boundary value problem in the theory of classical shock waves. G. B. Whitham reformulated the problem by tracing characteristics back from the piston to an equivalent initial value problem that was then solved via the method of characteristics [86]. Here, we do the reverse by converting a desired initial value problem into a boundary value problem in the context of dispersive shock waves. We use this approach to precisely realize several wavebreaking profiles in experiment: step, box, triangle, and N-wave configurations. We find that, despite neglecting short-wave dispersion, we can precisely control the location and time of wavebreaking as well as the long-wave characteristics that lead up to breaking. This is supported both theoretically by numerical simulations of the conduit equation and experimentally with our viscous conduit setup.

3.1.1 Theory

The simplest wavebreaking configuration is a step decrease in (dimensional) conduit area

$$A(Z, T_b) = \begin{cases} A_2, & Z < Z_b \\ A_1, & Z \geq Z_b \end{cases}, \quad (3.1)$$

for some $A_2 > A_1 = \pi R_0^2$, where R_0 is the conduit radius, Z_b is the breaking location, and T_b is the breaking time. We can nondimensionalize the equation and rescale the leading area to unity via the scalings (1.42) to arrive at the conduit equation (1.3)

$$a_t + (a^2)_z - (a^2 (a^{-1} a_t)_z)_z = 0.$$

We represent the desired wavebreaking profile via the data $a(z, t_b) = a_0(z)$. For example the step profile (3.1) is

$$a_0(z) = \begin{cases} a_b, & z < z_b \\ 1, & z \geq z_b \end{cases}, \quad z \in \mathbb{R}, \quad (3.2)$$

where $a_b = A_2/A_1 > 1$ is the jump ratio and z_b, t_b are the nondimensional breaking height and time, respectively. We also consider the box profile of amplitude a_b and width w ,

$$a_0(z) = \begin{cases} a_b, & z_b - w < z < z_b \\ 1, & \text{else} \end{cases}, \quad z \in \mathbb{R}, \quad (3.3)$$

the triangle profile of amplitude a_b , width w , and hypotenuse slope $m = \frac{a_b - 1}{w}$,

$$a_0(z) = \begin{cases} mz + (a_b - mz_b), & z_b - w < z < z_b \\ 1, & \text{else} \end{cases}, \quad z \in \mathbb{R}, \quad (3.4)$$

and the N-wave profile of maximum amplitude a_{max} , minimum amplitude a_{min} , width w , and slope $m = \frac{a_{max} - a_{min}}{w}$,

$$a_0(z) = \begin{cases} mz + (a_b - mz_b), & z_b - w < z < z_b \\ 1, & \text{else} \end{cases}, \quad z \in \mathbb{R}. \quad (3.5)$$

For example profiles, see figure 3.2.

3.1.1.1 Inviscid Burgers Equation

In order to approximately realize the breaking configurations that give rise to $a_0(z)$, e.g. (3.2)–(3.5), we seek to identify the spatio-temporal profile for times prior to breaking $t < t_b$.

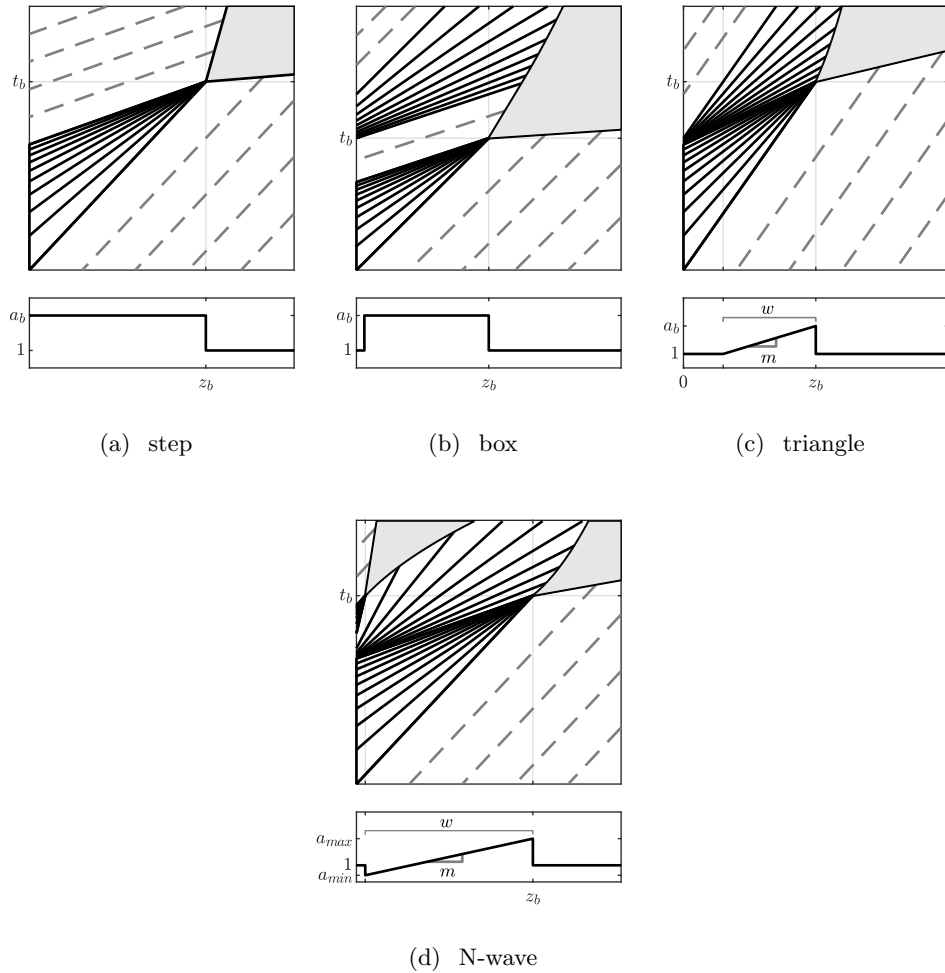


Figure 3.2: Characteristic plots (large plots) and wavebreaking profiles at time of breaking (small plots). The gray regions are areas where wavebreaking has occurred and small-scale dispersion is important so the inviscid Burger's solution is no longer valid. Shown here are step (a), box (b), triangle (c), and N-wave (d) wavebreaking profiles.

We assume that prior to DSW formation, the third order dispersive term is negligible, which we justify with numerical and physical experiments. This is a long-wave assumption that is valid when $|a_z|/|a| \sim |a_t|/|a| \ll 1$, so that nonlinear effects dominate wave dispersion effects. We therefore neglect the dispersive term, $(a^2(a^{-1}a_t)_z)_z$ in (1.3), and reverse time and shift space via

$$z = \zeta + z_b, \quad t = -(\tau - t_b), \quad a = u, \quad (3.6)$$

where $u(\zeta, \tau)$ now satisfies the time-reversed inviscid Burgers equation,

$$u_\tau - (u^2)_\zeta = 0, \quad \tau > 0, \quad \zeta \in \mathbb{R}, \quad (3.7)$$

$$u(\zeta, 0) = u_0(\zeta) = a_0(\zeta - z_b), \quad (3.8)$$

which has the implicit solution

$$u(\zeta, \tau) = u_0(\zeta + 2u(\zeta, \tau)\tau). \quad (3.9)$$

Then, converting (3.9) back to conduit equation variables and evaluating at the boundary $z = 0$, we have an implicit form of the boundary condition in terms of the known initial condition $a_0(z)$,

$$a(0, t) = a_0(-2a(0, t)t). \quad (3.10)$$

Observe the ζ -derivative of $u(\zeta, \tau)$ in equation (3.9) is

$$u_\zeta = \frac{u'_0(\zeta + 2u(\zeta, \tau)\tau)}{1 + 2u'_0(\zeta + 2u(\zeta, \tau)\tau)\tau}.$$

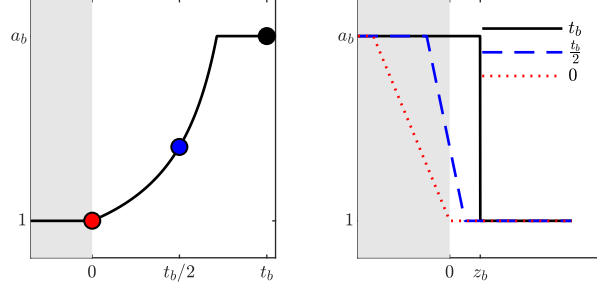
Thus a necessary condition that precludes breaking for $0 < t < t_b$ is $a'_0(z) < 1/2t_b$ for all z .

We now consider the specific case of step data (3.2). For this case, the self-similar, rarefaction wave solution is operable

$$u(\zeta, \tau) = \begin{cases} u_- & : \zeta \leq 2u_- \tau, \\ \frac{\zeta}{2\tau} & : 2u_- \tau \leq \zeta \leq 2u_+ \tau, \\ u_+ & : \zeta \geq 2u_+ \tau. \end{cases} \quad (3.11)$$

The substitution (3.6) along with

$$t_b = \frac{z_b}{2} \frac{a_b - 1}{a_b}, \quad u_- = 1, \quad u_+ = a_b \quad (3.12)$$



(a) Boundary temporal profile. (b) Spatio-temporal development of the wavebreaking profile.

Figure 3.3: (a) Temporal profile of the boundary condition equation (3.13). (b) Evolution of the rescaled rarefaction wave equation (3.13). As time moves forward, the wave approaches the desired step. The dots in (a) correspond to the times depicted in (b), from left to right.

yields the sought for boundary condition

$$a(0, t) = \begin{cases} 1 & : t \leq 0 \\ (1 - 2t/z_b)^{-1} & : 0 < t < \frac{(a_b-1)}{2a_b} z_b \\ a_b & : t \geq \frac{(a_b-1)}{2a_b} z_b \end{cases} \quad (3.13)$$

This solution and its evolution are shown in figure 3.3. Note that we have chosen the specific breaking time t_b in (3.12) so that $a(0, t) = 1$ for $t \leq 0$. Any desired breaking time can be achieved by a simple time shift.

3.1.1.2 Generalizations to Piecewise Linear Profiles

This method of neglecting the dispersive term can be used to generate a variety of initial conditions, the formulae for which are included in table 3.1.

In figure 3.2, we show characteristic plots based on the dispersionless approach to generate a step in figure 3.2(a), a box in figure 3.2(b), a triangle in figure 3.2(c), and an N-wave in figure 3.2(d).

There are some restrictions on the types of profiles we can generate. In order for an entire profile to be above the $z = 0$ boundary at the time of breaking, we require the width of the profile

Profile	Formula	Restrictions
Step	$a(0, t) = \begin{cases} 1 & : \\ (1 - 2t/z_b)^{-1} & : \\ a_b & : \end{cases} \begin{cases} t \leq 0 \\ 0 < t < \frac{(a_b-1)z_b}{2a_b} \\ t \geq \frac{(a_b-1)z_b}{2a_b} \end{cases}$	none
Box	$a(0, t) = \begin{cases} 1 & : \\ (1 - 2t/z_b)^{-1} & : \\ a_b & : \\ 1 & : \end{cases} \begin{cases} t \leq 0 \\ 0 < t < \frac{(a_b-1)z_b}{2a_b} \\ \frac{z_b}{2} \leq t < \frac{z_b}{2} \\ t \geq \frac{z_b}{2} \end{cases}$	$t_b = z_b/2.$
Triangle	$a(0, t) = \begin{cases} 1 & : \\ (1 - 2t/z_b)^{-1} & : \\ \frac{-mz_b + a_b}{1 - mz_b + 2mt} & : \\ 1 & : \end{cases} \begin{cases} t < 0 \\ t < \frac{(a_b-1)z_b}{2a_b} \\ 0 < t < \frac{(a_b-1)z_b}{2a_b} \\ \frac{z_b}{2} \leq t < \frac{z_b}{2} \\ t \geq \frac{z_b}{2} \end{cases}$	$1 \leq \frac{z_b}{w} \leq \frac{1}{a_b-1}$
N-wave	$a(0, t) = \begin{cases} 1 & : \\ (1 - 2t/z_b)^{-1} & : \\ \frac{-mz_b + a_{max}}{1 - mz_b + 2mt} & : \\ \frac{z_b - w}{z_b - 2t} & : \\ 1 & : \end{cases} \begin{cases} 0 \\ t < \frac{(a_{max}-1)z_b}{2a_{max}} \\ 0 < t < \frac{(a_{max}-1)z_b}{2a_{max}} \\ \frac{w}{2} \leq t < \frac{w}{2} \\ t \geq \frac{w}{2} \end{cases}$	$1 \leq \frac{z_b}{w} \leq \frac{1}{a_{max} - a_{min}}$

Table 3.1: Boundary conditions $a(0, t)$ resulting in approximate profiles of interest. All profiles have a breaking time t_b based on the breaking height z_b of $t_b = z_b/2.$

to be less than or equal to z_b . For triangle waves and N-waves, there is an additional width-height ratio that must be satisfied in order for the diagonal portions to be fully realized. These conditions are listed in table 3.1.

3.1.2 Experimental Methods

The experimental setup is as described in 1.4, using glycerine. An example of conduit breaking is shown in figure 3.4.

In order to use the results from section 3.1.1, we rescale (3.13) from the nondimensional conduit equation (lower case variables) to physical parameters (upper case variables) as outlined in section 1.4.2 and map $a(0, t)$ to the volumetric flow rate profile $Q(t)$ for the desired wavebreaking configuration; see table 3.1. A camera near the nozzle takes images before and after the initiation of the boundary volumetric flow profile, so background conduit diameters are measured. Another camera near the breaking height takes several high-resolution images before, during, and after the time of breaking. After breaking occurs, the pump is reduced to the background rate Q_0 , and the conduit is left to equilibrate before the next trial while fluid is extracted from the top of the fluid column.

The images from the camera are processed in MATLAB as described in 1.4.2. We calibrate the ratio $\mu^{(i)}/\Delta$ by fitting the observed diameter data to the Poiseuille flow relation (1.61). We then determine the experimental breaking height z_b and time t_b . Note that near the point of breaking, dispersion is no longer negligible; as a result, a perfect Riemann step is not realized in the conduit system. Instead, we observe the generation of a DSW as seen in the experimental figure 3.4 and the numerical simulation of figure 3.5. Therefore, we introduce a definition of dispersive wavebreaking as follows.

By analyzing numerical simulations of the conduit equation (1.3), e.g. the contour plot in figure 3.5, we developed a robust method to determine the space-time location of wavebreaking using the slope of the wave front. We observe an inflection point in the slope over time that roughly corresponds to the expected breaking time, t_b , as shown in figure 3.6. Then, we interpolate the

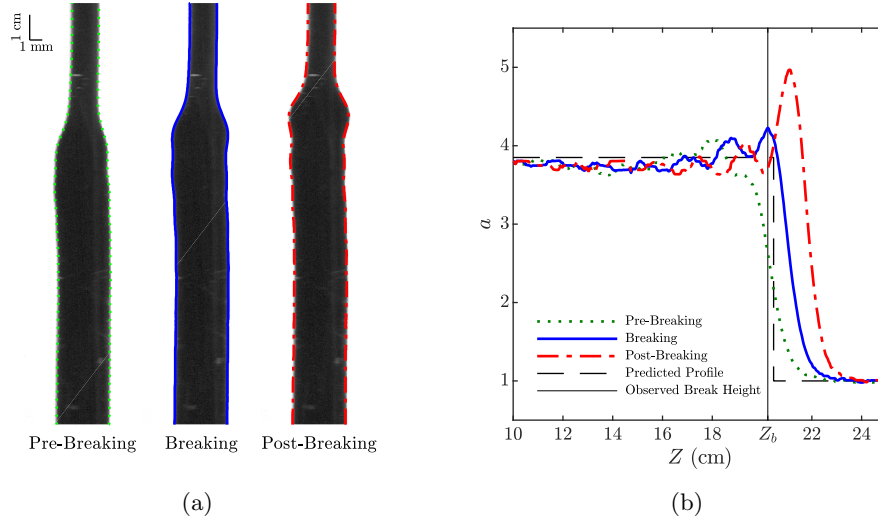


Figure 3.4: (a) Processed images from a glycerine trial. Measured parameter values are $\mu^{(i)} = 72 \pm 1\text{cP}$, $\rho^{(i)} = 1.222 \pm 0.001\text{g/cm}^3$, $\mu^{(e)} = 1190 \pm 20\text{cP}$, $\rho^{(e)} = 1.262 \pm 0.001\text{g/cm}^3$, and $Q_0 = 0.25 \pm 0.01\text{ml/min}$. The grayscale images are overlaid with the extracted conduit edges. (b) Nondimensional area plot corresponding to the images in (a). The vertical line indicates the measured breaking height obtained by the inflection criterion. The dashed line indicates the expected step in a dispersionless system. Predictions were fit to the found Poiseuille flow relation (1.61).

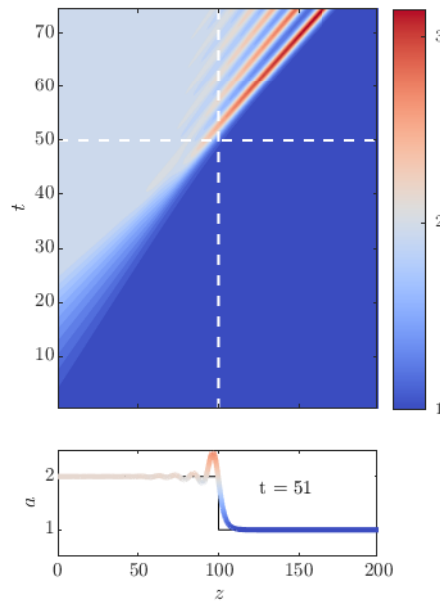


Figure 3.5: Numerical simulation of the conduit equation with initial condition $a(z, 0) = 1$ and the boundary condition equation (3.13) with $z_b = 100$ and $a_b = 2$. The predicted z_b and $t_b = 50$ are marked.

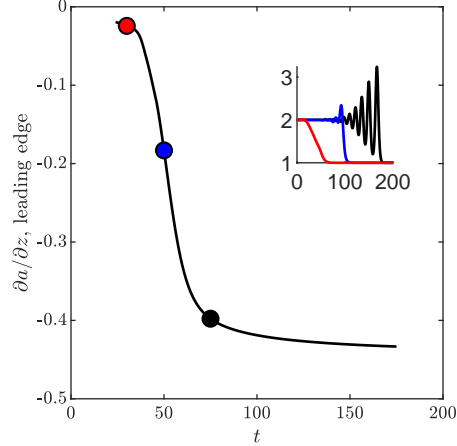


Figure 3.6: Numerics: slope of the front of the evolving structure over time. Inset: three profiles in space corresponding to the marked points in time. Observe dispersion is in full effect by the time the slope of the leading edge has ‘leveled out.’ The expected breaking time of the input boundary condition was $t_b = 50$.

conduit profile to $t = t_b$ and define the point of breaking as the location of the maximum area (leading wave height) of the conduit for the trial.

3.1.3 Results for Wavebreaking Profiles

For the step profile, thirteen trials were taken over the course of four hours. The main results of this experiment are shown in figure 3.7. The predicted breaking heights and times ($z_{b,in}$ and $t_{b,in}$) are very close to the experimentally observed values ($z_{b,out}$ and $t_{b,out}$). Figure 3.7 includes theory, numerics, and experiment for the breaking height (a) and the breaking time (b). All experiments were under 5% relative error in breaking height z_b and 2.5% relative error in breaking time t_b . Therefore, a high degree of wavebreaking control is achieved by our approach.

Experiments were also performed for other wavebreaking profiles. The box profile generation and evolution will be covered in detail in chapter 4. Experiments on boundary conditions for generating triangle waves and N-waves showed qualitative fidelity to the expected shapes, as shown in figure 3.8. For the figure, we fit z_b and t_b to those found experimentally, then generated the predicted characteristics (contours) based on these values. We find this fitting method is equivalent

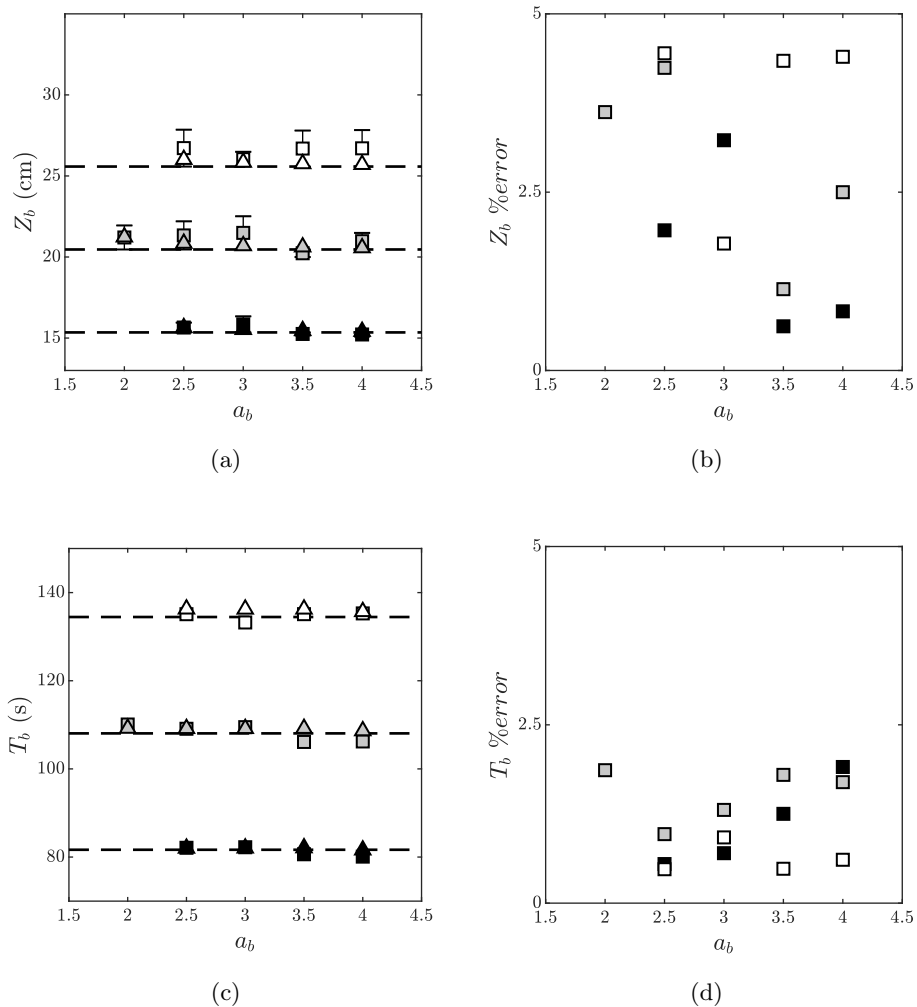


Figure 3.7: Comparison of dispersionless (long-wave) theory (dashed lines), full conduit equation numerics (triangles) and glycerine experiments (squares) for the step wavebreaking configuration. (a) Breaking height results and (b) relative error for experiments as a function of jump ratio a_b , with the same fluid parameters as those in figure 3.4. (c) Breaking time results and (d) relative error for those same experiments. Note the breaking time error bars are smaller than the symbols used. The black squares correspond to an expected $z_b = 15.3$ cm, the gray to $z_b = 20.5$ cm, and the white to $z_b = 25.6$ cm.

to fitting $\mu^{(i)}/\Delta$ to the data, similar to what was done for the step profile.

3.1.4 Conclusions about Wavebreaking Profiles

We have performed numerical and physical experiments to validate the use of a long-wave hyperbolic model (inviscid Burgers’ equation) of nonlinear wave propagation at the interface of a viscous fluid conduit prior to wavebreaking. The pre-breaking validity of the hyperbolic model enables the precise creation of desired wavebreaking profiles in the interior of the dispersive hydrodynamic domain with only boundary control. Characteristics are propagated backward in time from a desired profile until they reach the boundary. So long as the backward characteristics do not overlap, it is possible to obtain a boundary condition whose forward propagation approximately results in the desired wavebreaking profile. For a step profile, the observed breaking values are within 5% and 2.5%, respectively, of their expected values. For more complex profiles—the triangle and N-wave configurations—we obtain good characteristic control observed in measured space-time contour plots. The method holds promise for other dispersive hydrodynamic media.

3.2 Post-Wavebreaking Interpretation

We can interpret the dynamics of a step post-wavebreaking as a DSW resulting from the physical realization of the Gurevich-Pitaevskii (GP) problem [34], a standard textbook problem for the study of DSWs [21] that has been inaccessible in other dispersive hydrodynamic systems. Here, the GP problem is the dispersive hydrodynamics of an initial jump in conduit area. Although we have only boundary control of the conduit width, our carefully prescribed injection protocol from section 3.1 enables delayed breaking far from the injection site. This allows for the isolated creation and long-time propagation of a “pure” DSW connecting two uniform, distinct conduit areas. Related excitations in the conduit system were previously interpreted as periodic wave trains modeling mantle magma transport [69]. As we now demonstrate, the interfacial dynamics observed here exhibit a solitary wave-like leading edge propagating with a well-defined nonlinear phase velocity, an interior described by a modulated nonlinear traveling wave, and a harmonic wave

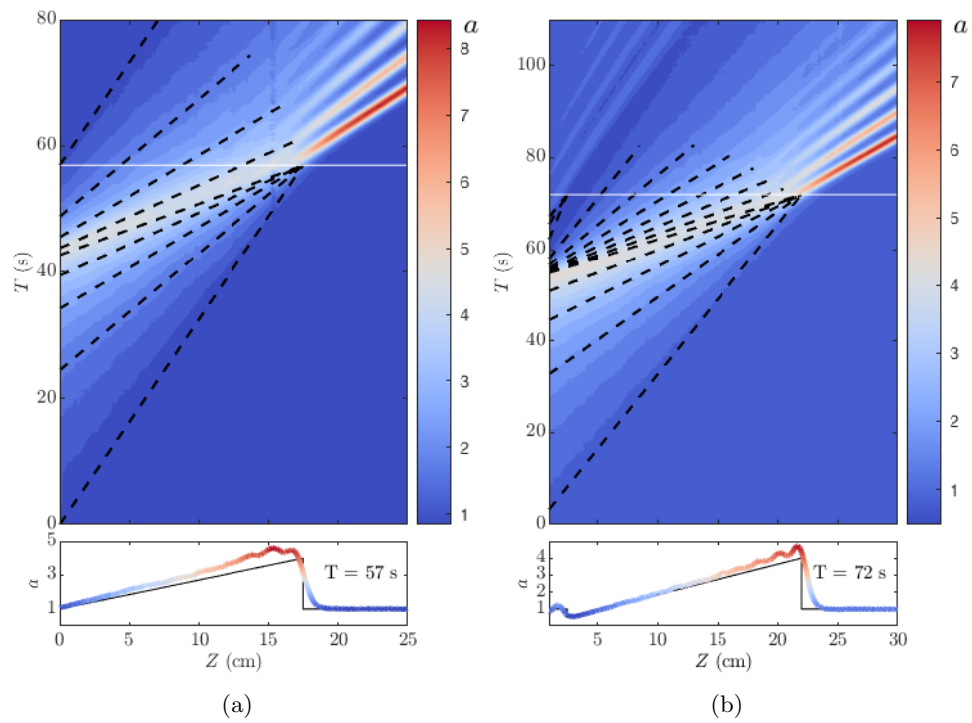


Figure 3.8: Experimental data for (a) triangle wave and (b) N-wave boundary conditions. Overlay lines: fitted characteristic data for the respective experiments.

trailing edge moving with the linear group velocity. The two distinct speeds of wave propagation in one coherent structure are a striking realization of the double characteristic splitting from linear wave theory [87].

The long wavelength approximation of the interfacial fluid dynamics is the conduit equation (1.3) [69, 52]. Both the interface of the experimental conduit system and equation (1.3) exhibit the essential features of frictionless, dispersive hydrodynamics: nonlinear self-steepening (second term) due to buoyant advection of the intrusive fluid, dispersion (third term) from normal stresses, and no dissipation due to the combination of intrusive fluid mass conservation and negligible mass diffusion. The analogy to frictionless flow corresponds to the interfacial dynamics, not the momentum diffusion dominated flow of the bulk.

The study of DSWs involves Whitham modulation theory [87], as studied in chapter 2, as we treat a DSW as an adiabatically modulated periodic wave [34, 21]. Key conduit DSW physical features such as leading solitary wave amplitude and leading/trailing speeds have been determined [50]. For the jump in downstream to upstream area ratio a_- , the conduit-Whitham equations (1.58) predict relatively simple expressions for the DSW leading s_+ and trailing s_- edge speeds (cf. equations (1.59))

$$s_+ = \sqrt{1 + 8a_-} - 1, \quad s_- = 3 + 3a_- - 3\sqrt{a_-(8 + a_-)}, \quad (3.14)$$

in units of the characteristic speed U in equation (1.34). The leading edge moving at speed s_+ approximately corresponds to an isolated solitary wave where the modulated periodic wave exhibits a zero wavenumber. Given the speed s_+ , the solitary wave amplitude \mathcal{A}_+ is implicitly determined from the solitary wave speed-amplitude relation $s_+ = [\mathcal{A}_+^2(2 \ln \mathcal{A}_+ - 1) + 1]/(\mathcal{A}_+ - 1)^2$ in equation (1.55). At the trailing edge, the modulated wave limits to zero amplitude, corresponding to harmonic waves propagating with the group velocity $s_- = \omega'(k_-)$, where $\omega(k)$ is the linear dispersion relation (1.52) of equation (1.3) on a background conduit area a_- and $k_-^2 = (a_- - 4 + \sqrt{a_-(8 + a_-)})/(4a_-)$ is the distinguished wavenumber determined from modulation theory [50] (see also [21]).

3.2.1 Methods

The conduit experimental data are obtained using the methods described in 1.4.2, with the interior fluid an approximately 7:2:1 mixture of corn syrup, water, and black food coloring and the exterior fluid pure corn syrup. The fluid temperature near the top of the fluid column was measured to be 22.2 ± 0.7 deg C across all experimental trials. We allowed the conduit to stabilize (straighten) by steady injection over a period of 36 hours for the data in figure 2 and 15 hours for the other data. Three cameras were utilized, two outfitted with macro lenses positioned just above the injection site and at approximately 120 cm above the injection site. The third camera, outfitted with a zoom lens, was used to image the entire vertical length of 120 cm from the injection site. Digital images of the conduit are processed as described in 1.4.2. Since these are the first experiments done using the setup in 1.4.2, we confirmed various assumptions, including Poiseuille flow and negligible mass diffusion.

3.2.2 Poiseuille Flow

The quantitative data presented here exhibits typical conduit diameters of one to four millimetres and Reynolds numbers in the range $\text{Re} = \rho^{(i)}U_0L_0/\mu^{(i)} \in (0.06, 2.6)$, where $\rho^{(i)}$ is the intrusive fluid density. We confirm the Poiseuille flow relation $D = \alpha Q^{1/4} = (2^7 \mu^{(i)} Q)^{1/4} / (\pi g \Delta \rho)^{1/4}$ by measuring the conduit diameter D approximately 6 cm above the fluid injection site with no fitting parameters (figure 3.9) [82]. In figure 3.10, we show the fit of the Poiseuille flow relation to the same conduit, imaged approximately 120 cm above the injection site. The difference between the externally measured viscosity $\mu^{(i)} = 80.4$ cP and the value $\mu^{(i)} = 104$ cP from a fit to the Poiseuille flow relation can be explained by the non-Newtonian, thixotropic (shear thinning) properties of corn syrup. At the injection site, the diluted corn syrup experiences heightened shearing, similar to our rotational viscometer measurements. Further up the fluid column, there is less shearing so the fluid increases in viscosity and leads to a dilation of the conduit. The conduit consistently has a measured diameter in the upper fluid column that is 7% larger than its value near the injection

site as shown in figure 3.11. The results reported here use the measured value of $\Delta\rho$ and the fitted value $\mu^{(i)} = 104$ cP. Although corn syrup is thixotropic, later experiments with glycerine appears to show this behavior as well, and we interpret this effect in a different way in chapters 4 and 5.

3.2.3 Mass Diffusion

The injected and external fluids are miscible so there is unavoidable mass diffusion across an interface between the two. Using a procedure similar to that described in [64], we estimate the diffusion constant \tilde{D} between a 7:3 corn syrup, water mixture and pure corn syrup (Karo brand light) to be approximately 1.2×10^{-6} cm²/s. Combining this with typical flow parameters, we estimate the Péclet numbers, which are the ratios of the thermal energy convected to the fluid to the thermal energy conducted within the fluid, and Schmidt numbers, which are the ratios of momentum diffusivity and mass diffusivity for the fluid flow. For the trials of figure 2, these lie in the range $Pe = L_0 U_0 / \tilde{D} \in (2.1 \times 10^4, 7.9 \times 10^5)$ and $Sc = Pe/Re \approx 5.2 \times 10^5$. The advective time scale for figure 2 trials is in the range $T_0 \in (1.6, 5.6)$ s. We therefore estimate that mass diffusion begins to play a role after approximately 9 hours ($Sc \cdot T_0$), whereas the time scale of an experimental trial is less than 10 minutes.

3.2.4 Results and Discussion

The leading edge of the DSW amplitude, normalised to the downstream area, is determined from the digital images of the upper camera without appealing to any fluid parameters. The number of pixels across the diameter of the leading edge DSW peak is calculated and normalized by the diameter of the downstream conduit. Squaring this quantity gives the leading edge DSW amplitude shown in figure 3.12. We calculated the leading edge DSW speed from the images of the full camera images toward the end of the trial. We nondimensionalise the speed by the characteristic speed $U = L/T = gA_0\Delta\rho/(8\pi\mu^{(i)})$ (cf. equation (1.34)), where we use the measured values of the downstream flow area A_0 from the upper camera and $\Delta\rho$. The fitted value for $\mu^{(i)}$ is used, as described in the earlier section on Poiseuille flow.

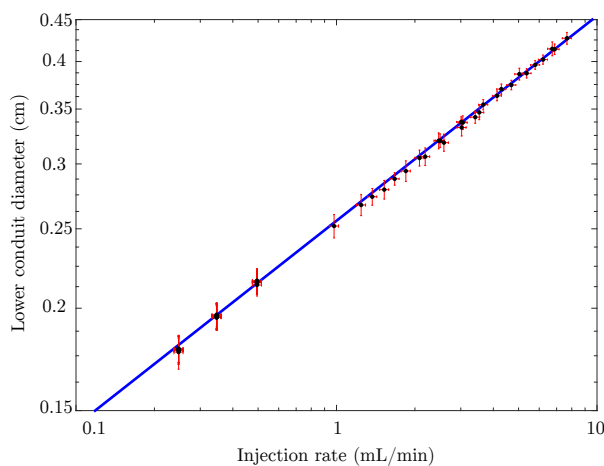


Figure 3.9: Demonstration of Poiseuille flow in a steady viscous fluid conduit. Log-log plot of measured conduit diameter D near injection site versus volumetric flow rate Q (dots) and the relation $D = \alpha Q^{1/4}$ with the measured value $\alpha = 0.2557 \text{ (cm}\cdot\text{min)}^{1/4}$ (solid) corresponding to $\mu^{(i)} = 80.4 \text{ cP}$, $\Delta\rho = 0.1305 \text{ g/cm}^3$. A least squares fit gives $\alpha = 0.2548 \text{ (cm}\cdot\text{min)}^{1/4}$, which translates to the fitted viscosity $\mu^{(i)} = 79.0 \text{ cP}$, within the 2% error tolerance of our rotational viscometer.

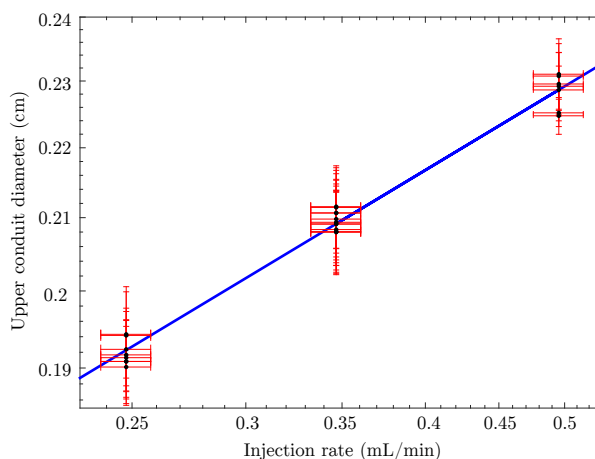


Figure 3.10: Poiseuille flow fit approximately 120 cm up the fluid column. Downstream conduit diameters D extracted from digital images (dots) and a least squares fit to the Poiseuille flow relation $D = \alpha Q^{1/4}$ with $\alpha = 0.2688 \text{ (cm}\cdot\text{min)}^{1/4}$ (solid). The fit corresponds to the interior viscosity $\mu^{(i)} = 104 \text{ cP}$, an increase from its measured value $\mu^{(i)} = 80.4 \text{ cP}$. This can be explained by the shear thinning properties of corn syrup.

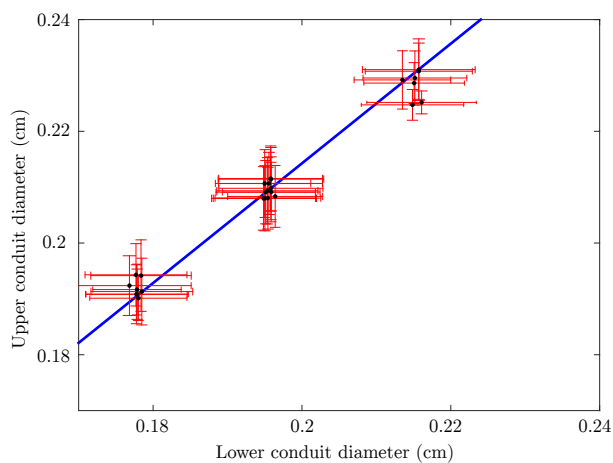


Figure 3.11: Comparison of conduit diameter at different locations along the fluid column. Measurements (dots) and the linear fit $D_{\text{top}} = mD_{\text{bottom}}$ (solid) with $m = 1.07$ corresponding to a 7% increase in the conduit diameter. The lower (upper) diameter was measured approximately 6 cm (120 cm) above the injection site.

In figure 3.12, we compare the leading edge amplitude and speed predictions with experiment, demonstrating quantitative agreement for a range of jump values a_- . Whitham theory is known to break down at large amplitudes [50] so we also include direct determination of the speed and amplitude from numerical simulation of equation (1.3), demonstrating even better agreement (for numerical methods see Appendix A.2). In order to obtain the reported dimensionless speeds of figure 3.12(a), we divide the measured speeds by U with $\mu^{(i)}$ determined by fitting the downstream conduit area to a Poiseuille flow relation. This enables us to self-consistently account for the shear-thinning properties of corn syrup. All the remaining fluid parameters take their nominal, measured values. The deviation between experiment and theory at large jump values is consistent with previous measurements of solitary waves, where the solitary wave dispersion relation was found to underpredict observed speeds at large amplitudes [62].

In addition to single DSWs, our experimental setup allows us to investigate exotic, coherent effects predicted by equation (1.3) for the first time. For example, backflow is a feature of dispersive hydrodynamic systems whereby a portion of the DSW envelope propagates upstream. This feature occurs here when the group velocity of the trailing edge wave packet is negative. From the expression for s_- in (3.14), we predict the onset of backflow when a_- exceeds $8/3$. In figure 3.13, we utilize our injection protocol to report the observation of this phenomenon in the viscous conduit setting. Waves with strictly positive phase velocity are continually generated at the trailing edge but the envelope group velocity is negative. This behavior is reminiscent of slow light in optical systems where manipulation of the propagation medium's dispersion properties enables the effective slowing down or stopping of light [39]. We estimate the crossover to backflow for the experiments reported in figure 3.12 at $a_- \approx 3$, consistent with a slightly larger crossover than theory ($8/3$) due to sub-imaging-resolution of small amplitude waves.

Viscous liquid conduits are a model system for the coherent dynamics of one-dimensional superfluid-like media with microscopic-scale fluid dynamics [84], mesoscopic-scale solitary waves [40] and macroscopic-scale DSWs as fundamental nonlinear excitations. The viscous liquid conduit system is a new environment in which to investigate complex, coherent dispersive hydrodynamics

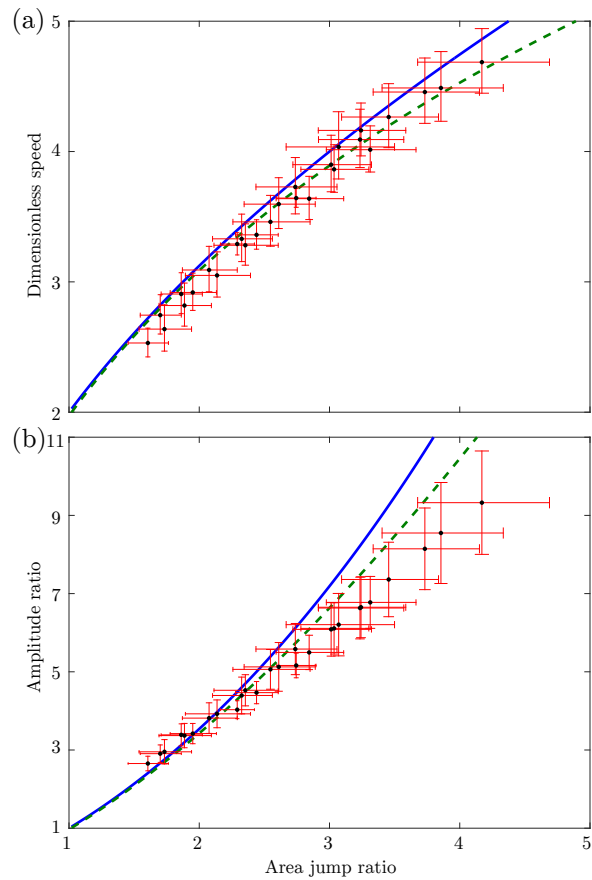


Figure 3.12: Comparison of observed and predicted leading edge DSW amplitude and speed. Observations (circles), Whitham modulation theory (solid), and numerical simulation of the conduit equation (dashed) for (a) DSW leading edge speeds s_+ and (b) DSW leading amplitude \mathcal{A}_+ versus downstream area ratio a_- . Nominal experimental parameters: $\Delta\rho = 0.1305 \text{ g/cm}^3$, $\mu^{(i)} = 80.4 \text{ cP}$ (measured), $\mu^{(i)} = 104 \text{ cP}$ (fitted as described in section 3.2.2), $\epsilon = 0.0024$.

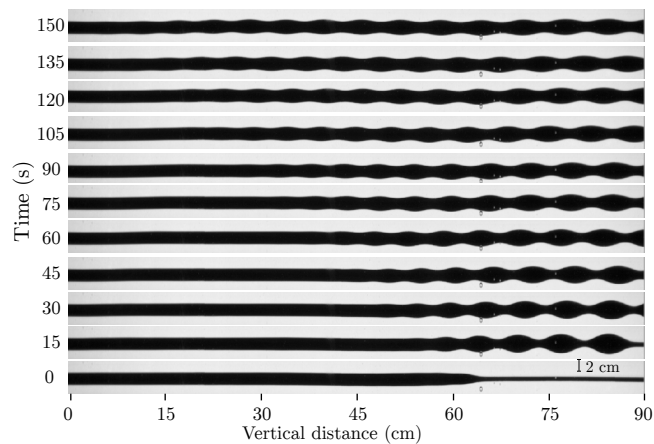


Figure 3.13: Time-lapse images (aspect ratio 1:1) of large amplitude wave breaking leading to upstream propagation of the DSW trailing edge envelope: DSW backflow. Nominal experimental parameters: $\Delta\rho = 0.0983 \text{ g/cm}^3$, $\mu^{(i)} = 93.5 \text{ cP}$, $\epsilon = 0.029$, $a_- = 4$, and $Q_0 = 0.50 \text{ mL/min}$.

that have been inaccessible in other superfluid-like media. We show here the fidelity of this experiment to predictions for conduit equation dispersive shock waves and accessibility for more exotic initial conditions.

Chapter 4

Solitary Wave Fission of a Large Disturbance in a Viscous Fluid Conduit

Solitary wave fission or soliton fission covers a wide range of problems with a multitude of applications. For example, while intense earthquakes can lead to the vertical displacement of the ocean surface by several meters, its horizontal extent can reach 10–100 kilometers [29], which, under appropriate shallowness conditions, can evolve into a large number of surface solitary waves [58, 6]. Another important example is the generation of large amplitude internal ocean solitary waves with two identified soliton fission mechanisms: 1) an initial, broad displacement of internal temperature and salinity [63] and 2) the propagation of a large internal solitary wave onto a shelf [27, 78]. In both scenarios, the result is the same—the generation of a large number of rank-ordered solitary waves. In fact, the well-known soliton fission law by [16] for scenario 2 was obtained by modeling it with an initial, broad disturbance to the constant coefficient Korteweg-de Vries (KdV) equation. More generally, the disintegration of a broad disturbance into solitary waves is the inevitable result of boundary or topography interaction with an undular bore or dispersive shock wave (DSW) that results from a sharp gradient [22].

Because of its ubiquity, we seek a deeper understanding of soliton fission that results from a broad initial condition. Because the method used to describe solitary wave fission in [24] is not reliant on integrability of the underlying PDE and yields concrete predictions for the number of solitary waves and their amplitude distribution that resolve from broad initial disturbances, we refer to it as the “solitary wave resolution method.”

We will first study the solitary wave fission problem experimentally. The work presented

here is part of a manuscript in preparation. Previous laboratory observations were primarily in water waves in the weakly nonlinear, long-wave KdV regime [35, 36, 76]. More recent water wave experiments were performed in a wave tank and physically recreated the Zabusky-Kruskal numerical experiment, observing recurrence as well as soliton fission [76]. These experiments exhibit excellent agreement with WKB theory applied to the inverse scattering transform, which in turn aligned with the original numerical experiment [14]. The IST-WKB approach has also been applied to NLS, resulting in the number and amplitudes of emergent solitons [15]. However, none of these methods are applicable to non-integrable equations.

This chapter presents soliton fission experiments and theory for the conduit equation (1.3)

$$a_t + (a^2)_z - (a^2 (a^{-1} a_t)_z)_z = 0.$$

Equation (1.3) fails the so-called Painlevé test for integrability [38] and has a finite number (two) conservation laws [37], therefore it is an excellent candidate to test the more broadly applicable solitary wave resolution method on the initial value problem consisting of (1.3) and

$$a(z, 0) = 1 + a_0(z), \quad \lim_{|z| \rightarrow \infty} a_0(z) = 0, \quad (4.1)$$

where $a_0(z)$ is a broad, localized disturbance with exactly one critical point at the maximum

$$a_m = \max_{z \in \mathbb{R}} a_0(z). \quad (4.2)$$

Note that $a = a_m + 1$ at the maximum, i.e., a_m measures the amplitude of the disturbance exceeding the unit background area ratio $a = 1$. We will quantify the profile's broadness more precisely later on but for $a_0(z)$ in the shape of a box, then a sufficiently wide box will do. Formally, $a_0 \in \mathcal{C}^\infty(\mathbb{R})$ (infinitely continuously differentiable functions of a real variable) as well, but the relaxation of this assumption still aligns with the theoretical results. We shall assume that the support of $a_0(z)$ is $[-w, 0]$ where $w > 0$ is the box width. The method utilizes the characteristics of the Whitham modulation equations to estimate the number of solitary waves and the solitary wave amplitude distribution resulting from a large-scale initial condition. An example initial condition and its numerically evolved state according to the conduit equation (1.3) are shown in figure 4.1. The

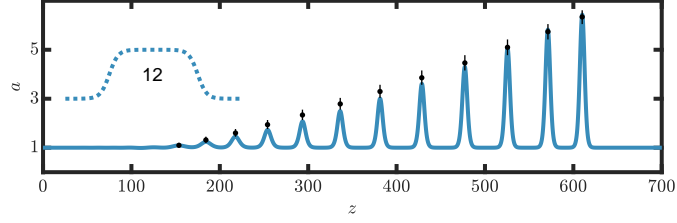


Figure 4.1: A box initial condition (inset) and its long-time numerical evolution according to the conduit equation (1.3). The number denotes the predicted number of solitary waves from that initial condition, and the black circles with vertical bars denote the ranges from a quantiled distribution of the predicted solitary wave amplitudes, both derived later in this chapter.

theoretically predicted solitary wave number (12) is correct and the predicted amplitudes fall well within the ranges determined from the quantization of the continuous amplitude distribution. These predictions will be derived in section 4.2.

As shown in section 1.2.2, the conduit equation (1.3) can be approximated by the KdV equation (1.2) in the small-amplitude, long-wavelength regime by the transformation [83] (cf. (1.47))

$$t = \delta^{3/2}t, \quad x = \delta^{1/2}2^{-1/3}(z - 2t), \quad v = 2^{2/3}\delta(a - 1), \quad (4.3)$$

where the small parameter $\delta > 0$ is the wave amplitude above a background of 1. Thus the KdV results for soliton fission in equation (1.27) can be applied to the conduit equation when rescaled according to equation (4.3), provided δ is small. We seek an approximate solution outside of this relatively narrow regime through the application of the solitary wave resolution method to the conduit equation, with results for the number of solitary waves and amplitude distribution for initial conditions of the class outlined above.

4.1 Observation of Solitary Wave Fission

We motivate our analysis by first presenting viscous fluid conduit experiments on solitary wave fission.

$\mu^{(i)}$	36.6 cP
$\mu^{(e)}$	1296 cP
$\rho^{(i)}$	$1.198 \pm 0.001, \text{ g cm}^{-3}$
$\rho^{(e)}$	$1.260 \pm 0.001, \text{ g cm}^{-3}$
ε	0.0283
Q_0	0.5 mm min^{-1}

Table 4.1: Densities, viscosities, viscosity ratio, and background flow rate from the experiments reported in chapter 4.

4.1.1 Experimental Setup

The experimental setup is the same as that in section 1.4, and the fluids consist of a glycerine base. One camera fitted with a macro lens is used to capture the initial box profile and another is near the top of the apparatus (the far-field) to capture the long-time dynamics. The parameter values used in the experiments presented here are those in table 4.1. The area of the full conduit over time was captured by a camera with a zoom lens, and a representative trial is shown in the contour plot figure 4.2.

4.1.2 Methods

We use the characteristic method described in [5] and section 3.1 to generate a volumetric flow rate profile resulting in a box-like structure in the lower part of the column with a specified width w and nondimensional cross-sectional area $a_m + 1$. The lower camera takes several images before, during, and after the predicted box development time. After the box forms, the pump rate is reduced to the background rate Q_0 , and the box evolves into oscillations, rising up the conduit. Once the leading oscillation reaches the upper camera imaging window, images are taken at 0.2 Hz for several minutes, to ensure all waves that originated from the box have had time to propagate through the viewing window. Images are processed via the method detailed in section 1.4.2.

We use the lower camera to determine the box shape. Note that near the point of breaking, dispersion is no longer negligible; as a result, a pure box is difficult to realize in the conduit system [5]. We use the method defined in [5] and section 3.1.2 to extract the time of box profile formation,

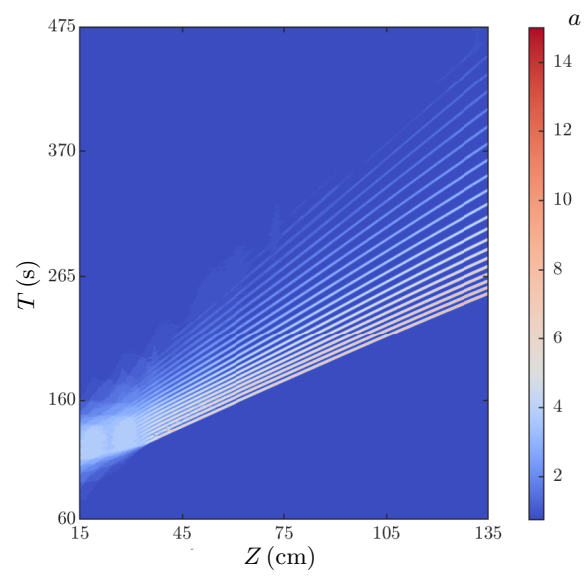


Figure 4.2: Experimental development and dispersion of a box over the full experiment.

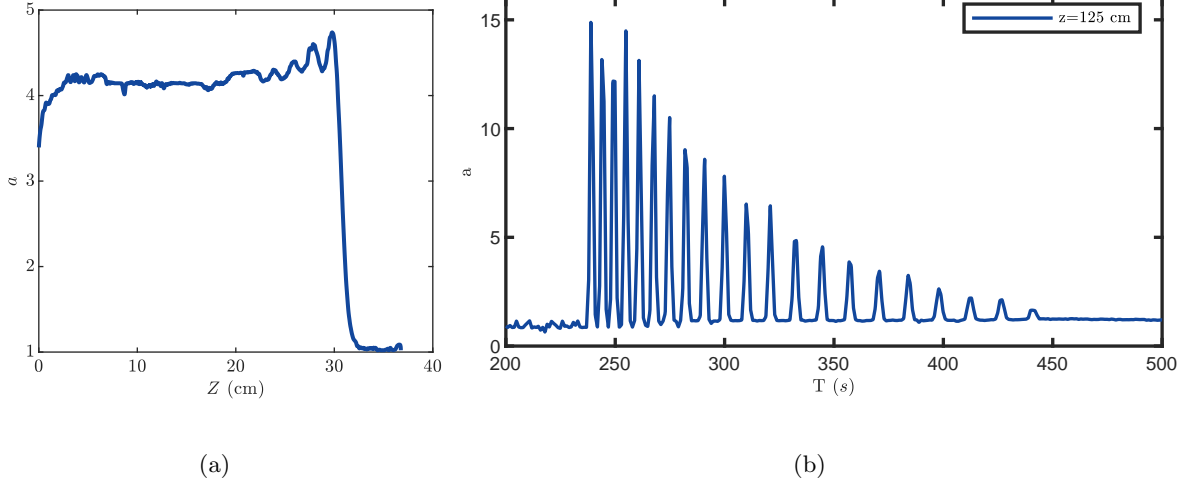


Figure 4.3: (a) Example of an experimental box. Note wavebreaking (DSW formation) has already initiated at the leading edge. (b) Conduit area over time at a fixed distance in the upper part of the apparatus.

and use the nondimensionalized version of that profile as the initial condition in further analyses of the conduit equation. An example, approximate box profile is shown in figure 4.3(a).

For the upper camera, a wave-tracking algorithm was implemented to follow all wave peaks across the imaging window. An experimental time-trace of a solitary wave train is shown in figure 4.3(b). Each candidate peak's amplitude and position are validated against the conduit equation's (1.3) solitary wave amplitude-speed relation (1.55) during the temporal window that the peak is in view. The elevation solitary wave amplitude $\mathcal{A}_s > 1$ is measured from zero area, hence must be larger than the background area $a = 1$. Since solitary waves in the conduit equation exhibit the speed lower bound $c(\mathcal{A}_s) > 2$, any wave peak with a speed lower than that was discarded as small amplitude, dispersive wave phenomena.

4.1.3 Results

A total of 30 experimental trials were executed according to the experimental protocol described in section 3.1.2. We generated the box widths $\{20, 25, 30, 35, 40\}$ cm, corresponding to nondimensional widths $w \in \{90, 112, 134, 156, 178\}$, and box heights $a_m \in \{1, 2, 3\}$. The results are

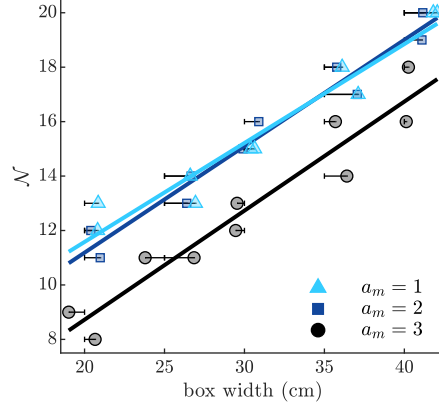


Figure 4.4: Observed number of solitary waves \mathcal{N} from experimental boxes of differing dimensional widths and nondimensional heights a_m . Least-square linear fits for each dataset are included.

shown in figures 4.4 and 4.5. Figure 4.4 depicts the observed number of solitary waves as a function of box width and amplitude. For fixed amplitude, the data exhibit an approximately linear increase with width. Figure 4.5 reports the normalized cumulative distribution functions (cdfs) $\mathcal{F}_{a_m}(\mathcal{A}; w)$ for solitary wave amplitudes resulting from a box of fixed amplitude a_m and variable width w . In particular, $F_{a_m}(\mathcal{A}; w)$ is the number of observed solitary waves with amplitude less than or equal to \mathcal{A} and $\mathcal{F}_{a_m}(\mathcal{A}) = F_{a_m}(\mathcal{A}; w)/\mathcal{N}_{a_m}(w)$, where $\mathcal{N}_{a_m}(w)$ is the total number of observed solitary waves from a box of amplitude a_m and width w . The coincidence of the normalized cdfs is remarkable and will be explained with theory.

4.2 Conduit Equation Solitary Wave Fission

Initially, the edges of the initial value problem (4.1) can be treated as two Riemann problems. In short time, the leading edge will evolve similar to a DSW, and the trailing edge similar to a rarefaction wave (RW). However, the evolution in both directions results in interactions with the other structure due to the finite size of the box. Then neither DSW or RW expands indefinitely, and the difference in this analysis as opposed to that done for DSWs is that the box is of finite width and thus will have a finite number of oscillations.

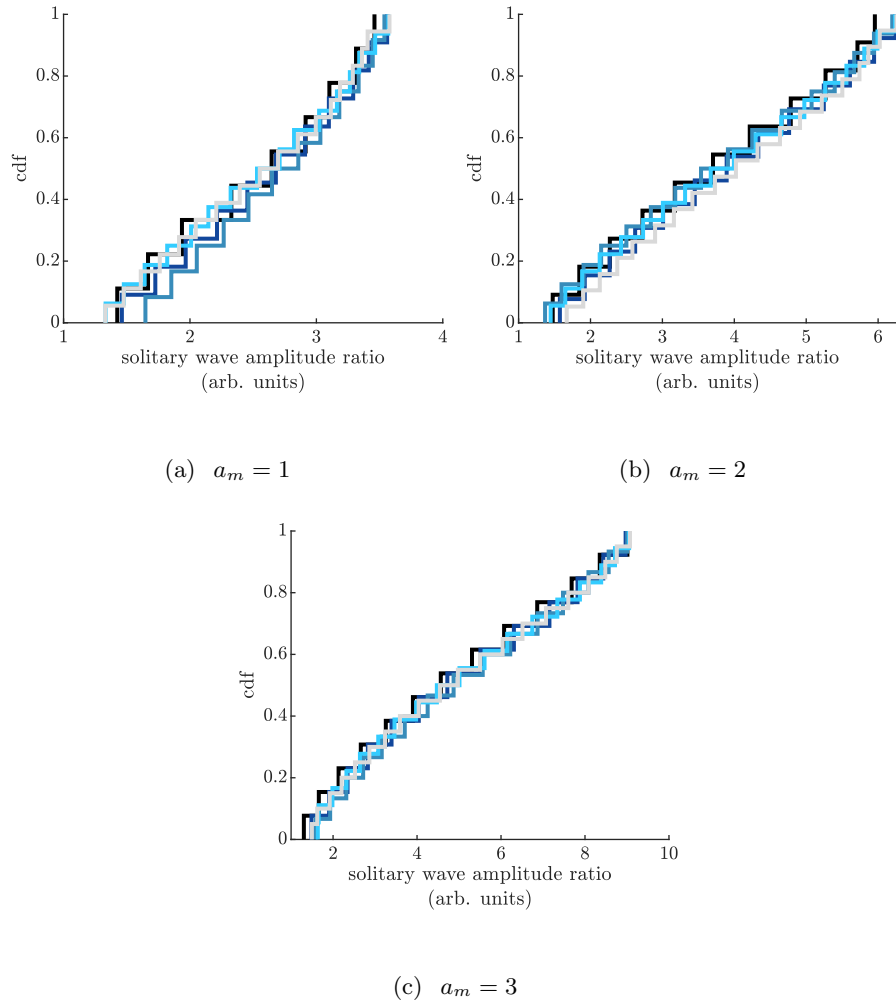


Figure 4.5: Experimental cdfs for solitary wave amplitudes $\mathcal{F}_{a_m}(\mathcal{A}; w)$, for different boxes. Each plot corresponds to a different input a_m and darker lines correspond to narrower boxes.

4.2.1 Number of Solitary Waves

We assume the initial value problem (4.1) will result in a slowly modulated wavetrain [24]. Given enough time, the individual wave crests will separate with minimal overlap, i.e., will result in a non-interacting solitary wavetrain. To count these waves, note that they are separated by exactly their wavelength, defined in terms of the wavenumber as $2\pi/k$. Thus $k/2\pi$ is a wave density and the total number of waves in a wavetrain at time t can be computed according to

$$\mathcal{N}(t) = \frac{1}{2\pi} \int_{-\infty}^{\infty} k(z, t) dz, \quad (4.4)$$

if we treat k as a slowly varying modulation variable. This integral is finite for $t = 0$, as the localized nature of the disturbance means $k \rightarrow 0$ as $|z| \rightarrow \infty$. Within the context of modulation theory, \mathcal{N} is conserved in time. Then the total number of waves are determined by simply the wavenumber function associated with the initial condition.

Whitham modulation theory can now be utilized to find a relationship between the initial condition—interpreted here as the initial wave mean $\bar{\phi}$ and the wavenumber k . The Whitham equations (1.58) are supplemented with conditions that ensure continuity of the modulation solution at the leading and trailing edges of the wavetrain for all t . Denoting these edges $z_+(t)$ and $z_-(t)$, respectively,

$$\begin{aligned} z = z_-(t) : \quad \mathcal{A} &= 0, \quad \bar{\phi} = \beta_-(t), \\ z = z_+(t) : \quad k &= 0, \quad \bar{\phi} = \beta_+(t) = 1, \end{aligned} \quad (4.5)$$

Here, $\beta_{\pm}(t) = \beta(z_{\pm}(t), t)$, where $\beta(z, t)$ is a solution of the Hopf equation

$$\beta_t + 2\beta\beta_z = 0, \beta(z, 0) = 1 + a_0(z). \quad (4.6)$$

This is the dispersionless conduit equation, which has been shown to approximate the system behavior when there are no oscillations [5]. Therefore, this equation is assumed to be valid outside the region influenced by the disturbance, i.e. $(-\infty, z_-(t)) \cup (z_+(t), \infty)$.

Note that there exist only two ways for the modulation solution to continuously match the dispersionless limiting equation for β : $k \rightarrow 0$ or $\mathcal{A} \rightarrow 0$. The choice $k \rightarrow 0$ in the solitary wave

limit and $\mathcal{A} \rightarrow 0$ is the small amplitude, harmonic wave limit. These limits both manifest in the modulation solution for a DSW, with $k \rightarrow 0$ at the rightmost edge and $\mathcal{A} \rightarrow 0$ at the leftmost edge [52]. Because the early time evolution leads to the generation of a DSW, $k \rightarrow 0$ at $z = z_+(t)$ and $\mathcal{A} \rightarrow 0$ at $z = z_-(t)$. When $\mathcal{A} \rightarrow 0$, the modulation system then reduces to (see section 1.1.4):

$$\mathcal{A} = 0: \quad \bar{\phi}_t + 2\bar{\phi}\bar{\phi}_z = 0, \quad k_t + (\omega_0(\bar{\phi}, k))_z = 0. \quad (4.7)$$

Since the disturbance is initially non-oscillatory, we have $\bar{\phi}(z, 0) = 1 + a_0(z)$, $z \in \mathbb{R}$. However, because there are no initial oscillations, $\mathcal{A}(z, 0) = 0$, $z \in \mathbb{R}$, the initial wavenumber is not well-defined. We must appeal to properties of the disturbance's evolution in order to uniquely define $k(z, 0)$. We do so by identifying a simple wave relationship $k = k_-(\bar{\phi})$ between the wavenumber and mean so that $k(z, 0) = k_-(\bar{\phi}(z, 0))$. The rationale for the use of the simple wave relation is detailed in [22] and is based on the fact that the DSW trailing edge is a characteristic. Equation (4.7) has two families of characteristics,

$$\frac{dz}{dt} = 2\bar{\phi}, \quad \frac{dz}{dt} = \omega_{0,k}. \quad (4.8)$$

The first family corresponds to evolution of the mean flow equation (4.6) and coincides with the slowly varying evolution of the disturbance, e.g. the initial RW, while the second family characterizes the small amplitude oscillations that emerge from the disturbance with an envelope that moves with the group velocity. It is the second characteristic family that captures the evolution of the emergent solitary wavetrain. In order to obtain the relationship between k and $\bar{\phi}$ along the second characteristic family, we make the simple wave assumption $k = k_-(\bar{\phi})$ along $z_-(t)$ where $dz/dt = \omega_{0,k}$, which combined with the modulation equations (4.7) results in the ODE (recall the differential form in section 1.1.4)

$$\frac{dk_-}{d\bar{\phi}} = \left[\frac{\omega_{0,\bar{\phi}}}{2\bar{\phi} - \omega_{0,k}} \right]_{k=k_-}. \quad (4.9)$$

Substituting the linear dispersion relation (1.52) into this equation and integrating yields an expression for k_- in terms of the wave mean $\bar{\phi}$ and an integration constant, λ

$$k_-(\bar{\phi}; \lambda)^2 = \frac{1}{2} \left(\lambda - \frac{2}{\bar{\phi}} + \sqrt{\frac{\lambda}{\bar{\phi}}(4 + \bar{\phi}\lambda)} \right). \quad (4.10)$$

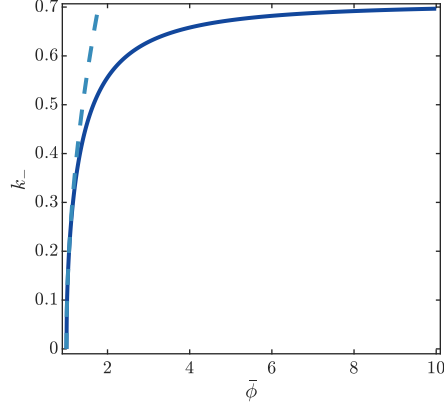


Figure 4.6: Wavenumber k_- versus the wave mean $\bar{\phi}$, with fixed integration constant $\lambda = 1/2$. The solid line shows k_- from the conduit equation, and the dashed line is the result from the KdV equation (1.26), rescaled for the conduit equation via (4.3). This monotonic relationship determines the mean-to-wavenumber mapping of the initial box disturbance.

Matching to equation (4.6) at the disturbance's initial termini $z \in \{0, w\}$, $k_-(\bar{\phi} = 1; \lambda) = 0$, thus $\lambda = 1/2$. This choice of integration parameter results in the same expression for k_- as found at the DSW's harmonic edge from DSW fitting theory; see equation (1.60). Figure 4.6 shows the change in k_- based on varying $\bar{\phi}$. The number of solitary waves are asymptotically determined by this relationship and equation (4.4)

$$\begin{aligned} \mathcal{N} &= \frac{1}{2\pi} \int_{-\infty}^{\infty} k(z, 0) dz \\ &= \frac{1}{2\pi} \int_{-\infty}^{\infty} k_- \left(1 + a_0(z); \frac{1}{2} \right) dz. \end{aligned} \quad (4.11)$$

For the case of a box of height a_m and width w above a background of 1, this can be integrated exactly

$$\begin{aligned} a_0(z) &= \begin{cases} a_m, & -w < z < 0, \\ 0, & \text{else} \end{cases}, \\ \mathcal{N} &= \frac{w}{4\pi} \sqrt{\frac{a_m - 3}{1 + a_m}} + \sqrt{\frac{9 + a_m}{1 + a_m}}. \end{aligned} \quad (4.12)$$

We can now precisely state the asymptotic requirement for the applicability of the solitary wave resolution method: $\mathcal{N} \gg 1$, guaranteeing a large number of solitary waves. The small a_m approxi-

mation depends on both w and a_m

$$\mathcal{N} \sim \frac{w}{\pi} \sqrt{\frac{a_m}{6}} - \frac{5w}{9\pi} \sqrt{\frac{a_m^3}{6}} + \mathcal{O}\left(w a_m^{5/2}\right) \quad (4.13)$$

whose leading order behavior agrees with the result for KdV in equation (1.27). The large a_m approximation, on the other hand, only weakly depends on a_m

$$\mathcal{N} \sim \frac{w}{4\pi} \left(\sqrt{2} - \frac{2\sqrt{2}}{a_m^2} \right) + \mathcal{O}\left(\frac{w}{a_m^3}\right) \quad (4.14)$$

Otherwise, equation (4.11) can be integrated numerically for generic disturbances $a_0(z)$.

4.2.2 Distribution of Solitary Wave Amplitudes

Next, we seek an estimate for the amplitudes of the generated solitary waves. We can assume after sufficiently long time the overlap between waves is exponentially small, and thus each wave crest can be treated as a solitary wave. Because the conduit solitary wave speed (1.55) is monotonically increasing with amplitude, the solitary waves are rank-ordered. We find a relationship between the initial condition $1 + a_0(z)$ and the solitary wave amplitude distribution via analysis of the level curve $k_-(\bar{\phi}; \lambda) = 0$ because $k \rightarrow 0$ is the solitary wave limit. Solving equation (4.10) for $k_- = 0$ yields $\lambda = 1/(2\bar{\phi})$, a monotone decreasing function of $\bar{\phi}$, as shown in figure 4.7. For an initial profile described by equation (4.1) and $a_m = \max_z a_0(z) \geq 0$, if we let $\bar{\phi}$ vary with a_0 , then λ has range $[1/(2(1 + a_m)), 1/2]$.

We can now extend the calculation of the total number of solitary waves \mathcal{N} to the number of solitary waves $G(\bar{\phi}_{\min})$ that emerge from the section of the initial profile of amplitude of at least $\bar{\phi}_{\min}$. We truncate the initial condition to that profile section and integrate k_- over z with $\lambda = 1/(2\bar{\phi}_{\min})$ obtained from the level curve $k_-(\bar{\phi}_{\min}; \lambda) = 0$. Then

$$G(\bar{\phi}_{\min}) = \frac{1}{2\pi} \int_{z_1(\bar{\phi}_{\min})}^{z_2(\bar{\phi}_{\min})} k_- \left(1 + a_0(z); \frac{1}{2\bar{\phi}_{\min}} \right) dz, \text{ for } \bar{\phi}_{\min} \in [1, 1 + a_m], \quad (4.15)$$

$$z_1(\bar{\phi}_{\min}) \leq z_2(\bar{\phi}_{\min}) \text{ such that } 1 + a_0(z_{1,2}(\bar{\phi}_{\min})) = \bar{\phi}_{\min}.$$

The goal now is to relate $\bar{\phi}_{\min}$ to \mathcal{A} , the solitary wave amplitude. We will use the intermediate variable λ to relate the two. With a slight abuse of notation, we define $z_1(\lambda)$, $z_2(\lambda)$ as the z -values

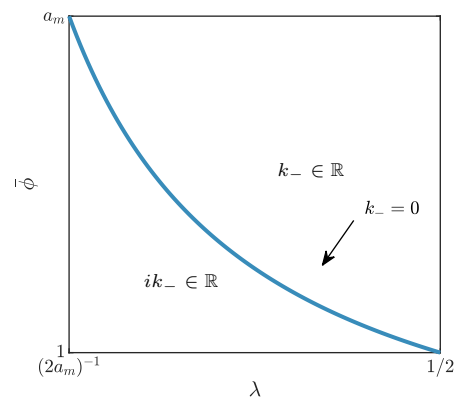


Figure 4.7: Plot of the solitary wave level curve corresponding to $k_- = 0$ in $(\lambda, \bar{\phi})$ -space.

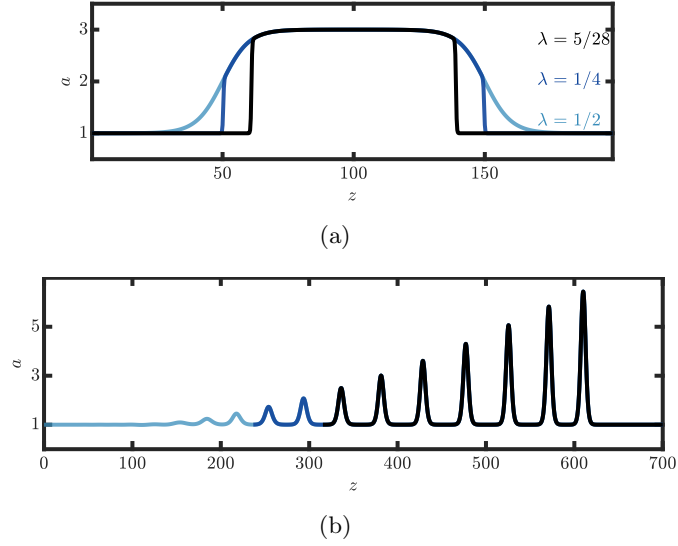


Figure 4.8: (a) Truncation of the initial profile from figure 4.1 for different values of λ . (b) Expected contribution of each λ -truncation in terms of the produced solitary waves.

at which $\bar{\phi} = 1/(2\lambda)$ and $G(\lambda)$ as the total number of solitary waves that emerge from the section of the initial profile of total amplitude at least $1/(2\lambda)$

$$G(\lambda) = \frac{1}{2\pi} \int_{z_1(\lambda)}^{z_2(\lambda)} k_-(1 + a_0(z); \lambda) dz, \quad (4.16)$$

$$z_1(\lambda) \leq z_2(\lambda) \text{ such that } 1 + a_0(z_{1,2}(\lambda)) = 1/(2\lambda).$$

Note $G(\lambda)$ is a decreasing function of λ , and its maximum is \mathcal{N} , so we define the normalized cumulative density function (cdf) $\mathcal{G}(\lambda)$ in λ as

$$\mathcal{G}(\lambda) = 1 - \frac{G(\lambda)}{\mathcal{N}} \in [0, 1], \text{ for } \lambda \in \left[\frac{1}{2(1 + a_m)}, \frac{1}{2} \right]. \quad (4.17)$$

Taking the box and its evolution from figure 4.1 as an example, truncations of the profile for different values of λ are shown in figure 4.8(a) and the expected solitary waves from each truncation are shown color-coded in figure 4.8(b). The integral endpoints z_1 and z_2 for the initial condition of figure 4.1 are shown as a function of λ in figure 4.9.

We now perform an analysis of the solitary wave limit of the Whitham equations that is analogous to the harmonic limit analysis of equation (4.7). We seek a relationship $\mathcal{A} = \mathcal{A}(\bar{\phi})$ valid along the characteristic family associated to the propagation of solitary waves. From DSW fitting

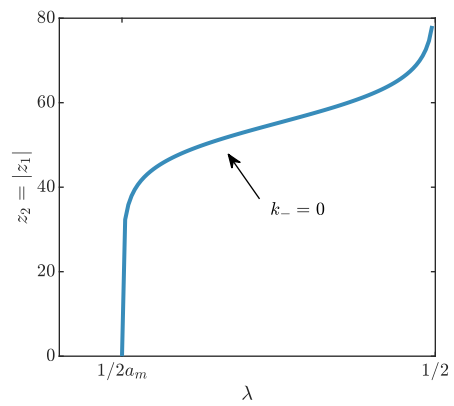


Figure 4.9: Integral endpoints $z_{1,2}$ as a function of the integration constant, λ , for the initial condition of figure 4.1.

theory, we obtain this relationship by a convenient change of variables.

We consider equation (1.58) in the solitary wave limit $k \rightarrow 0$, where the first two equations reduce to (see section 1.1.4)

$$k = 0 : \quad \bar{\phi}_t + 2\bar{\phi}\bar{\phi}_z = 0, \quad \mathcal{A}_t + c(\mathcal{A}, \bar{\phi})\mathcal{A}_z + g(\mathcal{A}, \bar{\phi})\bar{\phi}_z = 0, \quad (4.18)$$

where g is a coupling function that we can bypass determining. A convenient change of variables is to use the conjugate wavenumber,

$$\tilde{k} = \pi \left(\int_{\phi_1}^{\phi_2} \frac{d\phi}{\sqrt{-g(\phi)}} \right)^{-1}, \quad (4.19)$$

where $\phi_{1,2}$ are the two smaller roots of the right side of the periodic wave ODE equation (1.56). The modulation parameter k is then replaced with $\Lambda = k/\tilde{k}$.

This conjugate wavenumber is a construction based on the idea of a conjugate conduit equation, where $\tilde{a}(\tilde{z}, \tilde{t}) = a(i\tilde{z}, i\tilde{t})$ is substituted into equation (1.3)

$$\tilde{a}_{\tilde{t}} + \tilde{a}\tilde{a}_{\tilde{z}} + (\tilde{a}^2 (\tilde{a}^{-1}\tilde{a}_{\tilde{t}})_{\tilde{z}})_{\tilde{z}} = 0. \quad (4.20)$$

The parameter \tilde{k} is the wavenumber of the conjugate traveling wave,

$$\left(\tilde{\phi}_{\tilde{\theta}} \right) = -g(\tilde{\phi}), \quad \tilde{\phi}(\tilde{\theta} + 2\pi) = \tilde{\phi}(\tilde{\theta}) \quad \tilde{\theta} = \tilde{k}\tilde{z} - \tilde{\omega}\tilde{t}, \quad (4.21)$$

with the conjugate linear dispersion relation

$$\tilde{\omega}_0(\tilde{k}) = \frac{2\tilde{k}\bar{\phi}}{1 - \tilde{k}^2\bar{\phi}}. \quad (4.22)$$

We require that periodic solutions $\phi(\theta)$ and $\tilde{\phi}(\tilde{\theta})$ to equations (1.7) and (4.21) have identical phase velocities $c_p = \omega/k = \tilde{\omega}/\tilde{k}$, thus $\omega = \Lambda\tilde{\omega}$. The benefit of this formulation is the solitary wave limit of the conduit equation is the harmonic limit of the conjugate conduit equation, and can be leveraged as such. By substituting $k = \Lambda\tilde{k}$, $\omega = \Lambda\tilde{\omega}$ into the equation for conservation of waves $k_t + \omega_z = 0$, we obtain.

$$\tilde{k}\Lambda_t + \tilde{\omega}\Lambda_z + \Lambda \left(\tilde{k}_t + \tilde{\omega}_z \right) = 0. \quad (4.23)$$

Taking the $k \rightarrow 0$ limit, $\Lambda \rightarrow 0$ and assuming $\Lambda \ll \Lambda_t, \Lambda_x$ for the solutions of interest (see [18]), the equation to leading order is

$$\Lambda_t + \frac{\tilde{\omega}_0}{\tilde{k}} \Lambda_z = 0. \quad (4.24)$$

This equation is satisfied along the characteristic

$$\frac{dz}{dt} = \frac{\tilde{\omega}_0(\bar{\phi}, \tilde{k})}{\tilde{k}} = c_p. \quad (4.25)$$

The specific characteristic where $\Lambda = 0$ corresponds to $k = 0$ and is the solitary wave edge of the DSW. Along $\Lambda = 0$, the characteristic speed c_p is equal to the solitary wave speed given by the speed-amplitude relation (1.55). This relation $c_p = \tilde{\omega}(\tilde{k})/\tilde{k} = c_s(\mathcal{A}, \bar{\phi})$ relates \tilde{k} and \mathcal{A} for well-separated solitary waves

$$\tilde{k}^2 = \frac{1}{\bar{\phi}} - \frac{2}{c_s(\mathcal{A}, \bar{\phi})}. \quad (4.26)$$

The next order equation is the equation for conservation of waves in this limit

$$\tilde{k}_t + (\tilde{\omega}_0)_z = 0, \quad \text{on } \frac{dz}{dt} = \frac{\tilde{\omega}_0(\bar{\phi}, \tilde{k})}{\tilde{k}}. \quad (4.27)$$

Similar to k_- for harmonic waves, the combination of the simple wave assumption ($\tilde{k} = \tilde{k}_+(\bar{\phi})$), $\tilde{\omega}_0(\tilde{k})$, and integration results in the relationship

$$\tilde{k}_+ \left(\bar{\phi}, \tilde{\lambda} \right)^2 = \frac{1}{2} \left(\tilde{\lambda} + \frac{4}{\bar{\phi}} + \sqrt{\frac{\tilde{\lambda}}{\bar{\phi}}(4 + \tilde{\lambda}\bar{\phi})} \right), \quad (4.28)$$

where $\tilde{\lambda}$ is the integration constant. The full system of equations for the wavenumber in the two distinguished limits of the modulated wave can now be written

$$I_1 = \left\{ \mathcal{A} = 0, \quad k_-^2 = \frac{1}{2} \left(\lambda - \frac{2}{\bar{\phi}} + \sqrt{\frac{\lambda}{\bar{\phi}}(4 + \bar{\phi}\lambda)} \right), \quad \text{on } \frac{dz}{dt} = \frac{\omega_0(\bar{\phi}, k)}{k}, \quad (4.29)$$

$$I_2 = \left\{ k = 0, \quad \tilde{k}_+^2 = \frac{1}{2} \left(\tilde{\lambda} + \frac{4}{\bar{\phi}} + \sqrt{\frac{\tilde{\lambda}}{\bar{\phi}}(4 + \tilde{\lambda}\bar{\phi})} \right), \quad \text{on } \frac{dz}{dt} = \frac{\tilde{\omega}_0(\bar{\phi}, \tilde{k})}{\tilde{k}}. \quad (4.30)$$

For compatibility between the short-time prediction of I_1 and the long-time prediction of I_2 , these equations must agree when $k_-(\bar{\phi}; \lambda) = 0 = \tilde{k}_+(\bar{\phi}; \tilde{\lambda})$. By eliminating $\bar{\phi}$, this yields an expression relating the integration constants of $\tilde{\lambda} = -8\lambda$.

In long time, the solitary waves are traveling on unit background, so inserting $\bar{\phi} = 1$, $\tilde{\lambda} = -8\lambda$ into equation (4.28) relates λ to \tilde{k} :

$$-8\lambda(\tilde{k}) = \frac{(\tilde{k}^2 - 1)^2}{\tilde{k}^2 - 2}. \quad (4.31)$$

Equations (4.26) and (4.31) combined describe a relationship between λ and \mathcal{A} , the total solitary wave amplitude

$$\lambda(\mathcal{A}) = \frac{1}{2c_s(\mathcal{A}, 1)^2 + 4c_s(\mathcal{A}, 1)}. \quad (4.32)$$

Note since $\lambda \in [1/2(1 + a_m), 1/2]$, \mathcal{A} is limited to the values $[1, \mathcal{A}_{\max}]$, where \mathcal{A}_{\max} is defined such that $\lambda(\mathcal{A}_{\max}) = 1/2(1 + a_m)$. Then $G(\lambda)$ from equation (4.16) can be written in terms of \mathcal{A}

$$F(\mathcal{A}) = G(\lambda(\mathcal{A})) = \frac{1}{2\pi} \int_{z_1(\lambda(\mathcal{A}))}^{z_2(\lambda(\mathcal{A}))} k_-(1 + a_0(z); \lambda(\mathcal{A})) dz, \quad \mathcal{A} \in [1, \mathcal{A}_{\max}] \quad (4.33)$$

And the normalized cdf of the amplitude distribution is

$$\mathcal{F}(\mathcal{A}) = 1 - \frac{F(\mathcal{A})}{\mathcal{N}}, \quad \mathcal{A} \in [1, \mathcal{A}_{\max}]. \quad (4.34)$$

Since this distribution is continuous, and we have an integer number of solitary waves, we will use the quantiled discretization of this distribution for comparison with experiment and numerics.

We now attempt to explain what is seen in figure 4.10(b), that initial conditions of differing widths but the same height have the same normalized cdf. To do so, we approximate the initial condition as a box of width w and height a_m . Thus the cdf in λ is

$$\mathcal{G}(\lambda) = 1 - \frac{\int_{-w}^0 k_-(1 + a_m, \lambda) dz}{\mathcal{N}}. \quad (4.35)$$

Since there is no variation in z , the numerator can be integrated exactly

$$\mathcal{G}(\lambda) = 1 - \frac{w}{2\pi} \sqrt{\frac{1}{2} \left(\lambda - \frac{2}{1 + a_m} + \sqrt{\frac{\lambda}{1 + a_m} (4 + (1 + a_m)\lambda)} \right)} / \mathcal{N}. \quad (4.36)$$

Then \mathcal{N} from equation (4.12) leads to no w -dependence in the normalized cdf

$$\mathcal{G}(\lambda) = 1 - \sqrt{\frac{2\lambda a_m + 2\lambda - 4 + 2\sqrt{\lambda(1 + a_m)(4 + (1 + a_m)\lambda)}}{a_m - 3 + \sqrt{(9 + a_m)(1 + a_m)}}, \quad \lambda \in [1/(2(1 + a_m)), 1/2]. \quad (4.37)$$

This approximation is valid as long as the edges of the disturbance transition over a small z relative to w .

Then the normalized cdf of the amplitude distribution is

$$\mathcal{F}(\mathcal{A}) = 1 - \sqrt{\frac{2\lambda(\mathcal{A})a_m + 2\lambda(\mathcal{A}) - 4 + 2\sqrt{\lambda(\mathcal{A})(1+a_m)(4+(1+a_m)\lambda(\mathcal{A}))}}{a_m - 3 + \sqrt{(9+a_m)(1+a_m)}}}, \quad \mathcal{A} \in [1, \mathcal{A}_{\max}] \quad (4.38)$$

where $\lambda(\mathcal{A})$ is from equation (4.32).

4.2.3 General Method

The above derivation is readily generalized. Consider the initial value problem for a general dispersive hydrodynamic equation

$$u_t + V(u)u_x = D[u]_x, \quad x \in \mathbb{R}, \quad t > 0, \quad (4.39)$$

$$u(x, 0) = u_0(x), \quad u_0(x) \rightarrow u_\infty,$$

with linear dispersion relation $\omega_0(k, \bar{u})$. Then introduce $k_-(\bar{u}, \lambda)$ as the solution of the ODE

$$\frac{dk_-}{d\bar{u}} = \left[\frac{\omega_{0,\bar{u}}}{V(\bar{u}) - \omega_{0,k}} \right]_{k=k_-}, \quad (4.40)$$

with λ a constant of integration. The number of solitary waves can then be calculated

$$\mathcal{N} = \frac{1}{2\pi} \int_{-\infty}^{\infty} k(u_0(x); \lambda_\infty) dx, \quad (4.41)$$

where λ_∞ is found from $k_-(u_\infty; \lambda_\infty) = 0$. For a box of width w and height u_m ,

$$\mathcal{N} = \frac{w}{2\pi} k(u_m; \lambda_\infty). \quad (4.42)$$

For the solitary wave amplitudes, we have the generic formula in terms of the relationship between the integration constant λ and the cutoff mean \bar{u}

$$\mathcal{F}(\mathcal{A}) = 1 - \frac{1}{2\pi\mathcal{N}} \int_{x_1(\lambda)}^{x_2(\lambda)} k_-(u_0(x); \lambda) dx, \quad (4.43)$$

$$x_1(\lambda) \leq x_2(\lambda) \text{ such that } u_0(x_{1,2}(\lambda)) = \bar{u}(\lambda).$$

Then to obtain $\lambda = \lambda(\mathcal{A})$, one first solves the ODE

$$\frac{d\tilde{k}_+}{d\bar{u}} = \left[\frac{\tilde{\omega}_{0,\bar{u}}}{V(\bar{u}) - \tilde{\omega}_{0,\tilde{k}}} \right]_{\tilde{k}=\tilde{k}_+}, \quad (4.44)$$

where $\tilde{\omega}_0(\tilde{k}, \bar{u}) = -i\tilde{\omega}_0(i\tilde{k}, \bar{u})$. The solution of equation (4.44) is $\tilde{k}_+(\bar{u}, \tilde{\lambda})$, where $\tilde{\lambda}$ is a constant of integration. Setting $k(\bar{u}; \lambda) = \tilde{k}(\bar{u}, \tilde{\lambda}) = 0$ gives the relation between λ and $\tilde{\lambda}$. Substituting $\tilde{k} = \tilde{k}(\bar{u}; \tilde{\lambda}(\lambda))$ into $\tilde{\omega}/\tilde{k} = c_s(\mathcal{A}, \bar{u})$ yields the desired $\lambda = \lambda(\mathcal{A})$.

Two of the main results of this paper do not depend on the system under study. When using equation (4.4) on a pure box initial condition, the result is always linear in the box width. Finally, the normalized cumulative amplitude distribution for a box $\mathcal{F}(\mathcal{A})$ is independent of box width.

4.2.4 Numerical Methods

Direct numerical simulations of the conduit equation were undertaken following the method described in Appendix A.2 [55]. Numerical results presented show how the box evolution changes with width in figure 4.10 and with height in figure 4.11. We observe the number of solitary waves produced changes linearly with the width but does not change very much with box height past a certain height. We observe the normalized cdfs change with box height but not with width.

4.2.5 Comparison to Experiment

Theory predictions for the physical experiments are shown in figures 4.12 and 4.13. The prediction from KdV analysis is also shown in figure 4.13. We calculate \mathcal{N} from a smoothed version of the profile at the time of wavebreaking (see figure 4.3(a)). We observe excellent agreement between experiment and theory, with the observed number of solitary waves being at most two away from the predicted value. We therefore observe a clear decrease in the relative error as the total number of solitary waves increases, as shown in figure 4.12(b). Filled dots and the vertical axis in figure 4.12(a) report the number of observed solitary waves for each trial. The number of emergent solitary waves ranges from 8 to 20, well within the large \mathcal{N} regime where Whitham theory applies [24].

For the normalized cdf $\mathcal{F}(\mathcal{A})$, any non-monotone decrease from the initial profile's maximum results in unphysical predictions, which is unavoidable in experiment. Therefore, instead of using the observed initial condition, we use an idealized version, similar to that used in numerical exper-

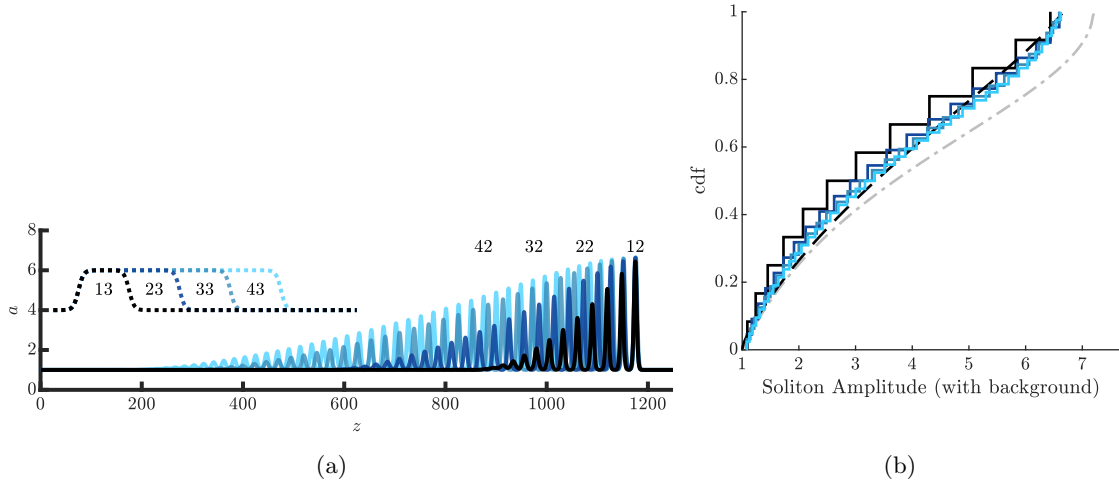


Figure 4.10: (a) Numerical simulations of boxes of different widths $w = 100, 200, 300, 400$ with fixed $a_m = 2$ and the ensuing solitary waves. Note the evolutions here are at different times and shifted to align, to better illustrate the similarities and differences in the amplitude distributions. (b) (solid) Amplitude distributions from the same simulations, (dashed) Predicted amplitude distribution from equation (4.34) for the smoothed box, and (dash-dotted) predicted amplitude distribution from equation (4.38) for a pure box.

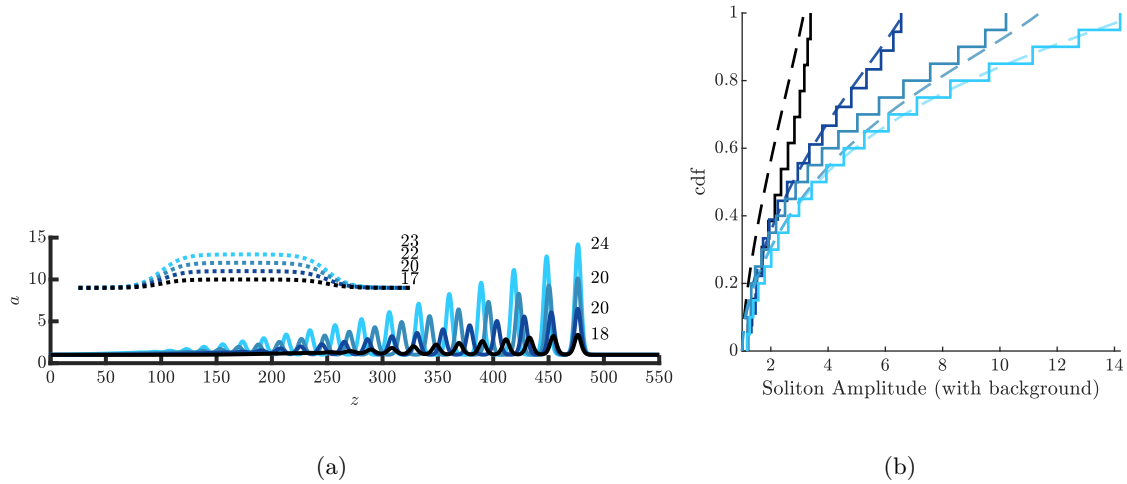


Figure 4.11: (a) Numerical simulations of boxes of different heights $a_m \in 1, 2, 3, 4$ with fixed $w = 150$ and the ensuing solitary waves. The evolutions here are at different times, to better illustrate the similarities and differences in the amplitude distributions. The expected solitary wave counts do not change much past a certain initial condition amplitude, as expected from equation (4.14). (b) (solid) Amplitude distributions from the same simulations, and (dashed) Predicted amplitude distribution from equation (4.34) for the smoothed box.

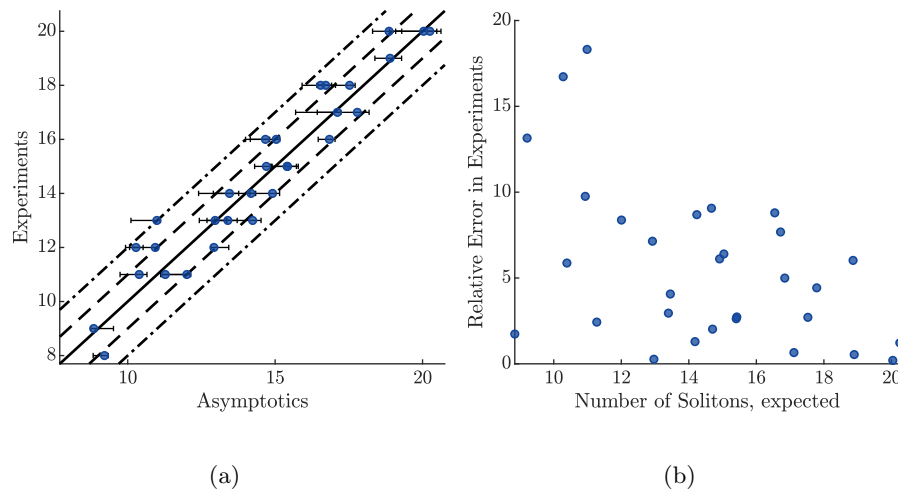


Figure 4.12: (a) Number of solitary waves from experiment (circles) versus the number expected from equation (4.4). The dashed and dot-dashed lines represent one and two solitary waves away from the expected 1:1 relationship. (b) Relative error versus the expected number of solitary waves. Note the relative error goes down dramatically as \mathcal{N} increases.

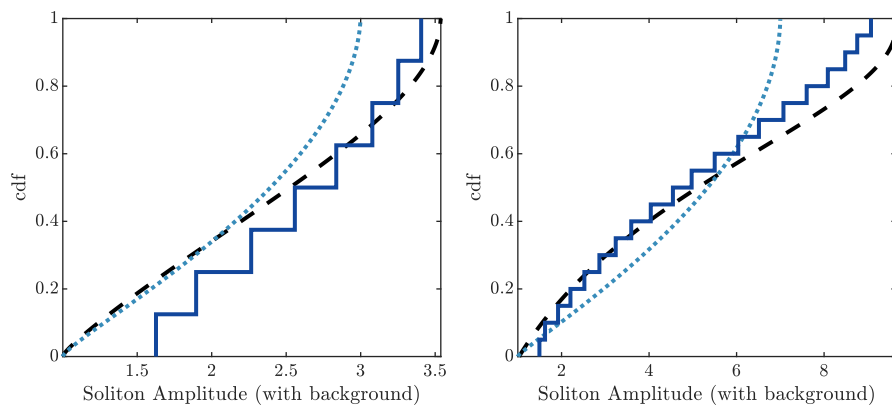


Figure 4.13: Cdfs of amplitude distributions from selected experiments (solid line), with the asymptotic expectation from using the conduit equation (4.34) for the smoothed box (dashed line) and KdV (dotted line). Each step in the experimental cdf corresponds to a solitary wave. Box parameters: (a) width=20 cm, $a_m = 2$ (b) width=40 cm, $a_m = 4$.

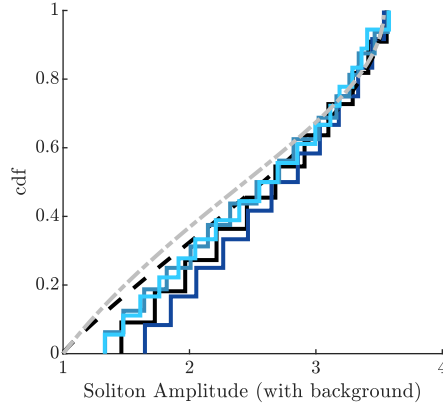


Figure 4.14: Experimental amplitude cdfs (stairs) versus (dashed) Predicted amplitude distribution from equation (4.34) for the smoothed box, and (dash-dotted) predicted amplitude distribution from equation (4.38) for a pure box. Color scale corresponds to initial conditions where $a_m = 2$ and (light to dark) widths 25, 30, 35, 40 cm.

iments (see the inset of figure 4.1). We fit the box amplitude a_m , width w , and steepness of the edges to the experimental profile via least squares.

We also observe a change in conduit diameter of roughly 15% from the bottom of the apparatus to the location of solitary wave data-taking. While this does not affect \mathcal{N} , this is observed to have a profound affect on $\mathcal{F}(\mathcal{A})$. To mitigate this, we use the amplitude prediction from [54] for a solitary wave on a changing background for the conduit equation. We measure error via the ∞ -norm, as this relates to the Kolmogorov-Smirnov test for comparing cdfs. Across all trials, the conduit prediction has roughly half the error as the prediction from rescaled KdV.

We also compare our results to the explicit formula (4.37) in figure 4.14. We observe as the initial condition width increases, we approach the expected distribution.

4.3 Conclusion

Characterizing large disturbances in dispersive hydrodynamic systems, including nonintegrable ones, can be done effectively by treating the disturbance as a slowly modulated wavetrain. By assuming matching conditions at the ends of the disturbance we can get a full picture of the long-time asymptotic evolution of the initial condition into a train of rank-ordered solitary waves.

Predictions from this solitary wave resolution method are the number of solitary waves in the train as well as a model for the distribution of their amplitudes.

We have performed physical experiments to validate this method, which, to the best of our knowledge, have not previously been undertaken in any medium. We find the long-time evolution of the initial profiles is well captured by the solitary wave resolution method, particularly for boxes of large width. All observed solitary wave counts are within 1-2 waves of their expected values, or to within 10% relative error for boxes producing at least 12 waves. Amplitude predictions agree reasonably well and those coming directly from the conduit equation have more predictive power than those rescaled from KdV. These promising results in the model conduit system will hopefully encourage future studies on this category of initial conditions in more complex systems.

Chapter 5

Solitonic Dispersive Hydrodynamics: Theory and Observation

Despite their common origins, solitons and dispersive hydrodynamic structures such as DSWs have been primarily studied independently. Motivated by the ease with which DSWs and solitons can be created in the viscous liquid conduit system, we now investigate novel coherent, nonlinear wave interactions. The focus here is on solitary waves that exhibit solitonic behavior, i.e., elastic or near-elastic interaction, henceforth we refer to them as solitons. This chapter is primarily from [54], with some experimental results reported in [56], as well as some previously unpublished results in section 5.4. Unlike other chapters, here the wave amplitude will be represented by a instead of \mathcal{A} and the field variable for the conduit equation (cross-sectional area) will be $u(x, t)$ instead of $a(z, t)$.

5.1 Observation of Soliton Interactions with Dispersive Hydrodynamic Structures

In figure 5.1, we report solitary wave-DSW and DSW-DSW interactions from our conduit experiment [56]. As in previous experiments [62, 40], an isolated conduit solitary wave is created by the pulsed injection of fluid on top of the steady injection that maintains the background conduit. Figures 5.1(a,b) depict the generation of a DSW followed by a solitary wave. Because solitons propagate with a nonlinear phase velocity larger than the linear wave phase and group velocities [62], the solitary wave eventually overtakes the DSW trailing edge. The solitary wave-DSW interaction results in a sequence of phase shifts between the solitary wave and the crests

of the modulated wavetrain. The solitary wave emerges from the interaction with a significantly increased amplitude and decreased speed due to the smaller downstream conduit upon which it is propagating. The initial and final slopes of solitary wave propagation in figure 5.1(b) demonstrate that the solitary wave has been effectively refracted by the DSW. Meanwhile, the DSW experiences a small—relative to the large, expanding width—phase shift, and is otherwise unchanged.

The opposite problem of a solitary wave being overtaken by a DSW is displayed in figure 5.1(c). After multiple phase shifts during interaction, the solitary wave is slowed down and effectively absorbed within the interior of the DSW, while the DSW is apparently unchanged except for a phase shift in its leading portion. Such behavior is consistent with the interpretation of a DSW as a modulated wavetrain with small amplitude trailing waves that will always move slower than a finite amplitude solitary wave.

Figure 5.1(d) reveals the interaction of two DSWs. The interaction region results in a series of effective phase shifts due to solitary wave-like interactions that form a quasiperiodic or two-phase wavetrain as shown in the inset. This nonlinear mixing eventually subsides, leaving a single DSW representing the merger of the original two. The trailing DSW has effectively been refracted by the leading DSW.

We may consider the overtaking interaction of two DSWs using an extension of DSW theory. Denote the midstream and upstream conduit areas $a_1 < a_2$ relative to the downstream area $a_0 = 1$. Equation (3.14) implies the leading edge speeds of the first and second DSWs are $s_1 = \sqrt{1 + 8a_1} - 1$, $s_2 = a_1(\sqrt{9 + 8(a_2 - 1)/a_1} - 1)$. Motivated by previous DSW interaction studies [2], we assume merger of the two DSWs and thus obtain the leading edge speed of the merged DSW $s_m = 4\sqrt{\frac{1}{2}(a_1 + a_2) - 1} - 1$ connecting conduit areas a_0 to a_2 . One can verify the interleaving property $s_1 < s_m < s_2$, demonstrating the refraction (slowing down) of the second DSW.

While we can assume the solitary wave is a limiting case of a DSW, we found it is more illuminating to use the solitary wave limit of the Whitham equations themselves for a detailed analytical study [54].

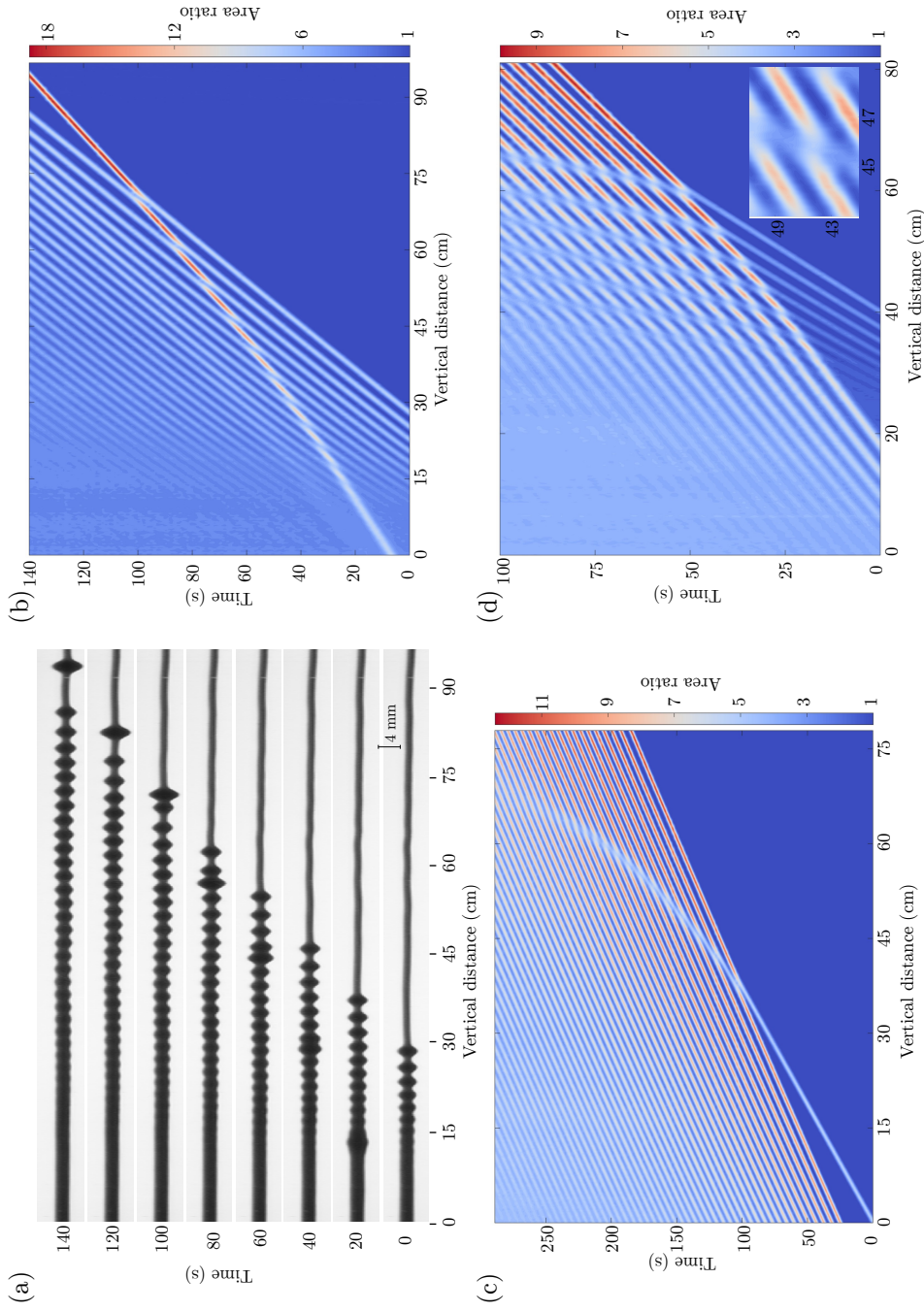


Figure 5.1: Interactions of solitons and DSWs. Time-lapse images with aspect ratio 10:1 (a) and space-time contour (b) of DSW-solitary wave interaction revealing solitary wave refraction by a DSW with $a_- = 3$. (c) Space-time contour of the absorption of a solitary wave by a DSW with $a_- = 3.5$. (d) DSW-DSW interaction and merger causing multiphase mixing (inset) and the refraction of the trailing DSW by the leading DSW with $a_1 = 2.5$, $a_2 = 5$. Nominal experimental parameters: $\Delta\rho = 0.0971 \text{ g/cm}^3$, $\mu^{(i)} = 99.1 \text{ cP}$, $\epsilon = 0.029$, $Q_0 = 0.2 \text{ mL/min}$.

$\mu^{(i)}$	$51 \pm 1 \text{ cP}$
$\mu^{(e)}$	$1200 \pm 200 \text{ cP}$
$\rho^{(i)}$	$1.2286 \pm 0.0001, \text{ g cm}^{-3}$
$\rho^{(e)}$	$1.2587 \pm 0.0001, \text{ g cm}^{-3}$
ε	0.0425
Q_0	0.25 mm min^{-1}

Table 5.1: Densities, viscosities, viscosity ratio, and background flow rate from the experiments reported in chapter 5.

5.1.1 Experiment Setup and Methods

To further focus our interest, experiments are performed using the viscous fluid conduit setup described in 1.4, with glycerine-based fluids with the parameters given in table 5.1. For each trial, a volumetric flow rate profile $Q(t)$ is generated based on these fluid properties that results in a long box followed by a soliton of chosen amplitude (cf. chapter 3). The smaller conduit diameter is set by the background flow rate $Q = 0.25 \text{ mL/min}$. The maximum flow rate for the long box is $Q = 0.7656 \text{ mL/min}$. These two flow rates correspond to a nondimensional jump in cross-sectional area from $u_- = 1$ to $u_+ = 1.75$. The box is sufficiently long that the trailing edge acts as a RW and leading edge acts as a DSW at the time of their respective interactions with the soliton.

Data acquisition of \bar{u}_\pm and a_\pm is performed using three high resolution cameras, two equipped with macro lenses and one with a zoom lens. The macro lens cameras are near the bottom and top of the conduit, and the zoom lens near the middle, for extracting precise conduit diameter and soliton amplitude information. The cameras take several high-resolution images of the soliton as it passes through their respective viewscreens, as well as pictures of the background conduit before and after the hydrodynamic structure has passed.

Calculations suggest that density variations of 1% in the exterior fluid can lead to a 10% change in the background conduit diameter. We observe an increase in the conduit diameter for the top camera, relative to the bottom and middle cameras by 10.1%, which we attribute to density variation of the external glycerine fluid, as opposed to the non-Newtonian, thixotropic effects in the corn syrup used in previous experiments [56]. Because the model assumes no density variation,

we accommodate this discrepancy by scaling all amplitude measurements from the top camera by the factor $1.101^2 = 1.212$.

5.1.2 Results

Observations of the hydrodynamic transmission and trapping of solitons resulting from their interaction with RWs and DSWs are depicted in figure 5.2. The contour plots in 5.2(b,f) show that transmitted solitons exhibit a smaller (larger) amplitude and faster (slower) speed post interaction with a RW (DSW). The transmitted solitons experience a phase shift due to hydrodynamic interaction, defined as the difference between the post and pre interaction spatial intercept. Our measurements show a negative (positive) phase shift for the soliton transmitted through a RW (DSW). Sufficiently small incident solitons in figure 5.2(d,h) do not emerge from the RW or DSW interior during the course of experiment, remaining trapped inside the hydrodynamic state. We now develop a mathematical description of these highly nontrivial nonlinear wave dynamics.

5.2 Solitonic Dispersive Hydrodynamics

Utilizing the scale separation between extended hydrodynamic states and localized solitons (see figure 5.3), we propose a general theory of solitonic dispersive hydrodynamics encapsulated by a set of effective partial differential equations for the hydrodynamic mean field \bar{u} , the soliton's amplitude a , and its phase. We identify two adiabatic invariants of motion and show that they lead to two pivotal predictions. First, the soliton trajectory is a characteristic of the governing equations that is directed by the mean field, a nonlinear analogue of wavepacket trajectories in quantum mechanics [88]. This implies that solitons are either trapped by or transmitted through a hydrodynamic state, depending on the relative amplitudes of the soliton and the hydrodynamic “barrier”.

The second prediction we term hydrodynamic reciprocity. Given an incident soliton amplitude and the far-field mean conditions, the adiabatic invariants are used to predict when the soliton is trapped or transmitted and, in the latter case, what its transmitted amplitude and phase shift

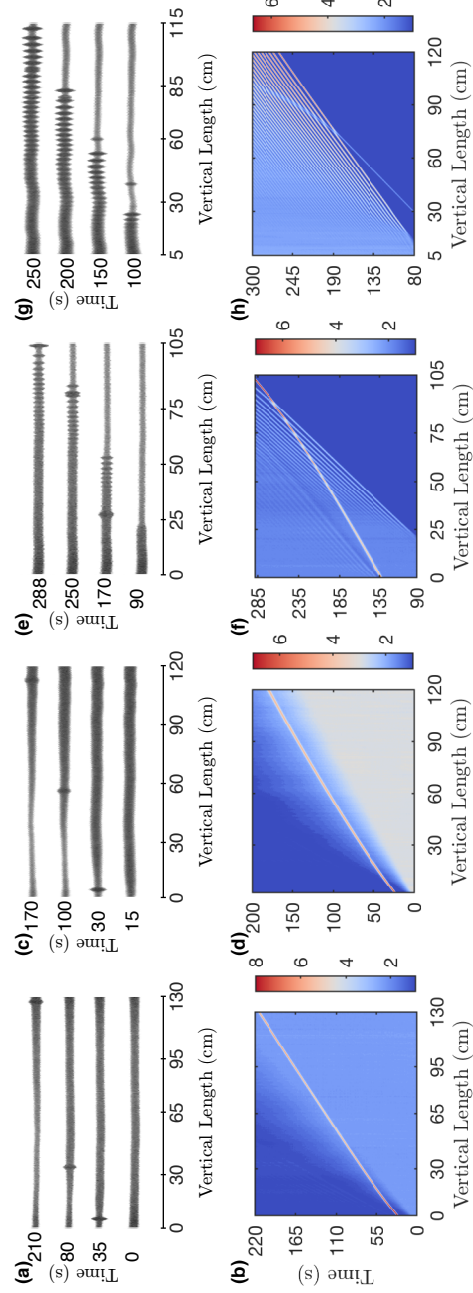


Figure 5.2: Experiments demonstrating soliton transmission and trapping with hydrodynamic states. Representative image sequences (a,c,e,g) and space-time contours (b,d,f,h) extracted from image processing are shown. The colour intensity scale is the dimensionless conduit cross-sectional area relative to the smallest area. a,b) Soliton-RW transmission. c,d) Soliton-RW trapping. e,f) Soliton-DSW transmission. g,h) Soliton-DSW trapping.

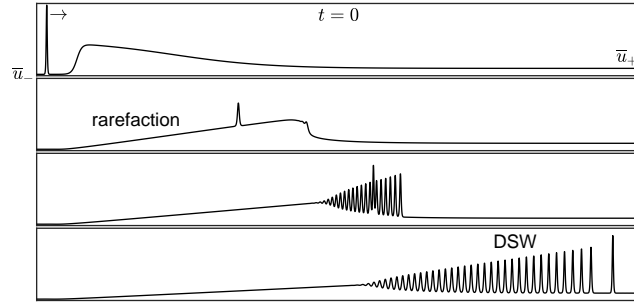


Figure 5.3: Representative initial configuration and evolution (top to bottom) for solitonic dispersive hydrodynamics. The narrow soliton on the uniform mean field \bar{u}_- is transmitted through the broad hydrodynamic flow if it reaches and propagates freely on the uniform mean field \bar{u}_+ . The hydrodynamic flow exhibits expansion (rarefaction) and compression that leads to a dispersive shock wave.

are. Hydrodynamic reciprocity means that the trapping, transmission amplitude/phase relations are the same for soliton interactions with smooth, expanding rarefaction waves (RWs) and compressive, oscillatory DSWs. We stress that the theory presented is general and applies to a wide range of physical media [42, 79, 60, 56, 77, 89, 43].

We begin by considering a general dispersive hydrodynamic medium with nondimensional scalar quantity $u(x, t)$ (e.g., conduit cross-sectional area) governed by

$$u_t + V(u)u_x = D[u]_x, \quad x \in \mathbb{R}, \quad t > 0. \quad (5.1)$$

$V(u)$ is the long-wave speed, $D[u]$ is an integro-differential operator, and equation (5.1) admits a real-valued, linear dispersion relation with frequency $\omega(k, \bar{u})$ where k is the wavenumber and \bar{u} is the background mean field. We assume $V'(u) > 0$ so that the dispersive hydrodynamic system has convex flux [22]. The dispersion is assumed negative ($\omega_{kk} < 0$) for definiteness. We also assume that equation (5.1) satisfies the prerequisites for Whitham theory, an approximate description of modulated nonlinear waves that accurately characterizes dispersive hydrodynamics in a wide-range of physical systems [87, 21].

Many models can be expressed in the form (5.1). We will perform calculations for the Korteweg-de Vries (KdV) equation (1.2), which has $V(u) = u$, $D[u] = -u_{xx}$, a universal model of weakly nonlinear, dispersive waves, and the conduit equation (1.3), which has $V(u) = 2u$,

$D[u] = u^2(u^{-1}u_t)_x$, an accurate model for our experiments [52].

The dynamics of DSWs, RWs, and solitons for equation (5.1) can be described using Whitham theory [87], where a nonlinear periodic wave's mean \bar{u} , amplitude a , and wavenumber k are assumed to vary slowly via modulation equations. The modulation equations admit an asymptotic reduction in the non-interacting soliton wavetrain regime $0 < k \ll 1$ [30, 33]

$$\bar{u}_t + V(\bar{u})\bar{u}_x = 0, \quad (5.2a)$$

$$a_t + c(a, \bar{u})a_x + f(a, \bar{u})\bar{u}_x = 0, \quad (5.2b)$$

$$k_t + [c(a, \bar{u})k]_x = 0. \quad (5.2c)$$

The first equation is for the decoupled mean field, which is governed by the dispersionless, $D \rightarrow 0$, equation (5.1). The second equation describes the soliton amplitude a , which is advected by the mean field according to the soliton amplitude-speed relation $c(a, \bar{u})$ and the coupling function $f(a, \bar{u})$. The final equation expresses wave conservation [87] and describes a train of solitons with spacing $2\pi/k \gg 1$. The soliton train here is a useful, yet fictitious construct because we will only consider the soliton limit $k \rightarrow 0$ of solutions to equation (5.2). Equation (5.2) with $c(a, \bar{u}) = a/3 + \bar{u}$ and $f(a, \bar{u}) = 2a/3$ corresponds to the soliton limit of the KdV-Whitham system of modulation equations, shown in [19] to be equivalent to the soliton modulation equations determined by other means [30] with application to shallow water soliton propagation over topography in [30, 20, 32, 31]. For the conduit equation, we have (5.2) with c_s given in equation (1.55) and some $f(a, \bar{u})$ that can be calculated but we will not need it here. The general case of equation (5.2) was derived in [33] and can be interpreted as a mean field approximation for the interaction of a soliton with the hydrodynamic flow. In contrast to standard soliton perturbation theory where the soliton's parameters evolve temporally [46], solitonic dispersive hydrodynamics require the soliton amplitude $a(x, t)$ be treated as a spatio-temporal field. We note that the equations in (5.2) can be solved sequentially by the method of characteristics [30].

5.2.1 Riemann Invariants

It will be physically revealing to diagonalize the system of equations in (5.2) by identifying its Riemann invariants [87]. First, we notice that equations (5.2a) and (5.2b) are decoupled from (5.2c), and have two distinct, real characteristic velocities $V < c$. This 2×2 subsystem of quasi-linear equations is thus strictly hyperbolic and can be diagonalized for any coupling function $f(a, \bar{u})$ [87].

The mean field equation (5.2a) is already in diagonal form with the Riemann invariant \bar{u} associated with the velocity V . The second Riemann invariant, $q = q(a, \bar{u})$ is associated with the characteristic velocity c . It can be found by integrating $f d\bar{u} + (c - V) da$ (see, e.g., [87]).

The coupling function $f(a, \bar{u})$ is not always readily available, and its direct computation generally requires the determination of a singular, soliton limit in the full system of Whitham modulation equations (5.1) [33]. Below, we use a convenient change of variables proposed in Ref. [18] that enables one to circumvent explicit determination of the coupling function f in the derivation of the Riemann invariant q , utilizing only the known linear dispersion relation $\omega(k, \bar{u})$ and the soliton amplitude-speed relation $c(a, \bar{u})$.

Following Ref. [18], and similar to chapter 4, we introduce a conjugate (soliton) wavenumber $\tilde{k} = \tilde{K}(a, \bar{u})$, implicitly determined via the soliton amplitude-speed relation

$$c(a, \bar{u}) = \tilde{\omega}(\tilde{k}, \bar{u})/\tilde{k}, \quad (5.3)$$

where $\tilde{\omega}(\tilde{k}, \bar{u}) = -i\omega(i\tilde{k}, \bar{u})$ is the conjugate dispersion, whose phase velocity coincides with the speed of a soliton. The conjugate dispersion relation is realized by linearizing the governing dispersive hydrodynamic equation (5.1) with respect to the soliton solution in the far-field. Very often, one can explicitly determine the soliton amplitude-speed relation $c(a, \bar{u})$ hence also the change of variables $\tilde{k} = \tilde{K}(a, \bar{u})$ via equation (5.3).

As a simple example, for the KdV equation we have $\omega = k\bar{u} - k^3$, $c(a, \bar{u}) = \bar{u} + a/3$, therefore $\tilde{k}^2 = a/3$.

For the conduit equation, recall the dispersion and soliton amplitude-speed relations are [56]

$$\begin{aligned}\omega(k, \bar{u}) &= \frac{2\bar{u}k}{1 + \bar{u}k^2}, \\ c_s(a, \bar{u}) &= \frac{\bar{u}}{a^2}(a + \bar{u})^2 (2 \ln(1 + a/\bar{u}) - 1] + \bar{u}^2).\end{aligned}\tag{5.4}$$

The conjugate wavenumber transformation (5.3) then yields $\tilde{k}^2 = 1/\bar{u} - 2/c_s(a, \bar{u})$.

In the variables (\tilde{k}, \bar{u}) , simple wave solutions of equations (5.2a) and (5.2b) satisfy the ordinary differential equation (ODE) [18]

$$\frac{d\tilde{k}}{d\bar{u}} = \frac{\tilde{\omega}_{\bar{u}}}{V(\bar{u}) - \tilde{\omega}_{\tilde{k}}}.\tag{5.5}$$

For the KdV equation, the ODE (5.5) is readily integrated to yield $2\bar{u} + 3\tilde{k}^2 = q$, where q is a constant. For the conduit equation, integration of (5.5) gives an implicit determination of $\tilde{k}(\bar{u})$

$$\frac{\bar{u}(2 - \bar{u}\tilde{k}^2)}{(\bar{u}\tilde{k}^2 - 1)^2} = q,\tag{5.6}$$

where q , again, is a constant of integration.

Generally, $q = q(a, \bar{u})$ is constant along the characteristic $dx/dt = C(q, \bar{u})$, where $C(q(a, \bar{u}), \bar{u}) \equiv c(a, \bar{u})$, and so is a Riemann invariant. For the KdV equation, we find $q = a + 2\bar{u}$ and $C = (q + \bar{u})/3$.

For the conduit equation, we obtain

$$\begin{aligned}q(a, \bar{u}) &= c(a, \bar{u})[c(a, \bar{u}) + 2\bar{u}]/\bar{u}, \\ C(q, \bar{u}) &= -\bar{u} + \sqrt{\bar{u}(q + \bar{u})}.\end{aligned}\tag{5.7}$$

The change of variables $q = q(a, \bar{u})$ diagonalizes (5.2)

$$\bar{u}_t + V(\bar{u})\bar{u}_x = 0,\tag{5.8a}$$

$$q_t + C(q, \bar{u})q_x = 0,\tag{5.8b}$$

For mean flows $\bar{u}(x, t)$ that evolve according to equation (5.2a), the Riemann invariant $q(a, \bar{u})$ is an adiabatic invariant of the dynamics. It is the dispersive hydrodynamic analog of the conserved soliton amplitude in soliton-soliton interactions. Under these conditions, there is a second adiabatic invariant, labeled $r(q, \bar{u}, k)$, also associated with the characteristic velocity $C(q, \bar{u})$. It is readily

found in the form $r = kp(q, \bar{u})$ where $p(q, \bar{u})$ is given by the general expression

$$p(q, \bar{u}) = \exp\left(-\int_{\bar{u}_0}^{\bar{u}} \frac{C_u(q, u)}{V(u) - C(q, u)} du\right), \quad (5.9)$$

where $C(q(a, \bar{u}), \bar{u}) \equiv c(a, \bar{u})$. For KdV, $p(q, \bar{u}) = (q - \bar{u})^{-1/2}$, and for the conduit equation,

$$p(q, \bar{u}) = \frac{\exp\left(\frac{1}{2} \operatorname{arctanh} 3\sqrt{\frac{\bar{u}}{q+\bar{u}}}\right) \sqrt{\frac{\bar{u}}{\sqrt{\bar{u}}+\sqrt{q+\bar{u}}}}}{(8\bar{u} - q)^{1/4}}. \quad (5.10)$$

5.2.2 Initial Value Problem for Diagonalized System

We seek solutions to equation (5.8) subject to an initial mean field profile $\bar{u}(x, 0) = \bar{u}_0(x)$ and an initial soliton of amplitude a_0 located at $x = x_0$. But we require initial soliton and wavenumber fields $a(x, 0)$ and $k(x, 0)$ for all x in order to give a properly posed problem for (5.2). Admissible initial conditions are obtained by recognizing this as a special solution, a simple wave in which q and r are constant [87]. The mean flow therefore satisfies $\bar{u} = \bar{u}_0(x - V(\bar{u})t)$. The initial soliton amplitude and position determine the constant Riemann invariant $q_0 = q(a_0, \bar{u}_0(x_0))$. An initial wavenumber k_0 determines the other constant adiabatic invariant $k_0 p_0 = k_0 p(q_0, \bar{u}_0(x_0))$. As we will show, the value of $k_0 > 0$ is not relevant so can be arbitrarily chosen. We now show how this solution physically describes soliton-mean field interaction.

A smooth, initial mean field, e.g., in figure 5.3, will evolve according to the obtained implicit solution until wavebreaking occurs. Our interest is in the interaction of a soliton with the expansion and compression waves that result. In dispersive hydrodynamics, the simplest examples of these are RWs and DSWs, respectively, which are most conveniently generated from step initial data [34]. We therefore analyze the obtained general solution subject to step initial data

$$\bar{u}(x, 0) = \bar{u}_{\pm}, \quad a(x, 0) = a_{\pm}, \quad k(x, 0) = k_{\pm}, \quad \pm x > 0, \quad (5.11)$$

that model incident and transmitted soliton amplitudes a_- and a_+ through the mean field transition \bar{u}_- to \bar{u}_+ for soliton train wavenumbers k_- and k_+ . The mean field dynamics depend upon the ordering of \bar{u}_- and \bar{u}_+ . When $\bar{u}_- < \bar{u}_+$, the mean field equation admits a RW solution, otherwise

an unphysical, multi-valued solution. Short-wave dispersion regularizes such behavior and leads to the generation of a DSW. We consider each case in turn.

5.2.3 Rarefaction Wave Results

The transmission of a soliton through a RW is shown experimentally in figure 5.2(a,b). The incident soliton “climbs” the RW and emerges from the interaction with altered amplitude and speed. Our aim is to determine the range of parameter values a_{\pm} , \bar{u}_{\pm} for such an interaction to occur and, if so, the amplitude a_+ of the transmitted soliton in terms of the other parameters. If not transmitted, we show that the soliton decays and is trapped by the RW.

The mean field is the self-similar, RW solution with $u(x, t) = \bar{u}_{\pm}$ for $\pm x > \pm V_{\pm} t$ and

$$\bar{u}(x, t) = V^{-1}(x/t), \quad V_- t \leq x \leq V_+ t, \quad (5.12)$$

where $V_{\pm} = V(\bar{u}_{\pm})$ and V^{-1} is the inverse of V . Constants q and kp correspond to adiabatic invariants of the soliton-mean field dynamics that yield constraints on the amplitude, mean field, and wavenumber parameters we call the transmission and phase conditions

$$q(a_-, \bar{u}_-) = q(a_+, \bar{u}_+), \quad \frac{k_-}{k_+} = \frac{p(q_+, \bar{u}_+)}{p(q_-, \bar{u}_-)}. \quad (5.13)$$

The first adiabatic invariant $q(a, \bar{u})$ determines the transmitted soliton amplitude a_+ in terms of the incident soliton amplitude a_- and the mean fields \bar{u}_{\pm} . The second adiabatic invariant determines the ratio k_-/k_+ , which in turn yields the soliton’s phase shift due to hydrodynamic interaction. Equation (5.13) is the main theoretical result of this chapter and describes the trapping or transmission of a soliton through a RW and a DSW.

The necessary and sufficient condition for soliton transmission is a positive transmitted soliton amplitude $a_+ > 0$, which places a restriction on the incident soliton amplitude a_- . For the conduit equation, equation (5.7) implies $c_- > c_{\text{cr}} = -\bar{u}_- + (\bar{u}_-^2 + 8\bar{u}_+\bar{u}_-)^{1/2}$. For KdV, $a_- > a_{\text{cr}} = 2(\bar{u}_+ - \bar{u}_-)$. In both cases, we find that the transmitted soliton’s amplitude is decreased, $a_+ < a_-$ and its speed is increased, $c_+ > c_-$. We now derive the extension of this result to the general dispersive hydrodynamic system equation (5.1), assuming $V'(u) > 0$.

In the mean field, simple wave approximation, the transmission of a soliton through a RW is determined by the conservation of the second Riemann invariant, $q(a, \bar{u})$, of the solitonic hydrodynamic system (5.8). We are interested in the sign of the derivative a_x in the course of soliton transmission. Expressing $a(q, \bar{u})$, we obtain $a_x = a_{\bar{u}} \bar{u}_x$ (since q is constant). Now, using equation (5.12), we have $\bar{u}_x = 1/(tV'(x/t)) > 0$. Next, $a_{\bar{u}} = -q_{\bar{u}}/q_a$. Hence, $\text{sgn } a_x = -\text{sgn}(q_{\bar{u}} q_a)$ and therefore, $\text{sgn}(a_+ - a_-) = -\text{sgn}(q_{\bar{u}} q_a)$ assuming $q_{\bar{u}} \neq 0$, $q_a \neq 0$. Say, for KdV $q = a + 2\bar{u}$ so $\text{sgn}(a_+ - a_-) = -1$ as already observed.

In a similar manner, the acceleration or deceleration of soliton-RW transmission can be determined by the positivity or negativity of C_x . By a similar argument, $\text{sgn}[C_x] = \text{sgn}(C_{\bar{u}})$. For KdV, $C_{\bar{u}} = 1/3$, and for the conduit equation, $C_{\bar{u}} = c^2/[2\bar{u}(c + \bar{u})] > 0$, so a transmitted soliton in both cases is accelerated by the RW. Thus we have shown $\text{sgn}(a_+ - a_-) = -\text{sgn}(q_{\bar{u}} q_a)$ and $\text{sgn}(c_+ - c_-) = \text{sgn}(C_{\bar{u}})$.

The soliton phase shift is $\Delta = x_+ - x_-$ where x_{\pm} are the x -intercepts of the soliton pre (-) and post (+) hydrodynamic interaction. Given the initial soliton position x_- , the contraction/expansion of the soliton train determines the phase shift as $\Delta/x_- = k_-/k_+ - 1 = p_+/p_- - 1$. Hence, the ratio k_-/k_+ in the phase condition (5.13), not the arbitrary initial wavenumber k_- , determines the soliton phase shift. Our use of a fictitious soliton train is therefore justified.

We also determine the soliton-RW trajectory. A soliton with position $x(t)$ propagates through the mean field along a characteristic of the modulation system (5.2)

$$\frac{dx}{dt} = C(q, \bar{u}(x, t)), \quad x(0) = x_-, \quad (5.14)$$

where the soliton amplitude $a(x, t)$ varies along the trajectory according to the adiabatic invariant $q(a(x, t), \bar{u}(x, t)) = q(a_-, \bar{u}_-)$. The phase shift from integration of (5.14) equals Δ from the adiabatic invariant in (5.13), as expected. When $a_+ \leq 0$ in (5.13), the soliton is trapped by the RW, as in experiment, figure 5.2(c,d).

5.2.4 Dispersive Shock Wave Results

If $\bar{u}_- > \bar{u}_+$, a DSW is generated. Soliton-DSW transmission is experimentally depicted in figure 5.2(e,f). An incident soliton propagates through the DSW, exhibiting a highly non-trivial interaction, ultimately emerging with altered amplitude and speed.

In contrast to the soliton-RW problem, the modulation equations (5.2) are no longer valid throughout the soliton-DSW interaction. Instead, the mean field equation is replaced by the DSW modulation equations [34, 21]. We seek a simple wave solution for soliton-DSW modulation. Because DSW generation occurs only for $t > 0$, the soliton-DSW modulation system for $t < 0$ reduces exactly to equation (5.2), i.e., that of soliton-RW modulation. For $t < 0$, the adiabatic invariants (5.13) hold. By continuity of the modulation solution, these conditions must hold for $t \geq 0$ as well. In particular, soliton-RW and soliton-DSW interaction both satisfy the same transmission and phase conditions (5.13). This fact, termed hydrodynamic reciprocity, is due to time reversibility of the governing equation (5.1) and is depicted graphically in figure 5.4.

Equations (5.7) and (5.13) for the conduit equation indicate that solitons incident upon DSWs exhibit a decreased transmitted speed $c_{\text{cr}} < c_+ < c_-$ and an increased transmitted amplitude $a_+ > a_{\text{cr}} > a_-$. The amplitude and speed of the DSW's soliton leading edge are precisely a_{cr} and c_{cr} [50]. Hydrodynamic reciprocity therefore implies that the transmitted soliton's amplitude is decreased (increased), its speed is increased (decreased), and its phase shift is negative (positive) relative to the soliton incident upon the RW (DSW), as observed experimentally in figure 5.2. Using the transmission and phase conditions (5.13), we accurately predict the conduit soliton trajectory post DSW interaction without any detailed knowledge of soliton-DSW interaction.

In contrast to soliton-RW transmission, solitons with amplitude a_+ initially placed to the right of the step will interact with the DSW if $a_+ < a_{\text{cr}}$. Then the transmission condition (5.13) implies $a_- < 0$, i.e., the soliton cannot transmit back through the DSW. Instead, the soliton is effectively trapped as a localized defect in the DSW interior as observed experimentally in figure 5.2(g,h).

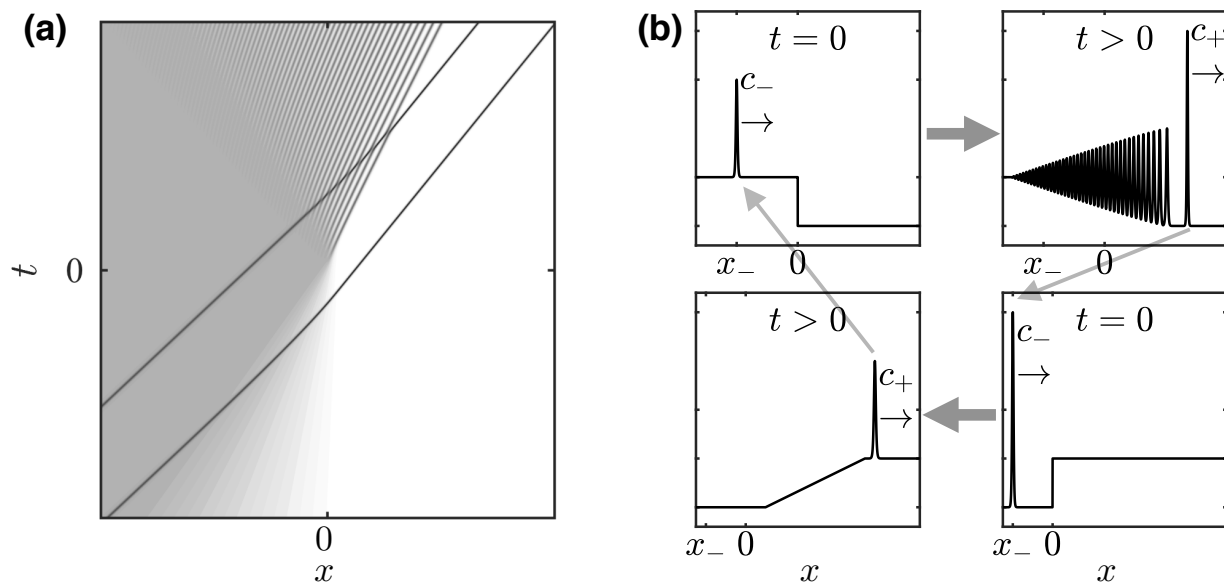


Figure 5.4: Graphical depictions of hydrodynamic reciprocity. (a) Space-time contour plot of soliton-DSW ($t > 0$) and soliton-RW ($t < 0$) interaction with two solitons satisfying the transmission condition (5.13). For $|t|$ sufficiently large, the soliton speeds are the same. (b) If the soliton post DSW interaction (top, left to right) is used to initialize soliton-RW interaction (bottom, right to left), the post RW interaction soliton has the same properties as the pre DSW interaction soliton.

5.3 Comparison to Experiment

The transmission and phase conditions (5.13) for the conduit equation are shown in figure 5.5. For soliton-RW interaction, the abscissa and ordinate are a_- and a_+ , respectively reversed for soliton-DSW interaction. Hydrodynamic reciprocity implies that the transmission condition on these axes is the same for soliton-RW and DSW transmission. Reciprocity is confirmed by experiment and numerical simulations of the conduit equation in figure 5.5(a), that slightly deviate from soliton-mean field theory as the amplitudes increase, consistent with previously observed discrepancies [50, 56]. Reciprocity of the phase shift is also confirmed by conduit equation numerics in figure 5.5(b). Our experiments provide definitive evidence of soliton-hydrodynamic transmission, trapping, reciprocity, and the theory's efficacy.

5.4 Soliton Phase Shift through a General Disturbance

The following work is new and not part of the paper [56]. We have found that the phase condition from equation (5.13) can be used for more generic initial profiles. Recall the soliton phase shift is $\Delta = \phi_+ - \phi_-$, where ϕ_{\pm} are the x -intercepts of the soliton post- and pre- hydrodynamic interaction (x_{\pm} has been changed to ϕ_{\pm} for clarity in later equations). Then the phase shift can be determined for the general equation (5.1) as

$$\Delta = \phi_- \left(\frac{k_-}{k_+} - 1 \right) = \phi_- \left(\frac{p_+}{p_-} - 1 \right), \quad (5.15)$$

where $p_{\pm} = p(q_{\pm}, \bar{u}_{\pm})$, and subsequently the soliton's new x -intercept is

$$\phi_+ = \Delta + \phi_- = \frac{\phi_- p_+}{p_-}. \quad (5.16)$$

Note that this equation assumes the hydrodynamic jump is at $x = 0$ and must be shifted accordingly for jumps at other locations. Recall for KdV, $p = \sqrt{2/a}$, which when combined with the transmission condition (5.13) gives $p_+ = \sqrt{2/(a_- + (\bar{u}_- - \bar{u}_+))}$. For the conduit equation, the expression for p was given in equation (5.10). Then, for a box of height a_m with support $[0, w]$, we can calculate the x -intercept ϕ_{Box} of the soliton post interaction with a box by assuming the back

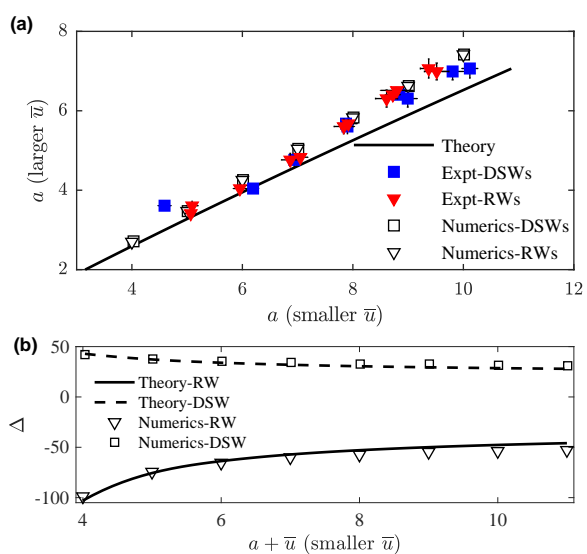


Figure 5.5: Transmitted soliton properties due to conduit soliton-RW and DSW interaction for a hydrodynamic transition from $\bar{u} = 1$ to $\bar{u} = 1.75$. a) Soliton amplitude from eq. (5.13) (curve), experiment (filled squares, triangles), and numerical simulations (open squares, triangles). b) Soliton phase shift from eq. (5.13) (curves) and numerical simulations (symbols).

of the box acts as a RW and the front as a DSW. Letting the mean flow and adiabatic invariants on the background be $(\bar{u}_0, q_0, k_0 p_0)$ and those on top of the box be $(\bar{u}_1, q_1, k_1 p_1)$, and using the soliton's initial x -intercept ϕ_0 , we first directly calculate the soliton phase shift from the step up (RW) to be $\phi_{\text{RW}} = \frac{\phi_0 p_1}{p_0}$, as in equation (5.16). The soliton phase shift from a DSW of the same size centered at 0 would be $\phi_{\text{DSW}} = \frac{\phi_0 p_0}{p_1}$. Then, in order to calculate ϕ_{Box} , we must insert into ϕ_{DSW} the new x -intercept ϕ_{RW} and shift everything by w , the actual location of the step down in the mean flow

$$\begin{aligned}\phi_{\text{Box}} - w &= (\phi_{\text{RW}} - w) \frac{p_0}{p_1} \\ &= \phi_0 - w \frac{p_0}{p_1}.\end{aligned}$$

Therefore

$$\phi_{\text{Box}} = \phi_0 + w \left(1 - \frac{p_0}{p_1}\right).$$

For a KdV soliton with initial total amplitude a_0 , the phase shift is

$$\Delta = \phi_{\text{Box}} - \phi_0 = w \left(1 - \sqrt{\frac{a_0 - 2(\bar{u}_1 - \bar{u}_0)}{a_0}}\right). \quad (5.17)$$

An additional benefit of this method is that it can be generalized. Consider a disturbance $\bar{u}(x)$ with support on $[0, W]$ connecting constant states \bar{u}_0 for $x < 0$ and \bar{u}_W for $x > W$. First, if $\bar{u}(x)$ consists of n boxes of width w and heights \bar{u}_k , $k = 1, \dots, n$, then the new phase ϕ_n for a soliton with initial phase $\phi_0 < 0$ and invariants $(\bar{u}_0, q_0, k_0 p_0)$ can be found in a similar way to the box, by inserting the previous phase shift into equation (5.16) and shifting by the box width w . This results in a recursive relation for ϕ_{k+1} of

$$\phi_{k+1} - kw = (\phi_k - w) \frac{p_{k+1}}{p_k}. \quad (5.18)$$

It can be shown via induction that the solution to this relation is

$$\phi_{k+1} = \phi_0 \frac{p_{k+1}}{p_0} + w \sum_{i=1}^k \left(1 - \frac{p_{k+1}}{p_i}\right). \quad (5.19)$$

Then for a continuous $\bar{u}(x)$, i.e. sending $n \rightarrow \infty$, $w = W/n \rightarrow 0$, we obtain the Riemann integral

$$\phi(x) = \phi_0 \frac{p(x)}{p(\phi_0)} + \int_{\phi_0}^x \left(1 - \frac{p(x)}{p(x')} \right) dx'. \quad (5.20)$$

where $p(x) = p(q(a_0, \bar{u}(x)), \bar{u}(x))$ is the associated with the adiabatic invariant kp evaluated on the initial disturbance $\bar{u}(x)$.

The most general case is when $\bar{u}(x)$ has support $[a, b]$ and the soliton is large enough to travel entirely through it, i.e. the transmission condition is satisfied for all $\bar{u}(x)$, $x \in [a, b]$. If we assume the initial and final mean are $\bar{u}(a)$ and $\bar{u}(b)$, respectively, then there is no contribution to the integral term outside of $x \in (a, b)$. Additionally, $p(x) = p(a)$ for $x \in (-\infty, a)$, and $p(x) = p(b)$ for $x \in (b, \infty)$, so the phase shift is

$$\Delta\phi = \phi_0 \left(\frac{p(b)}{p(a)} - 1 \right) + \int_a^b \left(1 - \frac{p(b)}{p(x)} \right) dx \quad (5.21)$$

For KdV, the phase shift is

$$\Delta\phi = \phi_0 \left(\sqrt{\frac{a_0 - 2(\bar{u}(b) - \bar{u}(a))}{a_0}} - 1 \right) + \int_a^b \left(1 - \sqrt{\frac{a_0 - 2(\bar{u}(x) - \bar{u}(a))}{a_0}} \right) dx. \quad (5.22)$$

We have tested both the KdV box formula (5.17) and the KdV general formula (5.22) numerically; the results are shown in figures 5.6 and 5.7. We find remarkable agreement when compared to other methods, such as approximating the box as a train of solitons with amplitudes from solitary wave fission (for KdV, equation (1.27)) or using IST, neglecting the contribution from radiation as in equation (1.25) to gain a similar result [2]. The total soliton phase shift is then estimated by the sum of all two-soliton phase shifts with the soliton train. The relative error associated with these approximations is shown in figure 5.7. The error in the soliton tunneling general prediction is consistently under 5%, and within 0.1% for all but one trial. The error is maximized for narrow boxes and large solitons. Other methods of prediction exhibit considerably more error and require knowledge of the two-soliton phase shift formula, e.g. equation (1.6) for KdV.

The KdV phase shift equation (5.22) can be readily applied to a wide variety of initial conditions. It has no dependence on whether the initial condition is positive or negative; the only

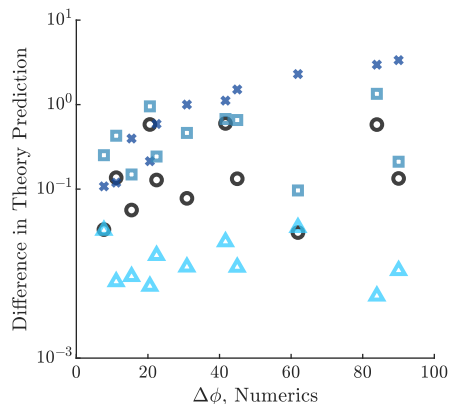


Figure 5.6: Comparison of predicted soliton phase shifts from the soliton fission prediction equation (1.27) (x's), IST box approximation (neglecting radiation) equation (1.25) (squares), equation (5.17) (o's), and (5.22) (triangles) with numerics.

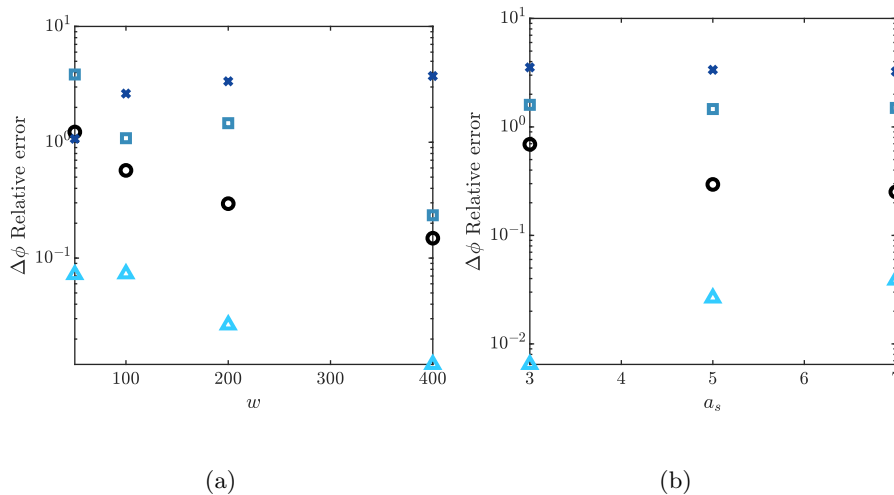


Figure 5.7: Percent relative error associated with predicted soliton phase shifts from the soliton fission prediction equation (1.27) (x's), IST box approximation (neglecting radiation) equation (1.25) (squares), equation (5.17) (o's), and (5.22) (triangles) compared to numerics as a function of (a) box width w , with soliton amplitude $a_s = 5$ and (b) test soliton amplitude a_s , with width $w = 200$.

restriction is $a_0 \geq 2 \max_x \bar{u}(x)$. To test this, we took the initial condition and soliton shown in figure 5.8 and evolved numerically. We observed a numerical phase shift of approximately 17.24, which is within 0.3% of the predicted 17.29 from equation (5.21). For other generic, slowly varying profiles, we observe similar accuracy.

5.5 Conclusion

We have introduced a general framework for soliton-mean field interaction. The dynamics exhibit two adiabatic invariants that describe soliton trapping or transmission. The existence of the same adiabatic invariants for soliton-mean field interactions of compression (DSW) and expansion (RW) imply hydrodynamic reciprocity. This describes a conceptually new notion of hydrodynamic soliton “tunneling” where the potential barrier is the mean field, obeying the same equations as the soliton [74]. We have found through extensive study of these formulae that they apply to a wide range of initial disturbances, far beyond the case considered of an initial step. This theory presents an appealing methodology to control soliton propagation by manipulation of the mean field.

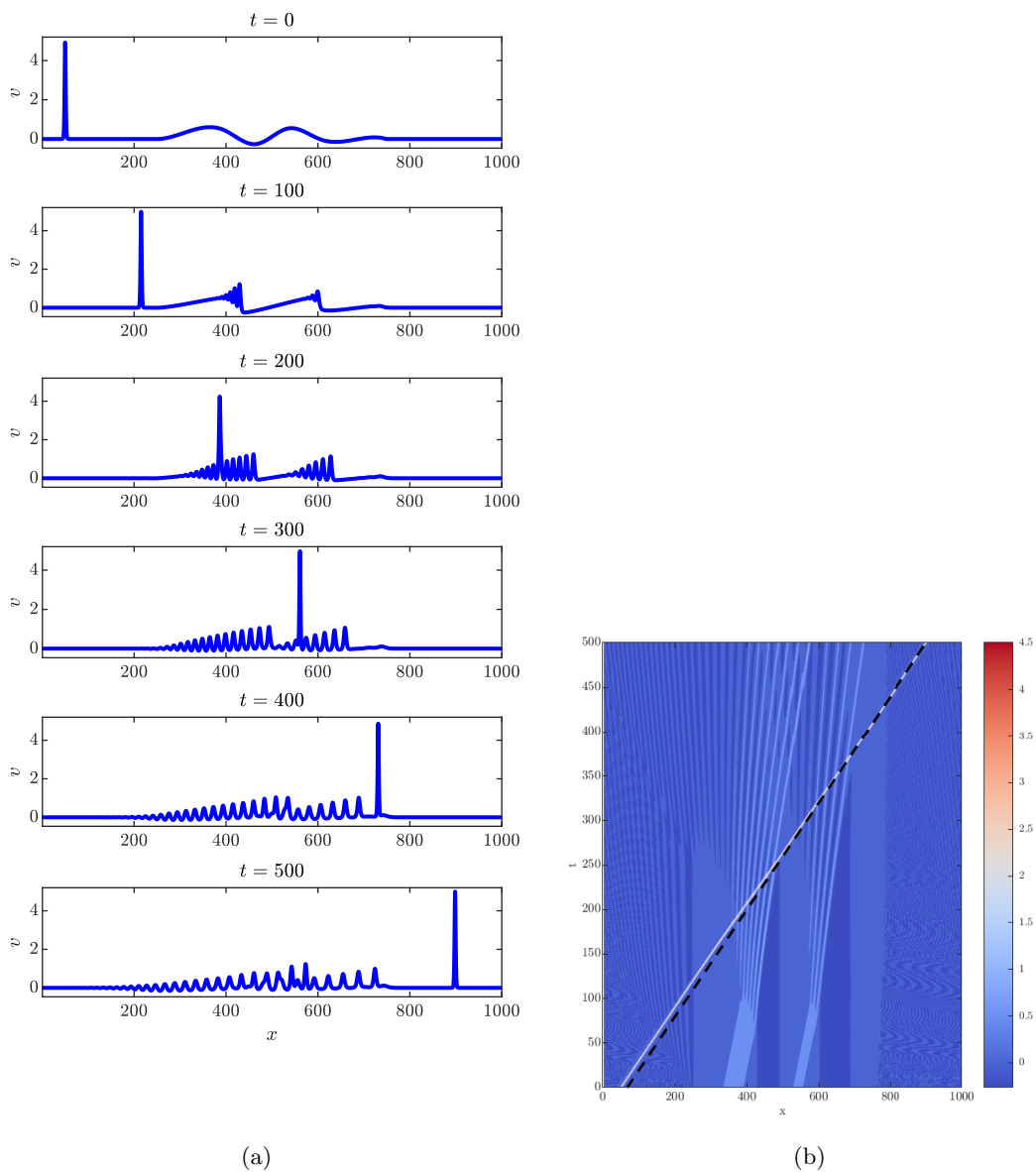


Figure 5.8: Example of a generic localized profile evolving according to KdV and its interaction with a soliton. (a) At different times (b) Space-time contour plot. Note the subtle phase shift identified by the difference between the t -intercepts of the dashed curve and solid line.

Chapter 6

Conclusion

This thesis is pushing forward the analytical description and physical interpretation of non-integrable dispersive hydrodynamics. Many of the results here were previously known only for integrable systems through IST, but we have bypassed the requirement of complete integrability here. The structures and interactions studied appear in a multitude of areas, including fluids, optics, condensed matter, and quantum mechanics. This thesis has set up a general framework for exploring these types of problems.

Whitham modulation theory has been shown to not only posit simple predictions for a wide range of phenomena, but also shows excellent agreement with both numerics and experiment. This invites further investigation of dispersive hydrodynamic problems. We highlight one such problem currently being studied: linear wavepacket-mean flow interaction [12]. This is currently under investigation for viscous fluid conduits, where diagonalization of the 2×2 system

$$\begin{aligned}\bar{\phi}_t + 2\bar{\phi}\bar{\phi}_z &= 0, \\ k_t + (\omega_0(k, \bar{\phi}))_z &= 0,\end{aligned}\tag{6.1}$$

results in an adiabatic invariant describing the change in the wavenumber k due to the mean $\bar{\phi}$

$$q(\bar{\phi}, k) = \frac{(1 + \bar{\phi}k^2)^2}{\bar{\phi}(2 + \bar{\phi}k^2)}.\tag{6.2}$$

Preliminary numerical studies of the conduit equation confirm that q is invariant to changes in the mean flow. It remains to study this problem experimentally.

This work has broad implications for more complex dispersive hydrodynamic systems. While we studied a scalar dispersive hydrodynamic equation here, this framework can be extended to a system of (1+1)-dimensional equations (e.g. NLS) or for (2+1)-dimensional equations, such as the KP equation, which describes, for example, two-dimensional shallow water waves

$$(u_t + uu_x + u_{xxx})_x + \lambda u_{yy} = 0, \quad \lambda = \pm 1, \quad x, y \in \mathbb{R}, \quad t > 0, \quad (6.3)$$

where $\lambda = -1$ is called the KPI equation, and $\lambda = 1$ is the KP-II equation. Work on these types of equations are already underway in the Dispersive Hydrodynamics Laboratory. NLS has been studied in the context of solitonic dispersive hydrodynamics [74], and a study of KP-II soliton modulations using the KP-Whitham equations derived in [3] is presently underway. The modulation theory framework generalizes neatly to fundamental problems in dispersive hydrodynamics.

Bibliography

- [1] M. J. Ablowitz. Nonlinear Dispersive Waves: Asymptotic Analysis and Solitons. Cambridge Texts in Applied Mathematics. Cambridge UP, Cambridge, UK ; New York, 1 edition edition, October 2011.
- [2] M. J. Ablowitz, D. E. Baldwin, and M. A. Hoefer. Soliton generation and multiple phases in dispersive shock and rarefaction wave interaction. Phys. Rev. E, 80:016603, Jul 2009.
- [3] Mark J Ablowitz, Gino Biondini, and Igor Rumanov. Whitham modulation theory for $(2 + 1)$ -dimensional equations of kadomtsev–petviashvili type. Journal of Physics A: Mathematical and Theoretical, 51(21):215501, Apt 2018.
- [4] A. Amo, S. Pigeon, D. Sanvitto, V. G. Sala, R. Hivet, I. Carusotto, F. Pisanello, G. Leménager, R. Houdré, E. Giacobino, C. Ciuti, and A. Bramati. Polariton superfluids reveal quantum hydrodynamic solitons. Science, 332(6034):1167–1170, 2011.
- [5] D. V. Anderson, M.D. Maiden, and M.A. Hoefer. Controlling dispersive hydrodynamic wave-breaking in a viscous fluid conduit. in preparation, 2018.
- [6] Diego Arcas and Harvey Segur. Seismically generated tsunamis. Philosophical Transactions of the Royal Society of London A: Mathematical, Physical and Engineering Sciences, 370(1964):1505–1542, 2012.
- [7] Victor Barcion and Frank M. Richter. Nonlinear Waves in Compacting Media. Journal of Fluid Mechanics, 164(-1):429–448, 1986.
- [8] J. Boussinesq. Essai sur la theorie des eaux courantes. l’Acad. des Sci. Inst. Nat. France, 23:1–680, 1877.
- [9] Iacopo Carusotto and Cristiano Ciuti. Quantum fluids of light. Rev. Mod. Phys., 85:299–366, Feb 2013.
- [10] C. Chong, M. A. Porter, P. G. Kevrekidis, and C. Daraio. Nonlinear coherent structures in granular crystals. Journal of Physics: Condensed Matter, 29(41):413003, 2017.
- [11] Matteo Conforti, Fabio Baronio, and Stefano Trillo. Resonant radiation shed by dispersive shock waves. Phys. Rev. A, 89(1):013807, January 2014.
- [12] T. Congy, G. A. El, and M. A. Hoefer. Interaction of linear modulated waves with unsteady dispersive hydrodynamic states, 2018.

- [13] Constantine M. Dafermos. Hyperbolic Conservation Laws in Continuum Physics. Springer, 3rd edition, December 2009.
- [14] Guo Deng, Gino Biondini, and Stefano Trillo. Small dispersion limit of the Korteweg–de Vries equation with periodic initial conditions and analytical description of the Zabusky-Kruskal experiment. Physica D: Nonlinear Phenomena, 333:137 – 147, 2016. Dispersive Hydrodynamics.
- [15] Guo Deng, Sitai Li, Gino Biondini, and Stefano Trillo. Recurrence due to periodic multisoliton fission in the defocusing nonlinear schrödinger equation. Phys. Rev. E, 96:052213, Nov 2017.
- [16] V. D. Djordjevic and L. G. Redekopp. The Fission and Distintegration of Internal Solitary Waves Moving over Two-Dimensional Topography. J Phys. Oceanogr., 8:1016–1024, 1978.
- [17] Zachary Dutton, Michael Budde, Christopher Slowe, and Lene Vestergaard Hau. Observation of quantum shock waves created with ultra- compressed slow light pulses in a bose-einstein condensate. Science, 293(5530):663–668, 2001.
- [18] G. A. El. Resolution of a shock in hyperbolic systems modified by weak dispersion. Chaos: An Interdisciplinary Journal of Nonlinear Science, 15(3):037103, 2005.
- [19] G. A. EL, R. H. J. GRIMSHAW, and A. M. KAMCHATNOV. Evolution of solitary waves and undular bores in shallow-water flows over a gradual slope with bottom friction. Journal of Fluid Mechanics, 585:213–244, 2007.
- [20] G. A. El, R. H. J. Grimshaw, and W. K. Tiong. Transformation of a shoaling undular bore. Journal of Fluid Mechanics, 709:371–395, 2012.
- [21] G. A. El and M. A. Hoefer. Dispersive shock waves and modulation theory. Physica D, 333:11–65, 2016.
- [22] G. A. El, M. A. Hoefer, and M. Shearer. Dispersive and diffusive-dispersive shock waves for nonconvex conservation laws. SIAM Rev, 59(1):3–61, 2017.
- [23] G. A. El and A. M. Kamchatnov. Kinetic Equation for a Dense Soliton Gas. Phys. Rev. Lett., 95(20), November 2005.
- [24] G.A. El, R.H.J. Grimshaw, and N.F. Smyth. Asymptotic description of solitary wave trains in fully nonlinear shallow-water theory. Physica D, 237, 2008.
- [25] Gennady A. El and Noel F. Smyth. Radiating dispersive shock waves in non-local optical media. P. Roy. Soc. A-Math Phy., 472(2187):20150633, March 2016.
- [26] T. Elperin, N. Kleeorin, and A. Krylov. Nondissipative shock waves in two-phase flows. Physica D, 74:372–385, 1994.
- [27] David Farmer and Laurence Armi. The Generation and Trapping of Solitary Waves over Topography. Science, 283(5399):188–190, 1999.
- [28] E. Fradkin. Field Theories of Condensed Matter Physics. Cambridge UP, Cambridge, UK, 2 edition edition, 2013.

- [29] E. L. Geist, V. V. Titov, D. Arcas, F. F. Pollitz, and S. L. Bilek. Implications of the 26 December 2004 Sumatra-Andaman Earthquake on Tsunami Forecast and Assessment Models for Great Subduction-Zone Earthquakes. Bull. Seis., 97(1A):S249–S270, 2007.
- [30] R. Grimshaw. Slowly varying solitary waves. i. Korteweg-De Vries equation. Proc. R. Soc. Lond. A, 368:359, 1979.
- [31] R. Grimshaw and C. Yuan. Depression and elevation tsunami waves in the framework of the korteweg–de vries equation. Natural Hazards, 84(2):493–511, Nov 2016.
- [32] R. Grimshaw and C. Yuan. The propagation of internal undular bores over variable topography. Physica D: Nonlinear Phenomena, 333:200 – 207, 2016. Dispersive Hydrodynamics.
- [33] A. V. Gurevich, A. L. Krylov, and G. A. El. Nonlinear modulated waves in dispersive hydrodynamics. Sov. Phys. JETP, 71(5):899–910, 1990.
- [34] A. V. Gurevich and L. P. Pitayevskii. Nonstationary structure of a collisionless shock wave. Sov. Phys. JETP, 38(2):291–297, 1974.
- [35] Joseph L. Hammack and Harvey Segur. The Korteweg-de Vries equation and water waves. part 2. comparison with experiments. Journal of Fluid Mechanics, 65(2):289–314, 1974.
- [36] Joseph L. Hammack and Harvey Segur. The Korteweg-de Vries equation and water waves. Part 3. Oscillatory waves. Journal of Fluid Mechanics, 84(2):337–358, 1978.
- [37] S. E. Harris. Conservation laws for a nonlinear wave equation. Nonlinearity, 9(1):187–208, January 1996.
- [38] S. E Harris and P. A Clarkson. Painleve analysis and similarity reductions for the magma equation. SIGMA. Symmetry, Integrability and Geometry: Methods and Applications, 2:068, 2006.
- [39] Lene V. Hau, S. E. Harris, Zachary Dutton, and Cyrus H. Behroozi. Light speed reduction to 17 metres per second in an ultracold atomic gas. Nature, 397:594–598, 1999.
- [40] Karl R. Helfrich and John A. Whitehead. Solitary waves on conduits of buoyant fluid in a more viscous fluid. Geophysical & Astrophysical Fluid Dynamics, 51(1):35–52, 1990.
- [41] E. J. Hinch. Perturbation Methods. Cambridge Texts in Applied Mathematics. Cambridge UP, Cambridge, UK ; New York, 1 edition edition, 1991.
- [42] M. A. Hofer, M. J. Ablowitz, I. Coddington, E. A. Cornell, P. Engels, and V. Schweikhard. Dispersive and classical shock waves in bose-einstein condensates and gas dynamics. Phys. Rev. A, 74:023623, Aug 2006.
- [43] P. A. Praveen Janantha, Patrick Sprenger, Mark A. Hofer, and Mingzhong Wu. Observation of self-cavitating envelope dispersive shock waves in yttrium iron garnet thin films. Phys. Rev. Lett., 119:024101, Jul 2017.
- [44] V.I. Karpman. An asymptotic solution of the Korteweg-de Vries equation. Physics Letters A, 25(10):708 – 709, 1967.
- [45] C. T. Kelley. Iterative methods for linear and nonlinear equations. SIAM, Philadelphia, 1995.

- [46] Yuri S. Kivshar and Boris A. Malomed. Dynamics of solitons in nearly integrable systems. Rev. Mod. Phys., 61:763–915, Oct 1989.
- [47] D. J. Korteweg and G. de Vries. On the change of form of long waves advancing in a rectangular canal, and on a new type of long stationary wave. Philosophical Magazine, 39:422–433, 1895.
- [48] L. D. Landau and E. Lifshitz. Fluid Mechanics. Butterworth-Heinemann, Oxford, UK, 2 edition edition, 1987.
- [49] David Levermore. The hyperbolic nature of the zero dispersion KdV limit. Commun Part Diff Eq, 13(4):495–514, 1988.
- [50] N. K. Lowman and M. A. Hoefer. Dispersive hydrodynamics in viscous fluid conduits. Phys. Rev. E, 88(2):023016, 2013.
- [51] N. K. Lowman, M. A. Hoefer, and G. A. El. Interactions of large amplitude solitary waves in viscous fluid conduits. Journal of Fluid Mechanics, 750:372–384, 2014.
- [52] Nicholas K. Lowman and M. A. Hoefer. Dispersive shock waves in viscously deformable media. Journal of Fluid Mechanics, 718:524, 2013.
- [53] J. C. Luke. A perturbation method for nonlinear dispersive wave problems. P. Roy. Soc. Lond. A-Mat., 292(1430):403–412, 1966.
- [54] M. D. Maiden, D. V. Anderson, N. A. Franco, G. A. El, and M. A. Hoefer. Solitonic dispersive hydrodynamics: Theory and observation. Phys. Rev. Lett., 120:144101, Apr 2018.
- [55] M. D. Maiden and M. A. Hoefer. Modulations of viscous fluid conduit periodic waves. Proceedings of the Royal Society of London A: Mathematical, Physical and Engineering Sciences, 472(2196), 2016.
- [56] Michelle D. Maiden, Nicholas K. Lowman, Dalton V. Anderson, Marika E. Schubert, and Mark A. Hoefer. Observation of dispersive shock waves, solitons, and their interactions in viscous fluid conduits. Phys. Rev. Lett., 116(17):174501, 2016.
- [57] T. R. Marchant and N. F. Smyth. Approximate techniques for dispersive shock waves in nonlinear media. 1250035, 21(3):18, 2012.
- [58] M. Matsuyama, M. Ikeno, T. Sakakiyama, and T. Takeda. A study of tsunami wave fission in an undistorted experiment. Pure Appl. Geophys., 164:617–631, 2007.
- [59] D McKenzie. Generation and compaction of partially molten rock. J. Petrol., 25(3):713–765, 1984.
- [60] Y. C. Mo, R. A. Kishek, D. Feldman, I. Haber, B. Beaudoin, P. G. O’Shea, and J. C. T. Thangaraj. Experimental observations of soliton wave trains in electron beams. Phys. Rev. Lett., 110:084802, Feb 2013.
- [61] M. Nakayama and D. P. Mason. Compressive solitary waves in compacting media. Int. J. Nonlinear Mech., 26(5):631–640, 1991.
- [62] Peter Olson and Ulrich Christensen. Solitary wave propagation in a fluid conduit within a viscous matrix. Journal of Geophysical Research, 91(B6):6367–6374, 1986.

- [63] A. R. Osborne and T. L. Burch. Internal Solitons in the Andaman Sea. Science, 208:451–460, May 1980.
- [64] E. Ray, P. Bunton, and J. A. Pojman. Determination of the diffusion coefficient between corn syrup and distilled water using a digital camera. American Journal of Physics, 75:903–906, October 2007.
- [65] Frank M. Richter and Dan McKenzie. Dynamical models for melt segregation from a deformable matrix. The J. Geophys. Res., 92(6):729–740, November 1984.
- [66] Joshua E. Rothenberg and D. Grischkowsky. Observation of the formation of an optical intensity shock and wave breaking in the nonlinear propagation of pulses in optical fibers. Phys. Rev. Lett., 62:531–534, Jan 1989.
- [67] J. Scott Russell. Report on waves, 1845.
- [68] David R. Scott and David J. Stevenson. Magma solitons. Geophys. Res. Lett., 11(11):1161–1164, 1984.
- [69] David R. Scott, David J. Stevenson, and John A. Whitehead. Observations of solitary waves in a viscously deformable pipe. Nature, 319(6056):759–761, February 1986.
- [70] G Simpson, M Spiegelman, and M I Weinstein. Degenerate dispersive equations arising in the study of magma dynamics. Nonlinearity, 20(1):21–49, January 2007.
- [71] G. Simpson, M. Spiegelman, and M. I. Weinstein. A Multiscale Model of Partial Melts 1: Effective Equations. J. Geophys. Res., 115:B04410, 2010.
- [72] G Simpson and MI Weinstein. Asymptotic stability of ascending solitary magma waves. SIAM J. Math. Anal., 40(4):1337–1391, 2008.
- [73] P. Sprenger and M. A. Hoefer. Shock waves in dispersive hydrodynamics with nonconvex dispersion. SIAM J Appl Math, 77(1):26–50, 2017.
- [74] P. Sprenger, M. A. Hoefer, and G. A. El. Hydrodynamic optical soliton tunneling. Phys. Rev. E, 97:032218, Mar 2018.
- [75] R. J. Taylor, D. R. Baker, and H. Ikezi. Observation of collisionless electrostatic shocks. Phys. Rev. Lett., 24:206–209, Feb 1970.
- [76] S. Trillo, G. Deng, G. Biondini, M. Klein, G. F. Clauss, A. Chabchoub, and M. Onorato. Experimental observation and theoretical description of multisoliton fission in shallow water. Phys. Rev. Lett., 117:144102, Sep 2016.
- [77] S. Trillo, M. Klein, G. F. Clauss, and M. Onorato. Observation of dispersive shock waves developing from initial depressions in shallow water. Physica D: Nonlinear Phenomena, 333:276–284, 2016. Dispersive Hydrodynamics.
- [78] Vasiliy Vlasenko, Nataliya Stashchuk, Mark E. Inall, and Joanne E. Hopkins. Tidal energy conversion in a global hot spot: On the 3-D dynamics of baroclinic tides at the Celtic Sea shelf break. Journal of Geophysical Research: Oceans, 119:3249–3265, 2014.

- [79] Wenjie Wan, Shu Jia, and Jason W. Fleischer. Dispersive superfluid-like shock waves in nonlinear optics. Nature Physics, 3(1):46–51, 01 2007.
- [80] Zhongde Wang and B.R. Hunt. The discreteW transform. Appl. Math. Comput., 16(1):19–48, January 1985.
- [81] J. A. Whitehead and K. R. Helfrich. Magma waves and diapiric dynamics. In M. P. Ryan, editor, Magma Transport and Storage, pages 53–76. John Wiley & Sons, Chichester, UK, 1990.
- [82] J. A. Whitehead and D. S. Luther. Dynamics of Laboratory Diapir and Plume Models. Journal of Geophysical Research, 80(5):705–717, 1975.
- [83] John A. Whitehead and Karl R. Helfrich. The Korteweg-deVries equation from laboratory conduit and magma migration equations. Geophysical Research Letters, 13(6):545–546, June 1986.
- [84] John A. Whitehead and Karl R. Helfrich. Wave transport of deep mantle material. Nature, 336(6194):59–61, November 1988.
- [85] G. B. Whitham. A general approach to linear and non-linear dispersive waves using a Lagrangian. J. Fluid Mech., 22(02):273–283, June 1965.
- [86] G. B. Whitham. Non-linear dispersive waves. Proc. Roy. Soc. Ser. A, 283:238–261, 1965.
- [87] G.B. Whitham. Linear and Nonlinear Waves. John Wiley & Sons, 1974.
- [88] R. E Wyatt and C. J. Trahan. Quantum Dynamics with Trajectories: Introduction to Quantum Hydrodynamics. Number 28 in Interdisciplinary Applied Mathematics. Springer, New York, 2005.
- [89] Gang Xu, Matteo Conforti, Alexandre Kudlinski, Arnaud Mussot, and Stefano Trillo. Dispersive dam-break flow of a photon fluid. Phys. Rev. Lett., 118:254101, Jun 2017.
- [90] N. J. Zabusky and M. D. Kruskal. Interaction of “solitons” in a collisionless plasma and the recurrence of initial states. Physical Review Letters, 15(6):240, 1965.
- [91] V.E. Zakharov and L.A. Ostrovsky. Modulation instability: The beginning. Physica D: Nonlinear Phenomena, 238(5):540–548, March 2009.

Appendix A

Numerical Methods

A.1 Periodic Solutions

We compute unit-mean conduit periodic traveling wave solutions $\tilde{\phi}(\theta)$ for specified $(\tilde{k}, \tilde{\mathcal{A}})$ with a Newton-GMRES iterative method [45] on the first integral of equation (2.1)

$$A + \tilde{\omega}\tilde{\phi} - \tilde{k}\tilde{\phi}^2 - \tilde{\omega}\tilde{k}^2\tilde{\phi}\tilde{\phi}'' + \tilde{\omega}\tilde{k}^2(\tilde{\phi}')^2 = 0, \quad (\text{A.1})$$

where $A \in \mathbb{R}$ is an integration constant. We use a spectral method to compute the unit-mean cosine series representation $\tilde{\phi}(\theta) = 1 + \sum_{n=1}^N 2a_n \cos n\theta$. Equation (A.1) is discretized in spectral space $\{a_n\}_{n=1}^N$ with the fast and accurate computation of derivatives achieved via fast cosine transforms (DCT II in [80]). The projection of (A.1) onto constants determines A , which we do not require because of our imposition of unit mean. Projection of equation (A.1) onto $\cos(n\theta)$ for $n = 1, \dots, N$ yields N equations for the $N + 1$ unknowns $((a_n)_{n=1}^N, \tilde{\omega})$. The amplitude constraint $\tilde{\phi}(\pi) - \tilde{\phi}(0) = -4 \sum_{n \text{ odd}} a_n = \tilde{\mathcal{A}}$ closes the system of equations. We precondition the spectral equations by dividing each by the sum of linear coefficients, shifted by $2k + 1$, i.e., by $\tilde{\omega} + n^2\tilde{\omega}\tilde{k}^2 + 1$. The accurate resolution of each solution is maintained by achieving an absolute tolerance of 10^{-13} in the 2-norm of the residual and choosing N so that $|a_n|$ is below $5 \cdot 10^{-12}$ for $n > 3N/4$. The number of coefficients required strongly depends on the wavenumber \tilde{k} . For example, when $0.5 \leq \tilde{k} \leq 4$, we find $N = 2^6$ provides sufficient accuracy whereas for $0.002 \leq \tilde{k} \leq 0.01$, we use $N = 2^{12}$.

With the cosine series coefficients of $\tilde{\phi}(\theta)$ in hand, we compute the unit-mean averaging integrals \tilde{I}_j , $j = 1, 2, 3$ in equations (2.28), (2.25) using the spectrally accurate trapezoidal rule. We

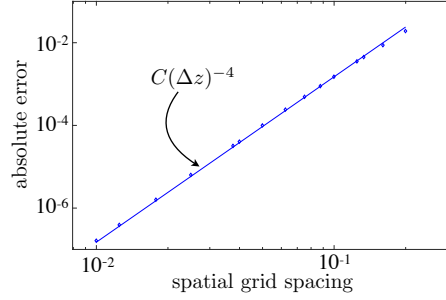


Figure A.1: Maximum absolute error in the direct numerical simulation of the conduit equation, achieving fourth order spatial accuracy as expected. The solution used in validation was a periodic wave with $k = 3$ and $a = 0.5$ generated with accuracy 10^{-8} , and was simulated over 50 spatial periods and 5 temporal periods. The reference line is $C(\Delta z)^{-4}$.

then use sixth order finite differencing to compute derivatives of \tilde{I}_j and $\tilde{\omega}$ on a grid of wavenumbers and amplitudes as explained in section 2.3.2. This numerically determines the Whitham equations in the form (2.29).

A.2 Time Stepping

For the direct numerical simulation of the conduit equation (1.3), it is convenient to write it in the form of two coupled equations:

$$\begin{cases} \mathcal{P} = A^{-1}A_t, \\ A\mathcal{P} + (A^2)_z - (A^2\mathcal{P}_z)_z = 0. \end{cases} \quad (\text{A.2})$$

The first equation is a temporal ODE in time and the second equation is a linear, elliptic problem $\mathcal{L}(A)\mathcal{P} = -(A^2)_z$ in space. We solve for \mathcal{P} using an equispaced fourth-order finite difference discretization and direct inversion of the resulting banded linear system. We implement time-dependent boundary conditions with prescribed $A(0, t)$ and $A(L, t)$ so that the first equation in (A.2) yields the boundary conditions for \mathcal{P} . Time-stepping is achieved with a fourth-order, explicit Runge-Kutta method with variable timestep (MATLAB's ode45). The solver was validated against computed periodic traveling wave solutions. The maximum error between the numerical solution and the periodic traveling wave solution is reported in figure A.1.